

STOCHASTIC STRONG GROUND MOTION SIMULATIONS ON NORTH  
ANATOLIAN FAULT ZONE AND CENTRAL ITALY: VALIDATION,  
LIMITATION AND SENSITIVITY ANALYSES

A THESIS SUBMITTED TO  
THE GRADUATE SCHOOL OF NATURAL AND APPLIED SCIENCES  
OF  
MIDDLE EAST TECHNICAL UNIVERSITY

BY

BELİZ UĞURHAN

IN PARTIAL FULFILLMENT OF THE REQUIREMENTS  
FOR  
THE DEGREE OF MASTER OF SCIENCE  
IN  
CIVIL ENGINEERING

SEPTEMBER 2010

Approval of the thesis:

**STOCHASTIC STRONG GROUND MOTION SIMULATIONS ON NORTH  
ANATOLIAN FAULT ZONE AND CENTRAL ITALY: VALIDATION,  
LIMITATION AND SENSITIVITY ANALYSES**

submitted by **BELİZ UĞURHAN** in partial fulfillment of the requirements for the degree of **Master of Science in Civil Engineering Department, Middle East Technical University** by,

Prof. Dr. Canan Özgen  
Dean, Graduate School of **Natural and Applied Sciences**

\_\_\_\_\_

Prof. Dr. Güney Özcebe  
Head of Department, **Civil Engineering**

\_\_\_\_\_

Assist. Prof. Dr. Ayşegül Askan Gündoğan  
Supervisor, **Civil Engineering Dept., METU**

\_\_\_\_\_

**Examining Committee Members:**

Prof. Dr. M. Semih Yüccemen  
Civil Engineering Dept., METU

\_\_\_\_\_

Assist. Prof. Dr. Ayşegül Askan Gündoğan  
Civil Engineering Dept., METU

\_\_\_\_\_

Assoc. Prof. Dr. M. Altuğ Erberik  
Civil Engineering Dept., METU

\_\_\_\_\_

Assist. Prof. Dr. Zeynep Gülerce  
Civil Engineering Dept., METU

\_\_\_\_\_

Dr. Nazan Yılmaz  
Disaster and Emergency Management Presidency

\_\_\_\_\_

**Date:**

15.09.2010

\_\_\_\_\_

**I hereby declare that all information in this document has been obtained and presented in accordance with academic rules and ethical conduct. I also declare that, as required by these rules and conduct, I have fully cited and referenced all material and results that are not original to this work.**

Name, Last name : Beliz, Uğurhan

Signature :

## **ABSTRACT**

### **STOCHASTIC STRONG GROUND MOTION SIMULATIONS ON NORTH ANATOLIAN FAULT ZONE AND CENTRAL ITALY: VALIDATION, LIMITATION AND SENSITIVITY ANALYSES**

Uğurhan, Beliz

M. Sc., Department of Civil Engineering

Supervisor: Assist. Prof. Dr. Ayşegül Askan Gündoğan

September 2010, 126 pages

Assessment of potential ground motions in seismically active regions is essential for purposes of seismic design and analysis. Peak ground motion intensity values and frequency content of seismic excitations are required for reliable seismic design, analysis and retrofitting of structures. In regions of sparse or no strong ground motion records, ground motion simulations provide physics-based synthetic records. These simulations provide not only the earthquake engineering parameters but also give insight into the mechanisms of the earthquakes.

This thesis presents strong ground motion simulations in three regions of intense seismic activity. Stochastic finite-fault simulation methodology with a dynamic corner frequency approach is applied to three case studies performed in Düzce, L'Aquila and Erzincan regions. In Düzce study, regional seismic source, propagation and site parameters are determined through validation of the simulations against the records. In L'Aquila case study, in addition to study of the regional parameters, the limitations of the method in terms of simulating the directivity effects are also investigated. In Erzincan case study, where there are very few records, the optimum model parameters are determined using a large set of simulations with an error-minimization scheme. Later, a parametric sensitivity study is performed to observe the variations in simulation results to small perturbations in input parameters.

Results of this study confirm that stochastic finite-fault simulation method is an effective technique for generating realistic physics-based synthetic records of large earthquakes in near field regions.

Keywords: Earthquake, Strong ground motion simulation, Stochastic method, Directivity effects, Finite-fault

## ÖZ

### KUZEY ANADOLU FAY HATTI VE ORTA İTALYA'DA STOKASTİK KUVVETLİ YER HAREKETİ SİMULASYONLARI: DOĞRULAMA, YETERLİLİK VE DUYARLILIK ANALİZLERİ

Uğurhan, Beliz

Yüksek Lisans, İnşaat Mühendisliği Bölümü

Tez Yöneticisi: Y. Doç. Dr. Ayşegül Askan Gündoğan

Eylül 2010, 126 sayfa

Sismik olarak aktif bölgelerde depreme dayanıklı tasarım ve analiz çalışmaları için potansiyel yer hareketlerinin değerlendirilmesi zorunludur. Yapıların güvenilir deprem tasarımı, analizi ve güçlendirilmesi için yer hareketlerinin olası en büyük değerleri ve frekans içeriği gereklidir. Kuvvetli yer hareketi kaydı olmayan veya yetersiz kayıt bulunan bölgelerde, yer hareketi simülasyonları fizik-temelli sentetik kayıtlar sağlar. Bu simülasyonlar sadece deprem mühendislerini ilgilendiren parametreler temin etmekle kalmaz, aynı zamanda depremlerin mekanizmalarını anlamak için öngörü sağlar.

Bu tez çalışmasında yoğun sismik aktiviteye sahip üç bölgede kuvvetli yer hareketi simülasyonları sunulmaktadır. Dinamik köşe-frekansı yaklaşımına dayanan stokastik sonlu-fay simülasyon yöntemi, Düzce, L'Aquila ve Erzincan bölgelerinde gerçekleştirilen üç örnek çalışmaya uygulanmıştır. Düzce çalışmasında, bölgesel sismik kaynak, yayılım ve saha parametreleri, simülasyonların gerçek kayıtlarla doğrulanması aracılığı ile belirlenmiştir. L'Aquila örnek çalışmasında, bölgesel parametrelerin belirlenmesinin yanı sıra, kullanılan yöntemin depremin yönlülük etkilerini simüle etmekteki yeterliliği araştırılmıştır. Çok az kayıt bulunan Erzincan bölgesi için yapılan çalışmada ise optimum model parametreleri, geniş simülasyon

grupları kullanılarak hatayı en aza indirme yöntemiyle belirlenmiştir. Daha sonra, girdi parametrelerindeki küçük değişikliklerin simülasyon sonuçları üzerinde yarattığı değişimi gözlemek amacıyla parametrik duyarlılık çalışması yapılmıştır.

Bu çalışmanın sonuçları stokastik sonlu-fay simülasyon yönteminin, büyük depremler için yakın saha bölgelerinde gerçekçi fizik-tabanlı sentetik kayıtlar ürettiği kanıtlamıştır.

Anahtar Kelimeler: Deprem, Kuvvetli yer hareketi simülasyonu, Stokastik yöntem, Yönlülük etkileri, Sonlu-fay

To My Parents  
To My Supervisor Dr. Ayşegül Askan Gündoğan

## ACKNOWLEDGEMENTS

I would like to express my profound gratitude to my supervisor Assist. Prof. Dr. Ayşegül Askan Gündoğan, whose encouragement, knowledge and support from the initial to the final level enabled me to develop an understanding of the subject. This thesis would not have been possible without her guidance, foresight and optimism. I am very lucky to have an adviser like her.

I am grateful to Assoc. Prof. Dr. M. Altuğ Erberik for his patience and support. It is a pleasure to work with him. I would also like to thank Assoc. Prof. Dr. Sinan Akkar for providing me the digital fault map of Turkey. Furthermore, I am indebted to Dr. Nazan Yılmaz who made possible the maps existing in this thesis by politely offering the digital district maps of Turkey. I am also heartily thankful to Dr. Aybige Akinci for the guidance and criticism she provided in the L'Aquila section.

I owe my sincere gratitude to Dr. Dariush Motazedian for kindly offering the computer program, EXSIM. Dr. David M. Boore is gratefully acknowledged for making valuable suggestions and discussions about the results of this study. Special thanks go to Assist. Prof. Dr. Yalın Arıcı for making me smile every time I feel desperate. Finally, Prof. Dr. M. Semih Yüçemen and Assist. Prof. Dr. Zeynep Gülerce are kindly acknowledged for their careful revisions and positive feedback.

My dear officemate Bilge Özer and friends Elif Müge Ün, Aslıcan Yılmaz, Berk Baltacı, Burçin Gürses, Aynur Giray and Noyan Ercan are always with me throughout this study providing me continuous support and joviality.

Finally, I want to thank to my beloved mother Muzaffer Uğurhan, father Türker Uğurhan and brother Mert Uğurhan for their endless support, encouragement, and love.

## TABLE OF CONTENTS

ABSTRACT .....	iv
ÖZ .....	vi
ACKNOWLEDGEMENTS .....	ix
TABLE OF CONTENTS .....	x
CHAPTERS	
1. INTRODUCTION .....	1
1.1. GENERAL.....	1
1.2. LITERATURE SURVEY .....	2
1.3. OBJECTIVE AND SCOPE.....	6
2. STOCHASTIC STRONG GROUND MOTION SIMULATION	
METHODOLOGY.....	8
2.1. GENERAL.....	8
2.2. STOCHASTIC POINT-SOURCE MODELING.....	8
2.2.1. <i>The Source Function (<math>E(M_0, \omega)</math>)</i> .....	11
2.2.2. <i>The Path Function (<math>P(R, \omega)</math>)</i> .....	17
2.2.3. <i>The Site Function (<math>G(\omega)</math>)</i> .....	21
2.2.4. <i>Type of Ground Motion (<math>I(\omega)</math>)</i> .....	26
2.3. STOCHASTIC FINITE-FAULT MODELING .....	26
3. GROUND MOTION SIMULATION OF THE 1999 DÜZCE EARTHQUAKE:	
A VALIDATION STUDY.....	32
3.1. GENERAL.....	32
3.2. BACKGROUND INFORMATION .....	32
3.3. STRONG GROUND MOTION DATA .....	35
3.4. MODEL PARAMETERS.....	38
3.5. RESULTS OF SIMULATIONS AND DISCUSSIONS.....	47
3.5.1. <i>Comparison of Observed and Simulated Waveforms</i> .....	47
3.5.2. <i>Simulation of Forward Directivity with an Analytical Pulse</i> .....	50

3.5.3. <i>Comparison of Observed Damage with the Distribution of Simulated Ground Motions</i> .....	52
3.5.4. <i>Comparison of Attenuation of Synthetics with GMPEs</i> .....	56
4. GROUND MOTION SIMULATION OF THE 2009 L’AQUILA EARTHQUAKE: SIMULATING DIRECTIVITY EFFECTS .....	60
4.1. GENERAL.....	60
4.2. BACKGROUND INFORMATION .....	62
4.3. STRONG GROUND MOTION DATA .....	64
4.4. VALIDATION OF SIMULATION PARAMETERS.....	66
4.5. RESULTS OF THE SIMULATIONS AND DISCUSSIONS.....	72
5. A SENSITIVITY ANALYSIS FOR EASTERN NORTH ANATOLIAN FAULT ZONE: ERZİNCAN CASE STUDY .....	79
5.1. GENERAL.....	79
5.2. BACKGROUND INFORMATION .....	80
5.3. GROUND MOTION SIMULATION OF 1992 ERZINCAN EARTHQUAKE.....	83
5.3.1. <i>Simulation Parameters</i> .....	83
5.3.2. <i>Variation in the Simulation Results with respect to Alternative Models</i> .	88
5.4. A LOCAL SENSITIVITY ANALYSIS AROUND THE OPTIMUM PARAMETERS .....	90
5.4.1. <i>Sensitivity of Simulations with respect to Source Parameters</i> .....	91
5.4.2. <i>Sensitivity of Simulations with respect to Path Parameters</i> .....	93
5.4.3. <i>Sensitivity of Simulations with respect to Site Parameters</i> .....	96
6. CONCLUDING REMARKS .....	99
6.1. SUMMARY .....	99
6.2. OBSERVATIONS AND CONCLUSIONS .....	100
6.3. FUTURE WORK AND RECOMMENDATIONS.....	103
REFERENCES.....	105
APPENDICES	
A. STRESS DROP.....	118
B. MAGNITUDE SCALES.....	121
C. MISFIT VALUES OF DÜZCE AND L’AQUILA SIMULATIONS.....	124
D. DIRECTIVITY .....	125

## LIST OF TABLES

### TABLES

Table 3.1 Information on the strong motion stations that recorded the 1999 Düzce earthquake .....	36
Table 3.2 Information on the strong motion stations used in the derivation of site specific parameters.....	42
Table 3.3 Finite-fault model parameters for the 12 November 1999 Düzce earthquake simulation.....	46
Table 3.4 Central damage ratios for the damage levels .....	53
Table 4.1 Information on the strong motion stations that recorded the 2009 L’Aquila earthquake .....	65
Table 4.2 Finite-fault model parameters for the 2009 L’Aquila earthquake simulation.....	72
Table 5.1 Information on the strong motion stations used in the validation of the finite-fault model of the 13 March Erzincan earthquake .....	82
Table 5.2 Alternative models used in the ground motion simulation of 1992 Erzincan earthquake .....	84
Table 5.3 Regional parameters of Erzincan Region.....	86

## LIST OF FIGURES

### FIGURES

Figure 2.1 Step by step stochastic point-source modeling procedure (Adapted from Boore, 2003).....	10
Figure 2.2 A tangential stress pulse applied to the interior surface of the dislocation surface with the near-field observation point O.....	12
Figure 2.3 Q versus frequency for different parts of the world (Adapted from Boore, 1984) .....	18
Figure 2.4 Alternative $Q(f)$ values for the Marmara region, Turkey.....	20
Figure 2.5 The effects of different $\kappa_0$ values on the spectrum.....	25
Figure 2.6 Stochastic finite-fault methodology (Adapted from Hisada, 2008).....	28
Figure 3.1 Top panel: Tectonic map of Turkey and the westward migration of major earthquakes on the NAFZ. The top panel is adapted from Utkucu et al. (2003). Bottom panel: Seismicity map of the Marmara region .....	34
Figure 3.2 Map showing the regional setting and slip distribution (bottom table) of 12 November 1999 Düzce earthquake .....	37
Figure 3.3 Average H/V ratios of each station based on mainshock and aftershock recordings and the mean H/V ratio of all available records from the 1999 Düzce earthquake .....	41
Figure 3.4 The distribution of vertical kappa factors versus epicentral distance .....	43

Figure 3.5 Average of the combined site effect $H/V \cdot e^{-\pi f \kappa_0(\text{vertical})}$ for the Düzce region in comparison with those of generic rock and soil conditions by Boore and Joyner (1997) .....	44
Figure 3.6 Model misfit versus frequency for various values of stress drop .....	45
Figure 3.7 Comparison of time histories and Fourier spectra of synthetics with real data for the 12 November 1999 Düzce earthquake at the selected stations .....	48
Figure 3.8 Acceleration, velocity and displacement time histories recorded at the BOL station in comparison with those of the synthetics generated using the analytical directivity model .....	52
Figure 3.9 Distribution of (a) synthetic PGA map (in $\text{cm}/\text{sec}^2$ ) and (b) and mean damage ratios .....	55
Figure 3.10 Comparison of attenuation of synthetic data with recent attenuation relationships derived for the region for (a) regional mean soil conditions, (b) generic rock conditions .....	57
Figure 4.1 Acceleration records from the 2009 L'Aquila earthquake evidencing directivity effects.....	61
Figure 4.2 The aftershock distribution in the L'Aquila region and the epicenter of the mainshock of April 1999 L'Aquila earthquake (Adapted from Akinici <i>et al.</i> , 2010) .....	63
Figure 4.3 Distribution of the strong ground motion stations that recorded the mainshock of the 2009 L'Aquila earthquake .....	66
Figure 4.4 Slip distribution models proposed for 2009 L'Aquila earthquake .....	69

Figure 4.5 Distribution of PGA values for different slip models of 2009 L'Aquila earthquake .....	71
Figure 4.6 Fourier amplitude spectra of forward stations that recorded the 2009 L'Aquila earthquake.....	74
Figure 4.7 Fourier amplitude spectra of backward stations that recorded the 2009 L'Aquila earthquake.....	75
Figure 4.8 Comparison of response spectra curves of equal distant stations.....	77
Figure 4.9 Comparison of PGA and PGV values of observed and synthetic records with respect to azimuth and Joyner-Boore distance of strong ground motions stations .....	78
Figure 5.1 Top Panel: Map showing the plate tectonics of the Anatolian Block (adapted from <a href="http://neic.usgs.gov/neis/eq_depot/2003/eq_030501/">http://neic.usgs.gov/neis/eq_depot/2003/eq_030501/</a> ) Bottom Panel: Regional map showing the active faults in the Erzincan region with the epicenter and strong ground motion stations of 1992 Erzincan earthquake .....	81
Figure 5.2 FAS and acceleration-time series of the observed and synthetic ground motions of 1992 Erzincan earthquake.....	87
Figure 5.3 Errors computed using different combinations of input parameters showing the effect of source, path and site parameters individually .....	89
Figure 5.4 Sensitivity indices with respect to different stress drop values .....	92
Figure 5.5 Sensitivity indices with respect to different quality factors.....	95
Figure 5.6 Sensitivity indices with respect to different kappa operators .....	97

## CHAPTER 1

### INTRODUCTION

#### 1.1 General

Earthquakes are among the most destructive natural hazards that humanity experience. Major earthquakes yield social, economic and structural losses, effects of which can last for long periods of time. According to the earthquake statistics by the United States Geological Survey (USGS), on the average 16 earthquakes per year occur worldwide with magnitudes greater than 7 (<http://earthquake.usgs.gov/earthquakes/eqarchives/year/eqstats.php>). Given the rate of occurrence in addition to their damage potential, it becomes essential to study earthquakes.

Earthquake studies are interdisciplinary by nature and involve a wide group of research fields ranging from earth sciences to civil engineering; from insurance industry to public policy. In civil engineering, for purposes of seismic design and retrofitting of structures, it is essential to utilize reliable estimates of the seismic loads that structures will be exposed to. Not only the peak ground motion intensity parameters but also the frequency content of any seismic excitation is important for seismic design and analysis. This brings the fundamental problem of determining the seismic parameters in regions with sparse or no seismic networks. Even though the best option is to use regional past seismic records, it requires long-term seismic monitoring and sustainable research to retrieve the seismicity of any region of interest. For engineering purposes, empirically-formed Ground Motion Prediction Equations (GMPEs) are frequently used in the estimation of peak ground motion intensity values. Utilizing ground motion records that are obtained in other regions with similar tectonic settings in seismic response analyses is another option.

A relatively recent research field is strong ground motion simulations where earthquake records of well-known seismic sources can be generated using basic rules of geophysics and mathematics. The fundamental approach in ground motion simulations is to mimic the source mechanisms and regional wave propagation properties for estimating reliable synthetic records. Since the tectonic features and seismological properties of the Earth vary spatially, it is not possible to find a unique seismological model that represents the whole Earth. Thus, regional studies representing the characteristics of the seismic sources, wave propagation properties and site conditions become crucial for successful ground motion simulations.

With respect to the solution technique they employ, strong ground motion simulations are divided into two major categories: stochastic and deterministic simulations. In stochastic simulations, inherent randomness of the ground motions is taken into account whereas deterministic approach relies on numerical solutions of the wave equation.

## **1.2 Literature Survey**

Ground motion simulations have always been of interest to both engineering and seismology community. Because they provide insight into the physics of the earthquakes, simulation of ground motions is the most effective tool to study characteristics of the faulting mechanisms and regional seismic parameters. In addition, in regions of sparse or no ground motion recordings, ground motion simulations provide the earthquake engineers peak parameters and frequency content of potential ground motions for seismic design and analysis purposes.

Ground motions can be divided into two categories with respect to their frequency content: low frequency ground motions and high frequency ground motions.

Low frequency ground motions ( $f < 1$  Hz) are deterministic and can be solved with numerical solutions of the partial differential equations representing elastic wave

propagation. In order to solve the wave propagation equation, earthquake source mechanism and the material properties (wave velocity and density variation with depth) in the region of interest must be known. A variety of numerical methods are employed for approximating the solution of wave propagation problem in heterogeneous media. Among these methods, the most popular ones are the finite difference (Frankel and Vidale, 1992; Frankel, 1993; Yomogida and Egten, 1993; Olsen *et al.*, 1996; Olsen and Archuleta, 1996; Moczo *et al.*, 2002), boundary-element (Kawase, 1988; Luco *et al.*, 1990; Pedersen *et al.*, 1994), finite element (Li *et al.*, 1992; Rial *et al.*, 1992; Toshinawa and Ohmachi, 1992; Bao, 1998) and the spectral element methods (Cohen *et al.*, 1993; Priolo *et al.*, 1994; Komatitsch, 1997; Komatitsch and Vilotte, 1998; Komatitsch and Tromp, 1999; Komatitsch *et al.*, 2004). With these numerical techniques for solving the equation of motion, the wave propagation through a three-dimensional medium with complicated surface topography and strong velocity contrasts is performed for near field distances.

An alternative technique is utilizing Green's functions which are simply displacement fields due to unit seismic forces. There are several studies that employ theoretical Green's functions in the deterministic simulation of ground motions (Bouchon, 1981; Hisada, 1994; Chen and Zhang, 2001). Another deterministic method for modeling wave propagation in layered media is the empirical Green's function (EGF) method which is introduced by Hartzell (1978) and developed further by Irikura (1986). In this method, the ground motions of small earthquakes are summed with appropriate scaling to obtain the ground motion of a large earthquake.

The aforementioned methods are deterministic and provide solutions to long period (low frequency) ground motion simulations. On the other hand, high frequency portion of seismic waves are random in nature. They are characterized by the loss of coherency in their phase spectra. Therefore, it is not possible to model the high frequency ground motions with deterministic methods. The method proposed by Housner (1947) and further developed by Housner (1955) and Thomson (1959) was the first attempt to model the ground motions of stochastic character. These studies model the time histories of ground motions by superposing random amplitude and

duration impulses with random time delays. This original model is superseded by the studies of Haskell (1966) and Aki (1967).

Aki (1967) modeled the dislocation due to an earthquake source as a ramp function of time. By assuming that the autocorrelation function of dislocation velocity decreases exponentially, he showed that the source spectrum decreases proportional to the square of frequency ( $\omega^{-2}$ ). On the other hand, by utilizing the autocorrelation function of dislocation acceleration, Haskell (1966) showed that the source spectrum decreases proportional to cubic power of frequency ( $\omega^{-3}$ ). Several authors compared these two models with the seismological observations and concluded that  $\omega^{-2}$  model represents the high frequency behavior of earthquakes more realistically (Aki, 1967; Brune, 1970; Hanks, 1979). The innovative observations made by Aki (1967) inspired several studies in ground motion simulations providing insight into modeling high frequency behavior of ground motions.

Having accomplished the representation of the spectrum in frequency domain, the most ambiguous part remained to model the source-time function. Among various models in the literature (Haskell, 1964; Aki, 1968), the most popular one is the source model by Brune (1970 and 1971) who related the effective stress available near the fault plane to the source-time function. Later, in their early work, Hanks (1979) and McGuire and Hanks (1980) showed that the application of the Parseval's theorem on the Brune source spectrum results in the far field shear wave root-mean-square acceleration ( $a_{rms}$ ). Through the application of the random-vibration theory (Vanmarcke and Lai, 1980) to the  $a_{rms}$  value, Hanks and McGuire (1981) related this parameter to the peak ground acceleration value. Furthermore, they showed the randomness in high frequency ground motions can be represented with white Gaussian noises.

Boore (1983) combined the source spectrum of Aki (1967) and Brune (1971) with the findings of Hanks and McGuire (1981) and proposed a methodology for generating time-domain simulations. This method represented the faults as stochastic point-sources. Later, Beresnev and Atkinson (1997) applied this methodology to

model finite-faults. The finite-fault model divides a rectangular fault plane into smaller subfaults, each of which is treated as a stochastic point-source, and sums up the contribution of each subfault. This stochastic finite-fault methodology is further developed by Motazedian and Atkinson (2005) with a significant improvement in the definition of corner frequency. The authors modified the definition of the corner frequency to be time-dependent which minimized the significant drawback of subfault dependence in the static corner frequency approach.

The stochastic method has been verified in several studies. Atkinson (1984) and Toro and McGuire (1987) applied this technique to eastern North America whereas Hanks and Boore (1984) and Atkinson and Silva (2000) worked on earthquakes in Western North America. It is also validated globally ranging from studies in Italy (Castro *et al.*, 2001 and 2008; and Galuzzo *et al.*, 2008); Greece (Roumelioti *et al.*, 2004); Iran (Motazedian and Moinfar, 2006; Shoja-Taheri and Ghofrani, 2007) to India (Raghukanth and Somala, 2009). Stochastic strong ground motion simulation method is validated for Turkey as well. Yalcinkaya (2005) applied the method in Adana region whereas Erdik and Durukal (2001) and Durukal (2002) worked in Northwestern Turkey.

Both deterministic and stochastic methods are limited in the frequency range that they are capable of simulating. In order to generate broadband simulations, there are hybrid methods which combine stochastic methods and deterministic methods for the simulation of high and low frequency ground motions, respectively. These hybrid methods are validated by several researchers (Kamae *et al.*, 1998; Pitarka *et al.*, 2000; Hisada and Bielak, 2003).

This study utilizes stochastic finite-fault methodology with a dynamic corner frequency approach to simulate the shear wave portion of high frequency near field ground motions. The method is applied to major earthquakes in Düzce, L'Aquila and Erzincan regions. Additional literature will be cited frequently throughout the text whenever necessary.

### **1.3 Objective and Scope**

This study presents the application of the stochastic ground motion simulation methodology to three regions namely Düzce, L'Aquila and Erzincan. The main objective of this thesis is to study and determine regional source and seismic parameters in the mentioned areas. For this purpose, initially, major past earthquakes occurred in these places are simulated. After the regional parameters are constrained with verification of the synthetics records with the observations, the limitations of the method in terms of simulating directivity effects are investigated. Finally, a parametric sensitivity analysis is performed.

In Chapter 2, the fundamentals of the stochastic finite-fault methodology are introduced. Original theory of the stochastic point-source simulations and its extension to finite-fault case is presented. The alternative approaches taken in the definition of the corner frequencies are discussed.

In Chapter 3, Düzce case study is presented. The regional parameters are validated using the strong ground motion recordings of 1999 Düzce earthquake. Comparisons of synthetics with the observed recordings, damage distribution and GMPEs are presented.

Chapter 4 investigates the seismic parameters of L'Aquila (Italy) region. In order to validate the regional parameters, 1992 L'Aquila earthquake is studied. This earthquake is characterized by strong directivity effects. In this case study, the focus is on the limitations of the method in terms of simulating directivity effects.

In Chapter 5, the methodology is applied to Erzincan region with the simulation of 1992 Erzincan earthquake from which there are only three strong motion records. Initially, the regional parameters are determined using an error minimization algorithm. Later, a sensitivity analysis is performed to observe the variation of simulations with respect to small perturbations in the selected input parameters.

Chapter 6 summarizes the thesis and concludes this study with the observations and future work.

## CHAPTER 2

### STOCHASTIC STRONG GROUND MOTION SIMULATION METHODOLOGY

#### 2.1 General

This chapter presents the stochastic strong ground motion simulation methodology used in this study for simulating large earthquakes in Northwestern and Eastern Turkey, and Central Italy. In section 2.2, stochastic point-source simulation method is presented in detail with the underlying theory. In subsections 2.2.1 to 2.2.4, source, path, site effects and instrument response models are presented with the required input parameters. In section 2.3, stochastic finite-fault simulation method is described in detail with a particular focus on the static and dynamic corner frequency approaches.

#### 2.2 Stochastic Point-Source Modeling

High frequency portion of strong ground motions ( $f > 1$  Hz) are characterized by their complex character. This complexity arises from the loss of phase coherence even between closely spaced stations. Due to the complex phase incoherency, deterministic methods for simulating ground motions (i.e. analytical or numerical solutions of seismic wave propagation equation) are insufficient for high frequencies. In order to model the high-frequency strong ground motions, one or more stochastic parameters are required, which account for the random phase angles (Hanks and McGuire, 1981).

Boore (1983) developed a method for generating acceleration-time series for the S-wave portion of the seismic waves due to point-sources. The method is based on the original findings of Hanks and McGuire (1981) who showed that high-frequency ground motion of shear-waves can be represented as finite duration  $\left(0 \leq t - \frac{R}{\beta} \leq T_d\right)$ , band-limited  $(f_0 \leq f \leq f_{max})$ , white Gaussian noise where  $R$  is the source to receiver distance,  $\beta$  is the shear-wave velocity,  $T_d$  is the faulting duration,  $f_0$  is the corner-frequency of the far-field shear radiation and  $f_{max}$  is the highest frequency recorded by the seismometer. The basic aim of the simulation methodology is to generate a transient time series whose amplitude spectrum in a general sense matches the desired spectrum.

In stochastic point-source modeling of strong ground motions, the first step is to generate random band-limited white Gaussian noise with zero mean and unit variance for a specified finite duration of motion. Then, the generated noise is windowed to give a more realistic shape of an acceleration-time series. The types of windows generally used for this purpose are Saragoni-Hart and boxcar windows. Following this step, the time series is transformed into the frequency domain. In the frequency domain, the noise spectrum is normalized such that Root Mean Square (RMS) spectrum equals unity. The deterministic ground motion spectrum, which is computed theoretically, is multiplied with the RMS of the random signal spectrum. Transformation of the new spectrum back into time domain results in a stochastic acceleration-time series (Boore, 2003). The main steps of the procedure are shown in Figure 2.1.

The theoretical ground motion spectrum is calculated based on the following observations: Using Green's function representation of the elastic wave propagation equation, Haskell (1964) showed that dislocation function of a longitudinal shear fault is equivalent to a distribution of double-couple point-sources over the fault plane. Aki (1967) used the equations of Haskell (1964) for the displacement components of P and S waves at far distances. He expressed the displacement

spectrum as a multiplication of functions representing the source,  $E(\omega)$  and the propagation,  $P(\omega)$  effects in the frequency ( $\omega$ ) domain as given in Equation (2.1):

$$U(\omega) = E(\omega)P(\omega) \quad (2.1)$$

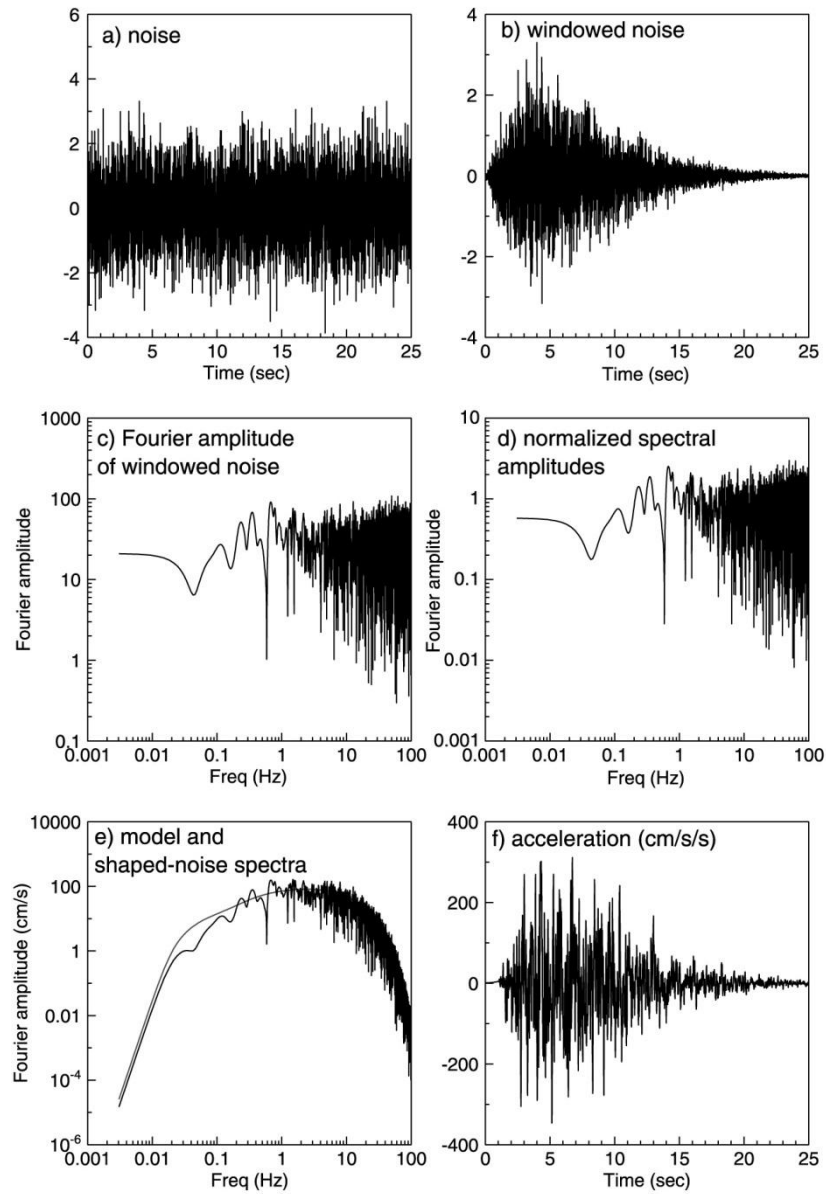


**Figure 2.1** Step by step stochastic point-source modeling procedure (Adapted from Boore, 2003)

The deterministic spectrum, which is multiplied with the normalized noise spectrum, is constituted based on the above representation of the source with the addition of the site effects. The product of filter functions representing source,  $E(M_0, \omega)$  propagation,  $P(R, \omega)$  and site effects,  $G(\omega)$  and the instrument response,  $I(\omega)$  results in the Fourier Amplitude Spectrum of a seismic signal,  $A(M_0, R, \omega)$  as given in Equation (2.2):

$$A(M_0, R, \omega) = E(M_0, \omega)P(R, \omega)G(\omega)I(\omega) \quad (2.2)$$

where  $M_0$  is the seismic moment.

### 2.2.1 The Source Function ( $E(M_0, \omega)$ )

The far-field shear wave displacement in a homogeneous, isotropic, unbounded medium due to a point shear dislocation is given as:

$$\mathbf{u}(\mathbf{x}, t) = \frac{\mathfrak{R}^{\theta\gamma}}{4\pi\rho\beta^3R} M' \left( t - \frac{R}{\beta} \right) \quad (2.3)$$

where  $\mathbf{u}(\mathbf{x}, t)$  is the displacement field at point  $\mathbf{x}$ ,  $\mathfrak{R}^{\theta\gamma}$  is the radiation pattern reflecting the variation of the displacement field for different directions due to a shear dislocation,  $\rho$  is the crustal density,  $\beta$  is the shear-wave velocity which is assumed to be constant at the crustal level,  $R$  is the source to receiver distance and  $M'(t)$  is the time derivative of the seismic moment  $M(t)$  (Aki and Richards, 1980).

In general, seismic moment is represented as:

$$M(t) = \mu\bar{u}(t)A \quad (2.4)$$

where  $\mu$  is the shear modulus or rigidity which is assumed to be constant at the crustal level,  $\bar{u}(t)$  is the source time function and  $A$  is the dislocation area.

The most ambiguous part in the representation of the seismic displacements is the source-time function. There are different approaches to represent displacements across the dislocation plane. Aki (1968) utilized a step function to represent the increase of displacements with time whereas Haskell (1964) assumed a ramp function for the same purpose.

The source-time function used in stochastic modeling belongs to Brune (1970) where the dislocation is modeled as a function of the effective stress that accelerates the sides of the fault. This model assumes that the earthquake dislocation can be represented as a tangential stress pulse  $\sigma(x, t)$  as shown in Equation (2.5), applied to the interior surface of the dislocation surface. This representation is demonstrated in Figure 2.2.

$$\sigma(x, t) = \sigma H\left(t - \frac{x}{\beta}\right) \quad (2.5)$$

In Equation (2.5),  $\sigma$  is the effective stress that acts on the dislocation surface,  $H(t)$  is the Heaviside Step function as given in Equation (2.6):

$$\begin{aligned} H(t) &= 0 & t < 0 \\ H(t) &= 1 & t > 0 \end{aligned} \quad (2.6)$$

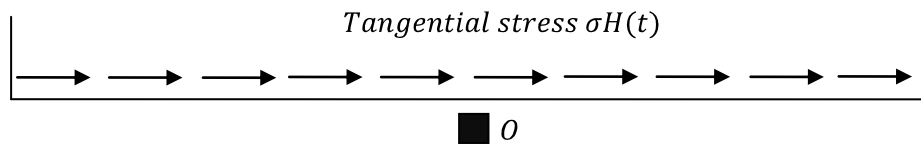


**Figure 2.2** A tangential stress pulse applied to the interior surface of the dislocation surface with the near-field observation point O

Using the stress-strain relationship for an isotropic linear elastic media  $\sigma = \mu \frac{\partial \bar{u}}{\partial x}$ , the tangential displacements occurring due to the tangential shear pulse are obtained as given in Equation (2.7):

$$\begin{aligned} \bar{u}(t) &= 0 \quad t < 0 \\ \bar{u}(t) &= \frac{\sigma}{\mu} \beta t \quad t > 0 \end{aligned} \quad (2.7)$$

In Equation (2.7),  $\bar{u}(t)$  represents the initial particle displacement of a point near the center of the dislocation surface (indicated as Point O in Figure 2.2).

At the near-field observation points, one expects to see a velocity increase in the particle's motion due to the dislocation. After the effects of dislocation are over, the particle velocity will be expected to decrease and become zero at times larger than  $r/\beta$ , where  $r$  is the distance between the near-field observation point O and the edge of the dislocation surface. Since point O is located close to the fault,  $r$  is approximated as fault length divided by 2 (Brune, 1970).

In order to model this effect, an exponential decay function is added to the displacement function. The particle displacement and velocity is modified as follows:

$$\begin{aligned} \bar{u}(t) &= \frac{\sigma}{\mu} \beta \tau \left( 1 - e^{-\frac{t}{\tau}} \right) \\ \bar{u}'(t) &= \frac{\sigma}{\mu} \beta e^{-\frac{t}{\tau}} \end{aligned} \quad (2.8)$$

where time parameter  $\tau$ , controls the rate of displacements.

The displacement function given in Equation (2.8) is a smoothed ramp function and it has a discontinuity at  $t = 0$ . This means infinite stress is needed at the tip of the rupture which is physically unrealistic. Therefore, a modification to the source-time function is needed which will satisfy the boundary condition described above (Beresnev and Atkinson, 1997).

The source-time function that is used in stochastic modeling and its time derivative is expressed as follows:

$$\begin{aligned}\bar{u}(t) &= \frac{\sigma}{\mu} \beta \tau \left[ 1 - \left( 1 + \frac{t}{\tau} \right) e^{-\frac{t}{\tau}} \right] \\ \bar{u}'(t) &= \frac{\sigma}{\mu} \beta \left( \frac{t}{\tau} \right) \left( e^{-\frac{t}{\tau}} \right)\end{aligned}\quad (2.9)$$

We can then represent the total seismic moment as:

$$M_0 = \mu \bar{u}(\infty) A \quad (2.10)$$

where we obtain  $\bar{u}(\infty)$  from Equation (2.9) as  $\bar{u}(\infty) = \frac{\sigma}{\mu} \beta \tau$ .

Combining Equations (2.3), (2.4) with the source-time function described in Equation (2.9), one can obtain the far-field shear wave displacement as follows:

$$\mathbf{u}(\mathbf{x}, t) = \frac{\Re^{\theta\gamma} M_0}{4\pi\rho\beta^3 R \tau} \left( \frac{t - \frac{R}{\beta}}{\tau} \right) e^{-\frac{[t - \frac{R}{\beta}]}{\tau}} \quad (2.11)$$

The Fourier transform of Equation (2.11) yields:

$$\mathbf{u}(\mathbf{x}, \omega) = \frac{\Re^{\theta\gamma} M_0}{4\pi\rho\beta^3 R} \left[ \frac{1}{1 + \left( \frac{\omega}{\omega_c} \right)^2} \right] \quad (2.12)$$

By equating the dislocation source moment and the spectrum at low-frequencies, and conserving the energy-density flux at high-frequency limit for large distances, Brune (1970, 1971) obtained  $\omega_c = 2\pi f_c$  for a circular dislocation area. The corner frequency  $f_c$  is defined as:

$$f_c = 4.9 \times 10^6 \beta \left( \frac{\Delta\sigma}{M_0} \right)^{1/3} \quad (2.13)$$

where  $f_c$  is in Hertz (Hz), shear-wave velocity  $\beta$  is in km/sec, stress drop  $\Delta\sigma$  is in bars and the seismic moment  $M_0$  is in dyne-cm. (Stress drop is explained in detail in Appendix A.)

Equations (2.12) and (2.13) form the basis of the source function. In general, the source function can be written as:

$$E(M_0, \omega) = CM_0 S(\omega, \omega_c) \quad (2.14)$$

In Equation (2.14),  $C$  is the enhanced form of the constants defined in Equation (2.12). It is represented in its general form as:

$$C = \frac{\mathfrak{R}^{\theta\gamma} \cdot FS \cdot PRTITN}{4\pi\rho\beta^3} \quad (2.15)$$

where  $FS$  is the free surface amplification factor whose value is generally assumed to be 2.  $PRTITN$  is a factor that is applied to reflect the effect of shear-wave energy partitioning into two horizontal components and its value is generally taken as  $1/\sqrt{2}$ . The radiation pattern constant  $\mathfrak{R}^{\theta\gamma}$  is generally taken as 0.55 for shear waves.

$M_0$  is the seismic moment of the earthquake. In general,  $M_0 = \mu\bar{u}A$  where  $\mu$  is the shear modulus or rigidity,  $\bar{u}$  is the average slip and  $A$  is the fault area. Moment magnitude  $M_w$ , can be related to the seismic moment by the relationship proposed by Hanks and Kanamori (1979) as:

$$\log M_0 = 1.5 \log M_w + 16.1 \quad (2.16)$$

(For conversions between different magnitude scales, see Appendix B.)

$S(\omega, \omega_c)$  is the displacement spectrum representing the earthquake source. Although there are a variety of functions proposed, the stochastic point-source modeling uses  $\omega$ -squared ( $\omega^{-2}$ ) model due to its accurate prediction of the far-field shear wave spectrum. Based on Equation (2.12) the displacement source spectrum is given as:

$$S(\omega, \omega_c) = \frac{1}{1 + \left(\frac{\omega}{\omega_c}\right)^2} \quad (2.17)$$

The far-field displacement spectrum of ground motions is observed to be constant for low-frequencies where it shows an asymptotic decay proportional to the negative power of frequencies at high frequencies. This behavior of the spectrum is modeled by roughly three parameters namely: low-frequency level which is a function of seismic moment; the corner frequency, which is the intersection frequency of the low and high-frequency asymptotes in the spectrum; and the power of the high-frequency asymptote (Aki and Richards, 1980). This observation on the displacement spectrum of ground motions constitutes the basics of the  $\omega^{-2}$  model.

The source spectrum given by Equation (2.17) is the  $\omega^{-2}$  model. From Equation (2.17) one observes that at the low frequencies ( $\omega \rightarrow 0$ ) the source spectrum decay is dominated by  $\omega_c^{-2}$ , whereas, the spectrum at high frequencies falls off proportional to  $\omega^{-2}$ .

Another popular function for the displacement source spectrum is the two-corner model by Atkinson and Silva (2000) given as:

$$S(\omega, \omega_c) = \frac{1 - \varepsilon}{1 + \left(\frac{f}{f_A}\right)^2} + \frac{\varepsilon}{1 + \left(\frac{f}{f_B}\right)^2} \quad (2.18)$$

where,  $f_A$  and  $f_B$  are the two corner frequencies and  $\varepsilon$  is a region specific weighting parameter with a value varying between 0 and 1.

In stochastic finite-fault modeling of ground motions,  $\omega^{-2}$  model with a single corner frequency is used. This approach has later been improved with a dynamic approach where corner frequency is assumed to be time-dependent. It must be noted that source effects are the most complex and ambiguous of all seismic properties. Thus, performance of any wave propagation simulation is dependent on the accuracy of seismic source definitions.

### **2.2.2 The Path Function ( $P(R, \omega)$ )**

As the seismic waves travel through the Earth, they are exposed to various processes that change not only their amplitudes but also frequency contents, velocities and durations. One can group these processes in two categories as elastic and anelastic processes. Geometric spreading, scattering and multipathing are elastic processes where the seismic energy is assumed to be conserved. On the other hand in anelastic attenuation, some of the seismic energy is lost in the form of heat energy generally due to material imperfectness (Stein and Wysession, 2003).

Geometric spreading is a factor that reflects the reduction in wave amplitudes due to the distance travelled. In a homogeneous spherical Earth, body wave amplitudes decay inversely proportional to the distance,  $R$ . In reality, since the Earth is not homogeneous and has an ellipsoidal shape, geometric spreading can be different than  $1/R$ .

The heterogeneities existing in the Earth, cause the waves to focus or defocus. In general, waves tend to focus on the low-velocity discontinuities and escape from high-velocity discontinuities. The changes in the behavior of waves due to velocity heterogeneities are called scattering and multipathing. In the absence of these processes, direct arrivals of the waves from the source to receivers are observed in the seismograms. When different arrivals are observed in the seismograms, it is inferred that waves have taken different paths which are indicators of the scattering

and multipathing processes. (Stein and Wysession, 2003). These two processes have the similar effect of enhancing the duration of the waves.

Since the Earth is not perfectly elastic, waves are exposed to damping as they travel along the Earth. Due to the material properties of the medium that waves travel through, the spectral amplitudes of the waves decrease. This type of damping is named as “anelastic” or “intrinsic attenuation” and parameterized by the quality factor,  $Q$  (Lay and Wallace, 1995). Different parts of the world have different  $Q$  values depending on their seismotectonic features (Aki, 1980). Figure 2.3 shows variation of  $Q$  with respect to frequency for different parts of the world.

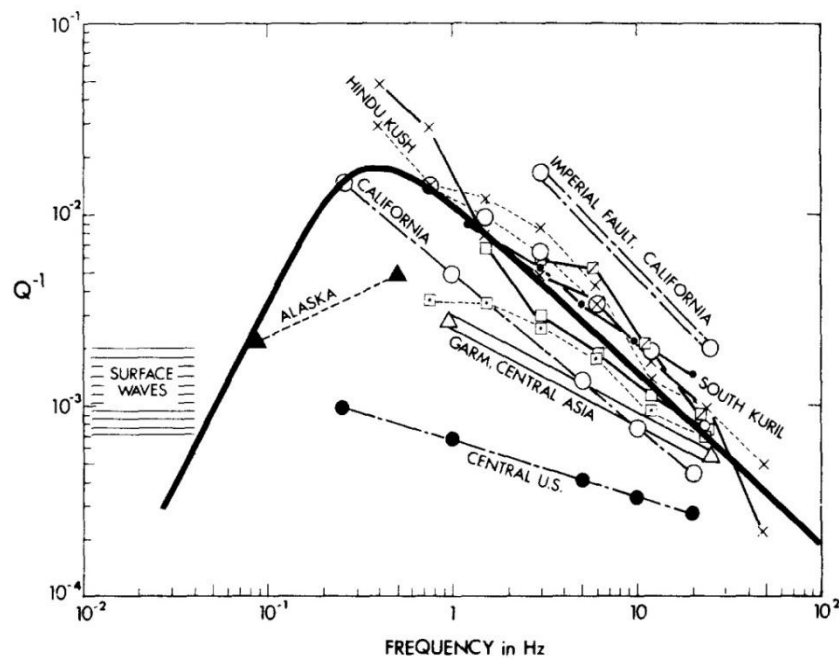


**Figure 2.3**  $Q$  versus frequency for different parts of the world (Adapted from Boore, 1984)

In general, Q value does not depend on frequency for  $f < 1$  Hz. For higher frequencies, Q is frequency-dependent and increases with increasing frequency as  $Q = Q_0 f^n$ . The constant  $Q_0$  reflects the heterogeneities in the medium and n is directly proportional to the seismicity of the region (Raghukanth and Somala, 2009). When the quality factor, Q of a region is small, the waves travelling in that region are exposed to higher attenuation and the wave amplitudes are observed to decrease quickly. In stochastic modeling of ground motions, the path effects are modeled as:

$$P(R, \omega) = Z(R) e^{-\frac{\pi f R}{Q(f)\beta}} \quad (2.19)$$

In Equation (2.19),  $Z(R)$  represents geometric spreading. It is defined to be a piecewise continuous function as given in Equation (2.20) (Boore, 2003):

$$Z(R) = \left\{ \begin{array}{ll} \frac{R_0}{R} & R \leq R_1 \\ Z(R_1) \left(\frac{R_1}{R}\right)^{p_1} & R_1 \leq R \leq R_2 \\ \vdots & \vdots \\ Z(R_n) \left(\frac{R_n}{R}\right)^{p_n} & R \leq R_n \end{array} \right\} \quad (2.20)$$

where R is the source to receiver distance.

The anelastic attenuation is represented by the  $e^{-\frac{\pi f R}{Q(f)\beta}}$  term where  $Q(f)$  is the frequency-dependent quality factor. This is a significant term since the shape of the high-frequency spectrum is specified by the anelastic attenuation (Motazedian, 2006).

In practice, neither source nor the medium properties that the seismic waves travel through are easy to measure or quantify. The major source of information is the recorded seismograms which reflect the combined effects of the source and propagation characteristics. In order to determine the regional parameters, one needs to analyze the seismograms. But since both the source and path effects are not perfectly known, assumptions are made which eliminates a group of unknown

regional parameters. To derive the best estimate of the parameters such as  $Q$  and geometric spreading, methods such as forward fitting, inversion or regression are utilized on the Fourier spectrum of the actual recordings. Since the results will depend directly on the methodology and dataset utilized in the derivation process, it is always possible to find alternative values proposed for the same region in the literature. Figure 2.4 illustrates the  $Q(f)$  values proposed for the Marmara region of Turkey by different researchers along with a generic model by Boore (1984).

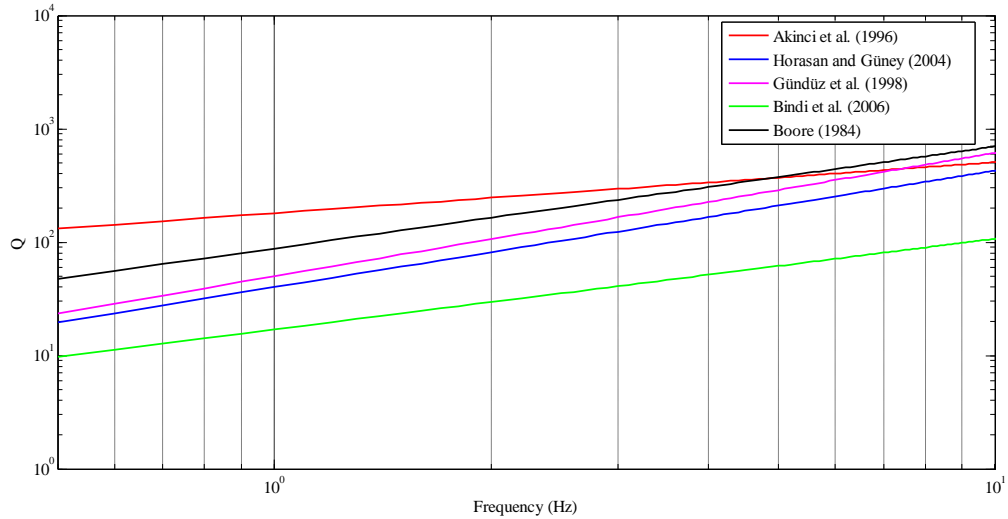


**Figure 2.4** Alternative  $Q(f)$  values for the Marmara region, Turkey.

Another parameter in stochastic modeling of ground motions that reflects the propagation effects is the distance-dependent duration. It does not affect the deterministic spectrum directly through Equation (2.12). But it affects the time-domain representation of the synthetic signal since peak amplitudes decay with increasing duration. The duration model in its general form is given as:

$$T = T_0 + bR \quad (2.21)$$

where  $T_0 = \frac{1}{\omega_c}$  is the source duration. The distance-dependent duration term,  $bR$  where  $R$  is the hypocentral distance, is added to account for the enhancement of duration due to scattering and multipathing processes (Beresnev and Atkinson, 1997).

### 2.2.3 The Site Function ( $G(\omega)$ )

Local soil conditions have significant effects on ground motions characteristics. Soil layers underneath a site modify the frequency content, amplitude and duration of the seismic waves that travel through them. The difference in seismic impedance (defined as  $Z = \rho\beta$ ) between two soil layers is known to affect the amplitudes of the seismic waves. Seismic impedance can be viewed as the resistance of the medium to the particle movement (Yalçinkaya, 2004). Going from bedrock to the surface, the density and velocity of soil layers generally decrease. When waves travel up in the Earth, since the seismic impedance decreases, particle velocity thus wave amplitudes must increase in order to conserve the elastic wave energy (Kramer, 1996). As an example, soft alluvial deposits are known to cause an increase in the amplitude and duration of the seismic waves.

Modeling of local soil conditions plays a very important role in ground motion simulations. In stochastic simulation of ground motions, site effects are represented as:

$$G(\omega) = A(\omega)P(\omega) \quad (2.22)$$

where  $A(\omega)$  is the amplification of seismic waves due to velocity contrast between layers and  $P(\omega)$  is the diminution factor reflecting the loss of energy. It must be noted that site effects are separated from the path effects, thus the amplification and diminution factors are not related to the characteristics of the medium between the source and the site.

## **i. Amplification Factors**

Determining soil types and site amplification is a fundamental step in ground motion simulations. Among various methods for determining site response, the most accurate assessment of site amplifications can be made if the velocity profile of the local soil layers is known. Seismic reflection, refraction and borehole drilling are among the most popular methods used in the derivation of the velocity profiles. When the wave velocity profile of a region is known, one can determine the amplification factors using theoretical transfer functions. These transfer functions can be computed once the one-dimensional (1D) (Haskell, 1960; Kennett, 1983), two-dimensional (2D) (Sanchez-Sesma, 1987) or three-dimensional (3D) (Pitarka *et al.*, 1998) models of the soil medium are specified.

Measuring S-wave velocities using the aforementioned methodologies (seismic reflection, refraction and borehole drilling) are expensive and difficult. In addition, velocity profiles down to the bedrock level cannot be easily extracted for deep basins. Another alternative is measuring surface waves which consist of a broad range of frequencies. With the high frequency portion, one can readily monitor the shallower layers. Using the low frequency portion of the surface wave measurements, which can penetrate into deeper layers, one can as well extract the deeper profile. Sources of these waves can be “active sources” like hammers, weight drops, electromechanical shakers, seismic vibrators and bulldozers. Spectral analysis of surface waves (SASW) (Stokoe *et al.*, 1994) and Multi-Channel array surface waves (MASW) (Park *et al.*, 1999) are two popular techniques where the theoretical dispersion curve of a proposed velocity profile is to be matched with the measured dispersion curve by a series of iterations (Rosenblad and Li, 2009).

Another source of surface waves can be microtremors or ambient noise. When ambient vibration of Earth is measured and analyzed, it is called “passive seismic” methods. Passive refraction microtremor (ReMi) (Louie, 2001), frequency-wavenumber (f-k) (Schmidt, 1986) and spatially averaged coherency (SPAC) (Asten *et al.*, 2003) are methods used in the evaluation of passive measurements. SPAC

technique is based on the findings of Aki (1957) which state that the coherency spectrum averaged over the azimuth angles has the shape of the Bessel function of the first kind and zero order. In this technique, theoretical coherency curves are iteratively fitted to the measured coherency curves in order to obtain the shear wave velocity profile of interest (Claprod and Asten, 2007).

An alternative method for computing the site response is the quarter wavelength approximation. The amplification corresponding to some particular frequency is given by the square root of the ratio of the seismic impedance corresponding to the depth of source ( $\rho_s \beta_s$ ) to the average seismic impedance calculated over a depth corresponding to a quarter of wavelength ( $\bar{\rho}(z) \bar{\beta}(z)$ ) (Joyner and Fumal, 1985; Boore and Joyner, 1997) as given in Equation (2.23):

$$A[f(z)] = \sqrt{\frac{\rho_s \beta_s}{\bar{\rho}(z) \bar{\beta}(z)}} \quad (2.23)$$

In case where velocity profile is unknown, the most common method in determining the local soil amplification factors is the horizontal-to-vertical ratio (H/V) method (Nakamura, 1989). H/V method is based on the observation that vertical component of the seismic waves are not exposed to local soil effects to the extent that the horizontal components are. In other words, the vertical component of the ground motion at the ground surface is almost identical to the vertical component measured at the rock level. Thus, by dividing the horizontal component to the vertical component both measured at the surface, it is possible to eliminate the complicated source and propagation effects. What is left is the local soil amplification that the horizontal component is exposed to. Weak motion records, strong motion records of aftershocks and mainshocks as well as microtremor measurements can be used as input when determining site amplification factors with H/V method. Various authors utilized H/V method for determining local site effects and verified its success in predicting site response (Lermo and Chaves-García, 1994; Suzuki *et al.*, 1995; Huang and Teng, 1999; Raghukanth and Somala, 2009).

Another popular method for estimating site response in the absence of wave velocity profiles is the standard spectral ratio (SSR) method. In this method, a very hard rock site is chosen as the reference site having negligible local site effects. Dividing the Fourier spectrum of any soil site to the Fourier spectrum of this reference site, one eliminates the source and propagation effects and left is the site response function (Borcherdt, 1970).

The aforementioned techniques are all suitable for determining the site amplification factors for simulation purposes. In this study, H/V method is used for Düzce region whereas quarter wavelength approach with generic amplification factors determined by Boore and Joyner (1997) is utilized for Erzincan and L'Aquila regions.

## ii. Diminution Factors

The rapid decay of the spectral values in the high-frequencies is not due to the attenuation during wave propagation (Boore, 1983). Papageorgiou and Aki (1983) state that this loss is due to the source processes; whereas Hanks (1982) and Atkinson (2004) attribute this effect to near-site conditions. While the cause is open to discussion, there are two basic filters that account for the spectral loss at frequencies above some cut-off frequency. The first one is the  $f_{max}$  filter (Hanks, 1982) where  $f_{max}$  is defined as the cut-off frequency. The diminution filter is given as:

$$D(f) = \left[ 1 + \left( \frac{f}{f_{max}} \right)^8 \right]^{-1/2} \quad (2.24)$$

In case the operator  $\kappa_0$ , which reflects the spectral decay at high frequencies, is used, the alternative diminution filter is defined as follows:

$$D(f) = e^{-\pi\kappa_0 f} \quad (2.25)$$

Anderson and Hough (1984) characterize the spectral decay at short periods as an exponential function of the kappa values. The Fourier acceleration spectrum of each record is plotted in semi-logarithmic scale. Best-fit line is obtained to the decaying portion of the spectrum. Dividing the negative of the slope of the best-fit line to  $\pi$ , the kappa factors of the individual stations are obtained. Afterwards, the calculated kappa values are plotted against the epicentral distances of the stations and the equation of the line that fits to the distribution is determined. The ordinate of this best-fit line gives the zero-distance kappa ( $\kappa_0$ ) value in the region of interest. In the simulations  $\kappa_0$  values are used as the near-surface attenuation factor in order to eliminate the effect of distance since the attenuation effects that are occurring due to distance travelled are already contained in the path model (Margaris and Boore, 1998).

Figure 2.5 shows the effects of different  $\kappa_0$  values on the Fourier Amplitude spectrum of the synthetic ground motions.

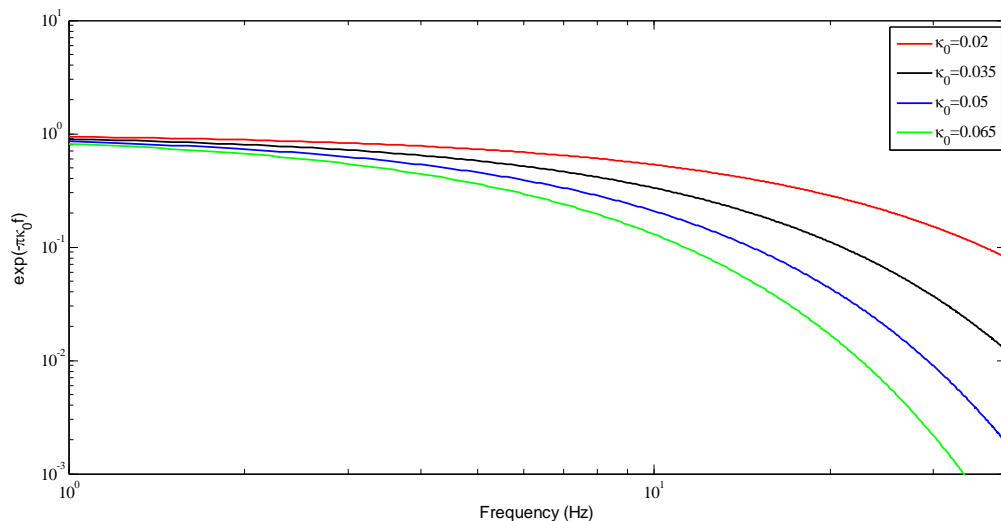


**Figure 2.5** The effects of different  $\kappa_0$  values on the spectrum

#### 2.2.4 Type of Ground Motion ( $I(\omega)$ )

The output of the simulations can be ground motion displacement, velocity, acceleration or response of an oscillator. The filter  $I(\omega)$  controls the type of the ground motion.

To obtain the required ground motion time series, one needs to use  $n = 0, 1$  or  $2$  for ground displacement, velocity and acceleration, respectively in Equation (2.26) (Boore, 2003).

$$I(f) = (2\pi f i)^n \quad (2.26)$$

where  $i$  is the imaginary unit.

To find the response of an oscillator,  $I(f)$  is used as:

$$I(f) = \frac{-V f^2}{(f^2 - f_r^2) - 2f f_r \zeta i} \quad (2.27)$$

where  $f_r$  is the undamped natural frequency of the oscillator,  $\zeta$  is the damping and  $V = 1$  for the response spectra (Boore, 2003).

### 2.3 Stochastic Finite-Fault Modeling

Stochastic point-source simulations are particularly successful for observation points that are located at distances greater than the larger dimension of the fault plane. However, to predict the ground motion field at near-source observation points, one needs to take into account finite dimensions of the fault plane. Beresnev and Atkinson (1997) proposed the stochastic finite-fault simulation method which discretizes the fault plane into smaller subfaults and sum the contribution of the subfaults where every subfault is treated as stochastic point-source. The idea of

discretizing large events and superimposing the contribution of every small element in the discretized space has its origins in the work of Hartzell (1978).

In stochastic finite-fault modeling, the fault is assumed to be a rectangular plane with dimensions representing rupture width and length. The fault plane is divided into smaller subfaults and every subfault is assumed to be a point-source with an  $\omega^{-2}$  spectrum. The hypocenter is placed on one of the subfaults and the rupture is assumed to start propagating radially from the hypocenter with a constant rupture velocity,  $v_r$ . As the rupture reaches the center of a subfault, that subfault is assumed to be triggered. In this way, the contribution of all subfaults is summed with appropriate time delays in order to obtain the entire fault plane's contribution to the seismic field at the observation point (Atkinson *et al.*, 2009):

$$a(t) = \sum_{i=1}^{nl} \sum_{j=1}^{nw} a_{ij}(t - \Delta t_{ij} - T_{ij}) \quad (2.28)$$

In Equation (2.28),  $a(t)$  is the ground motion acceleration obtained from the entire fault whereas  $a_{ij}$  is the ground motion acceleration obtained from the  $ij^{\text{th}}$  subfault.  $nl$  and  $nw$  are the number of subfaults along the length and width of main fault respectively.  $T_{ij}$  is a fraction of rise time of a subfault where rise time is defined as the subfault radius divided by the rupture velocity (Atkinson *et al.*, 2009). The time delay for each element  $\Delta t_{ij}$ , is the summation of the time required for the rupture front to reach the element and the time required for the shear-wave to reach the receiver after the element has been triggered (Beresnev and Atkinson, 1997). The general outline of the methodology is shown in Figure 2.6.

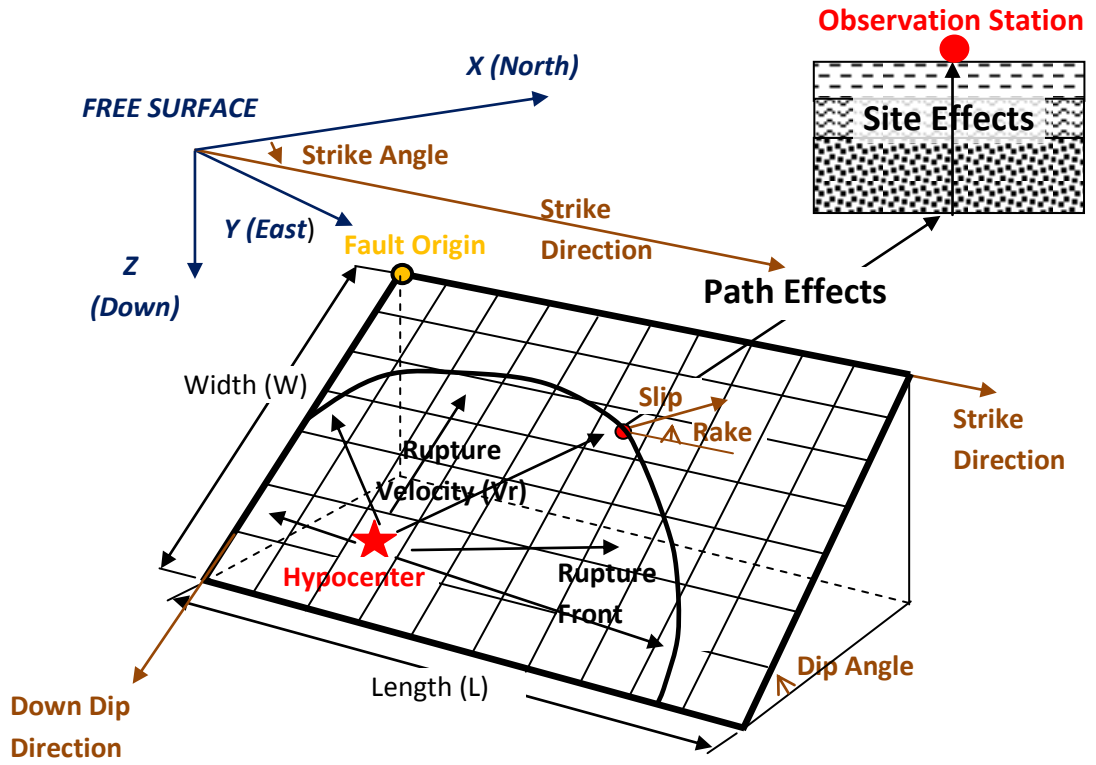


**Figure 2.6** Stochastic finite-fault methodology (Adapted from Hisada, 2008)

The distribution of slip values along the fault plane can be assumed to be homogeneous. In this case, the moment of each subfault is then defined as follows:

$$M_{0ij} = M_0/N \quad (2.29)$$

where  $N$  is the number of subfaults. If the subfaults are not identical, the distribution of the seismic moment among the subfaults is based on the slip weights (Motazedian and Moinfar, 2006). The moment of each subfault is defined as:

$$M_{0ij} = \frac{M_0 S_{ij}}{\sum_{k=1}^{nl} \sum_{l=1}^{nw} S_{kl}} \quad (2.30)$$

where  $S_{ij}$  is the relative slip weight of the  $ij$ th subfault.

In their early work, Beresnev and Atkinson (1997) defined the acceleration spectrum of a subfault  $ij$ ,  $A_{ij}$  to be exactly the same with that of stochastic point-source:

$$A_{ij}(f) = CM_{0ij} \frac{(2\pi f)^2}{\left[1 + \left(\frac{f}{f_{c_{ij}}}\right)^2\right]} \frac{1}{R_{ij}} e^{-\frac{\pi f R_{ij}}{Q\beta}} D(f) e^{-\pi\kappa f} \quad (2.31)$$

And the corner frequency of a subfault,  $f_{c_{ij}}$  is defined as:

$$f_{c_{ij}} = 4.9 \times 10^6 \beta \left(\frac{\Delta\sigma}{M_{0ij}}\right)^{1/3} \quad (2.32)$$

The computer program utilizing the above mentioned methodology by Beresnev and Atkinson (1997) is named FINSIM (Beresnev and Atkinson, 1998a and 1998b).

The synthetic ground motions generated using FINSIM and the above definition of corner frequency with the acceleration spectrum defined in Equation (2.31), are recently shown to be dependent on the subfault size or the number of subfaults. This drawback is overcome by the work of Motazedian and Atkinson (2005) who implemented a dynamic corner frequency approach in an updated computer program named as EXSIM. In this approach, the corner frequency at any time is defined to be inversely proportional to the area of the subfaults that have ruptured up to that time. For example, if the rupture stops at the end of the  $N^{\text{th}}$  subfault, then corner frequency is proportional to the inverse of the area of  $N$  subfaults. Since the number of ruptured subfaults changes with time, the corner frequency becomes time-dependent and decreases with increasing duration. The dynamic corner frequency is defined as follows:

$$f_{c_{ij}}(t) = N_R(t)^{-1/3} 4.9 \times 10^6 \beta \left(\frac{\Delta\sigma}{M_{0ave}}\right)^{1/3} \quad (2.33)$$

where  $N_R(t)$  is the cumulative number of ruptured subfaults at time  $t$ ,  $M_{0_{ave}} = M_0/N$  is the average seismic moment of subfaults.

An important observation is that in this new formulation, as rupture progresses, the ruptured area increases which in turn decreases the corner frequency and the radiated energy at high frequencies. In order to conserve the radiated energy at high frequencies, Motazedian and Atkinson (2005) applied a scaling factor  $H_{ij}$  to the spectrum. The new acceleration spectrum with the  $H_{ij}$  formulation is as follows:

$$A_{ij}(f) = CM_{0_{ij}}H_{ij} \frac{(2\pi f)^2}{\left[1 + \left(\frac{f}{f_{c_{ij}}}\right)^2\right]^2} \frac{1}{R_{ij}} e^{-\frac{\pi f R_{ij}}{Q\beta}} e^{-\pi\kappa f} \quad (2.34)$$

$$H_{ij} = \left\{ N \frac{\left( \sum \left[ \frac{f^2}{1 + \left(\frac{f}{f_c}\right)^2} \right]^2 \right)^{1/2}}{\left( \sum \left[ \frac{f^2}{1 + \left(\frac{f}{f_{c_{ij}}}\right)^2} \right]^2 \right)^{1/2}} \right\}$$

Another modification is the implementation of pulsing subfaults concept by Motazedian and Atkinson (2005). This concept is inspired from the “self-healing model” of Heaton (1990) who showed that slip duration on any part of the fault can be shorter than the duration of rupture. This new modification is based on the reasoning that slip is observed to stop at the points near the nucleation point when rupture reaches the end of the fault plane especially at large ruptures. Pulsing subfault concept assumes that rupture starts and builds up until a specified percentage of the subfaults are ruptured. Subsequently, the cumulative number of subfaults that are rupturing becomes constant. Thus, the cells that are actively pulsing contribute to the dynamic corner frequency whereas no contribution comes from the passive cells. This behavior gives a decreasing corner frequency until pulsing area percentage is reached. Afterwards the dynamic corner frequency

becomes constant. The parameter that controls the percentage of the maximum ruptured area is called pulsing area percentage. Decreasing the pulsing area percentage tends to lower the spectrum at long periods. Among all the simulation parameters, pulsing area percentage along with the stress drop is one of the two free parameters that are capable of changing the amplitude of the spectrum.

In the next chapters, application of the stochastic finite-fault methodology using dynamic corner frequency approach to three different earthquakes is presented in detail.

## CHAPTER 3

### GROUND MOTION SIMULATION OF THE 1999 DÜZCE EARTHQUAKE: A VALIDATION STUDY

#### 3.1 General

This section presents stochastic finite-fault simulation of the ground motions from the 12 November 1999 Düzce earthquake at selected near-fault stations. The main objective of this case study is not to regenerate the records blindly but to investigate the regional parameters. The missing regional parameters are obtained by the verification of simulation results against the records from the 1999 Düzce earthquake.

Sections 3.2 and 3.3 give background information about the 1999 Düzce Earthquake and the strong ground motion stations that recorded the mainshock of the event. Section 3.4 presents the seismological parameters that are used in the simulations. In Section 3.5, results of the simulations and discussions of results are presented.

#### 3.2 Background Information

An earthquake of  $M_w=7.1$  occurred on the Düzce segment of North Anatolian Fault Zone on 12 November 1999 (Earthquake Research Department of the (abolished) General Directorate of Disaster Affairs, Turkey (ERD)) only three months after the nearby  $M_w=7.4$  17 August 1999 Kocaeli earthquake (Kandilli Observatory and Earthquake Research Institute of Bogazici University (KOERI)). These two

earthquakes caused extensive damage to the surrounding cities which contain significant industrial facilities.

Most parts of Turkey are located on the Anatolian plate. The movement of the Anatolian plate is governed by the collision of relative northward movement of Arabian and Eurasian plates. This collision formed the major tectonic structures of Anatolian plate, namely North Anatolian Fault Zone (NAFZ) and East Anatolian Fault Zone (EAFZ) (Figure 3.1, top panel). EAFZ is left-lateral strike slip in nature and has an extrusion of  $18\pm 6$  mm/year (Stein *et al.*, 1997). It generated smaller earthquakes compared to NAFZ in the past century; however, paleoseismological records evidence that EAFZ also produced several destructive earthquakes (Ambraseys, 2009). NAFZ and EAFZ join together at the Karliova junction. From Karliova, NAFZ extends 1500 km to the Marmara Sea. Right-lateral strike slip NAFZ is the major tectonic structure of Anatolian plate with a westward extrusion of  $24\pm 4$  mm/year (Stein *et al.*, 1997). The destructive westward migrating earthquake sequence of NAFZ started with the great 1939 Erzincan earthquake (surface wave magnitude,  $M_s=8.0$ ) in the very Eastern segment of the fault zone. The latest of this sequence are the Düzce and Kocaeli Earthquakes. These earthquakes are of significance due to the extensive damage they caused to the neighboring regions which are among the densely populated and heavily industrialized regions of Turkey. Furthermore, these earthquakes attract the particular attention of seismological community due to the debates on whether Düzce event is an aftershock of the Kocaeli earthquake. Another significant feature of these two earthquakes is that supershear rupture phenomenon (where the rupture velocity is greater than the shear wave velocity of the fault material) is observed in the recordings of the two events.

Figure 3.1, bottom panel shows the seismicity map of the region within the last century and the neighboring active faults (Şaroğlu *et al.*, 1992) with the red star indicating the epicenter of 1999 Düzce earthquake.

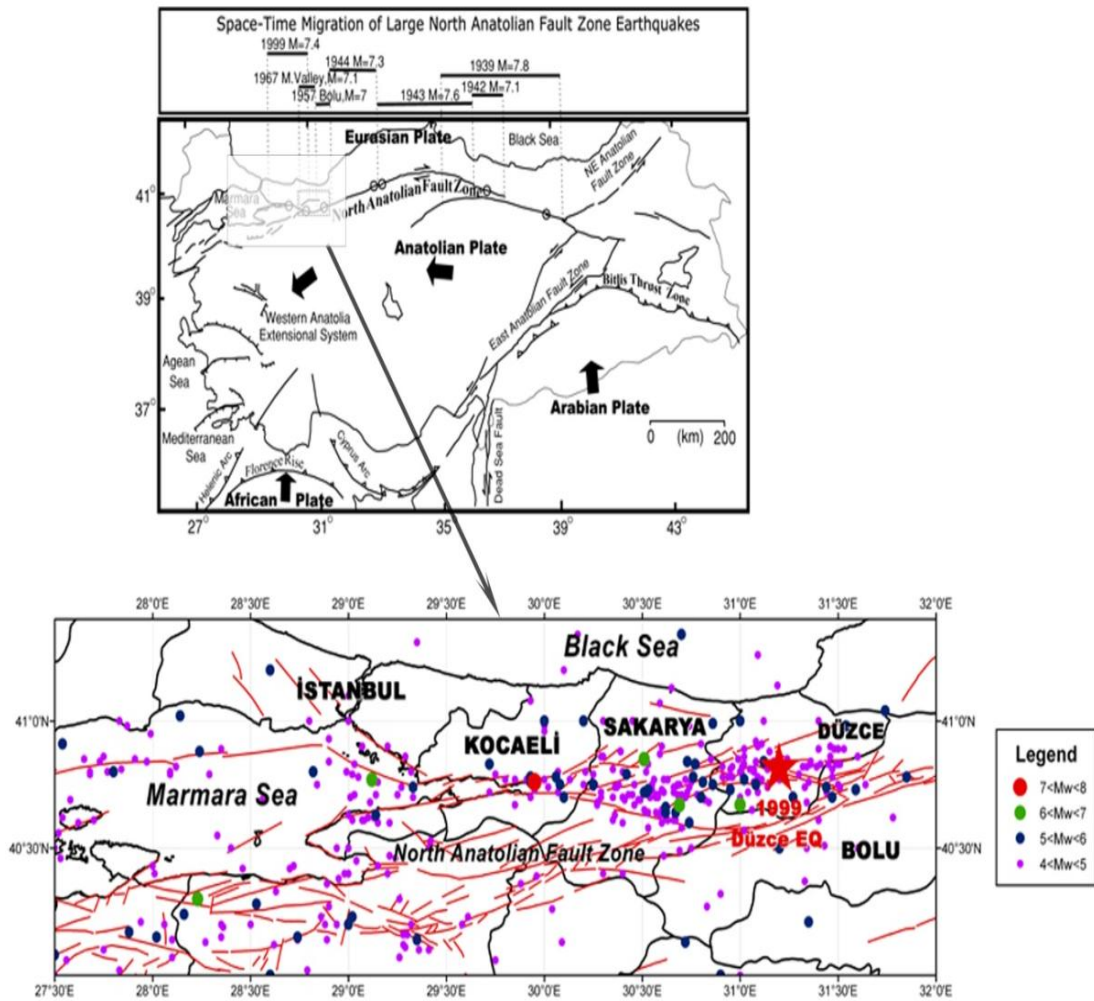


**Figure 3.1** Top panel: Tectonic map of Turkey and the westward migration of major earthquakes on the NAFZ. The top panel is adapted from Utkucu *et al.* (2003). Bottom panel: Seismicity map of the Marmara region with the neighboring active faults indicated with solid red lines. The catalog information of the earthquakes is obtained from KOERI, <http://www.koeri.boun.edu.tr/sismo/default.htm>.

The 12 November 1999 Düzce earthquake was reported to have epicentral coordinates of  $40.82^{\circ}\text{N}$ ,  $31.20^{\circ}\text{E}$  (ERD) with a focal depth of 12.5 km (Milkereit *et al.*, 2000). The strike, dip and rake angles of the event were  $264^{\circ}$ ,  $64^{\circ}$  and  $-172^{\circ}$ , respectively (Umutlu *et al.*, 2004). The fault plane was dipping to the North whereas

rupture propagation was to the East. The earthquake is characterized as bilateral fault rupture by several researchers (Burgmann *et al.*, 2002; Cakir *et al.*, 2003; Utkucu *et al.*, 2003; Bouin *et al.*, 2004).

Significant structural damage is observed in the near-fault region. The earthquake caused 763 fatalities and 4948 injuries. Among approximately 122500 damaged residential and office buildings, 32000 of them are either severely damaged or collapsed (Özmen and Bagci, 2000).

The geology of the region that is mostly affected by the earthquake shows significant variations. Mountain ranges characterized as Mesozoic bedrock are present next to pull-apart basins formed by the NAF system. Düzce and Bolu basins are the major alluvial basins affected by the earthquake in addition to Kaynaşlı town located to the east of the fault where there was a concentrated building damage and 313 fatalities. (Rathje *et al.*, 2006).

### **3.3 Strong Ground Motion Data**

At the time of the earthquake, thirty-two strong ground motion stations were operating within an epicentral distance range of 200 km. These strong ground motion stations belong to ERD, KOERI and Istanbul Technical University (ITU) (Durukal, 2002). The instruments are of the GSR-16, SMA-1 and SSA-2 type accelerographs installed on the basement or lower floors of low-rise buildings mostly founded on deep alluvium as typical of the local geology. The stations at closest distance from the fault rupture are Bolu (BOL, rupture distance,  $R_{rup}=8.55$  km) and Düzce (DZC,  $R_{rup}=9.71$  km) stations which are both located in the meizoseismal area (Ugurhan and Askan, 2010).

In this study, nine of the strong ground motion stations located within an epicentral distance range of 125 km are utilized. Figure 3.2 shows the distribution of the strong ground motion stations used in this study with black triangles. The codes of the

stations that lie in the epicentral distance range of 125 km are indicated on the figure. Also presented in Figure 3.2 are the epicenters of the Düzce (solid black star) and Kocaeli (empty star) earthquakes, orientation of the fault plane and focal plane solution. Slip distribution values computed by Umutlu *et al.* (2004) are also shown in the bottom part of Figure 3.2.

Table 3.1 gives information on the strong ground motion stations utilized in this study. Station names, codes, operating institutes, coordinates of the stations, site classes according to NEHRP classification, distance of the station with respect to the epicenter of the earthquake and peak ground acceleration values observed in both horizontal components of the recordings are given in Table 3.1. The sampling periods of the stations are either 0.005 or 0.01 sec. The data are baseline corrected and band-pass filtered using a forth-order Butterworth filter within the frequency band of 0.25-25 Hz.

**Table 3.1** Information on the strong motion stations that recorded the 1999 Düzce earthquake

Station Name	Operator Code	Operator Name	Latitude (°N)	Longitude (°E)	Site Class	Epicentral	PGA	PGA
						Distance (km)	(NS) (cm/s <sup>2</sup> )	(EW) (cm/s <sup>2</sup> )
Bolu	BOL	ERD	40.747	31.610	D	39.026	715.38	771.28
Düzce	DZC	ERD	40.740	31.210	D	9.314	360.04	463.81
Gölcük	GLC	ITU	40.726	29.815	D	112.513	35.56	47.58
Göynük	GYN	ERD	40.385	30.734	D	55.163	26.04	23.19
İzmit	IZN	ERD	40.440	29.750	D	123.663	19.53	20.96
İzmit	IZT	ERD	40.790	29.960	C	100.169	17.55	16.73
Mudurnu	MDR	ERD	40.463	31.182	D	34.073	121.91	54.18
Sakarya	SKR	ERD	40.737	30.384	C	64.518	14.52	24.52
Yarımca Petkim	YPT	KOERI	40.740	31.210	D	116.853	20.70	14.73

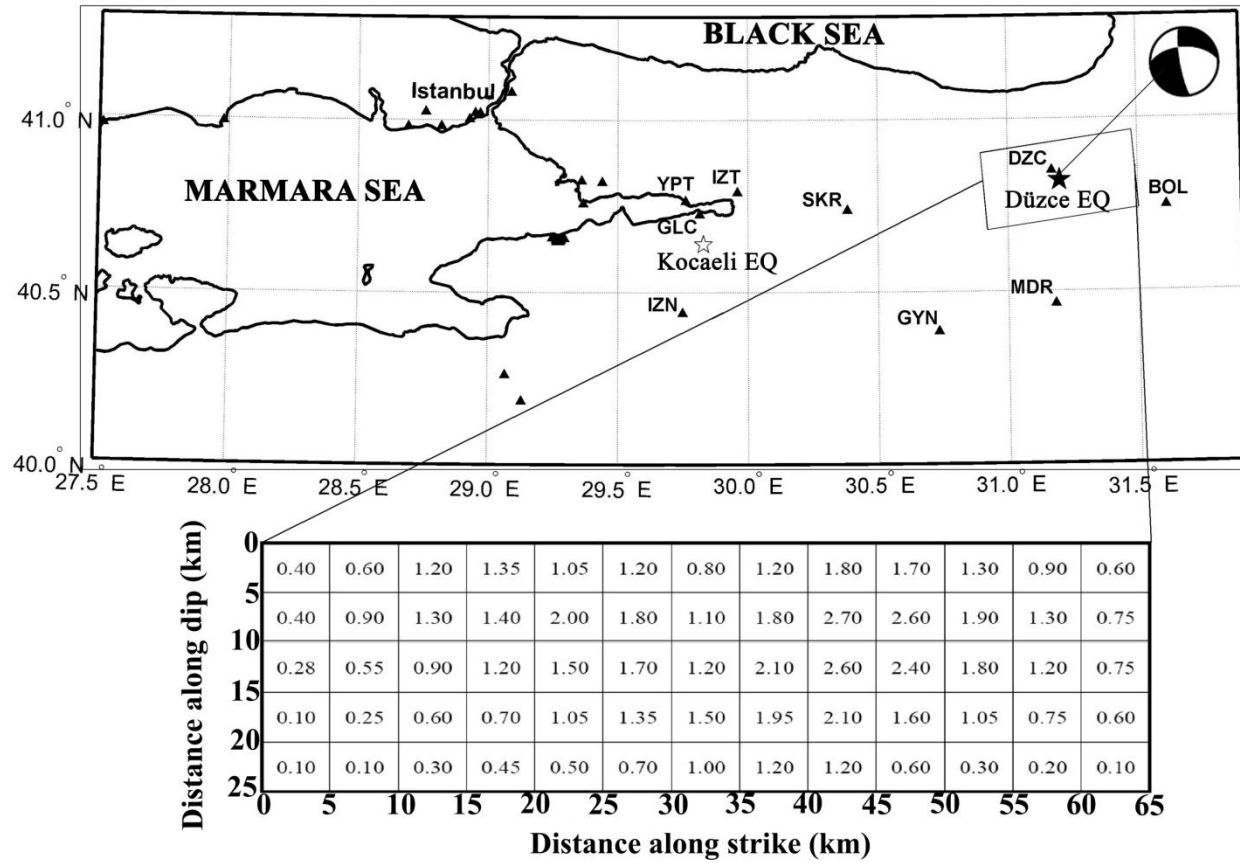


**Figure 3.2** Map showing the regional setting and slip distribution (bottom table) of 12 November 1999 Düzce earthquake

### 3.4 Model Parameters

In stochastic finite-fault modeling, parameters defining the source, path and site properties of the target region are required to generate reliable ground motions. Therefore, in general it is essential to use regional parameters instead of generic ones. But in regions where regional seismological studies do not exist, generic parameters need to be utilized. This section describes the derivation of the regional parameters defining the ground motion characteristics in the Marmara region.

The input parameters defining the source model in stochastic ground motion simulations are the dip and strike angles, length and width of the rupture plane, hypocentral depth and coordinates, slip distribution along the fault plane, stress drop and the pulsing area percentage. The dip, strike angles, hypocentral coordinates and depth are well constrained by the focal plane solutions. The only parameters that can vary are the dimensions of the fault plane, stress drop and pulsing area percentage. In this study, initially the path and site effects and the source parameters other than stress drop and pulsing area percentage are constrained. Afterwards an error minimizing algorithm is formed to calculate the two most uncertain but significant parameters of interest, namely the stress drop and pulsing area percentage.

To determine the fault plane and the associated slip values, different models (Yagi and Kikuchi, 1999; Burgmann *et al.*, 2002; Cakir *et al.*, 2003; Utkucu *et al.*, 2003; Bouin *et al.*, 2004, Birgoren *et al.*, 2004 and Delouis *et al.*, 2004; Umutlu *et al.*, 2004) computed for this particular earthquake are tested in this study using the computer program EXSIM. Among the various models listed, the slip model proposed by Umutlu *et al.* (2004) minimized the overall error between the observed and synthetic Fourier amplitude spectra of the nine stations considered. The model of Umutlu *et al.* (2004) is based on the joint inversion of strong ground motion and teleseismic records of the 1999 Düzce earthquake. The proposed fault model has dimensions of 65 x 25 km and the slip distribution values as indicated in Figure 3.2. The fault plane is divided into smaller subfaults having dimensions of 13 x 5 km along the strike and dip directions, respectively.

To define the path model, geometric spreading, anelastic attenuation (quality factor) and distance-dependent duration model are required as input parameters. To begin with the path parameters, geometric spreading model proposed by Ansal *et al.* (2009) for the Marmara region (Equation (3.1)) is used in the simulations. The mentioned model is as follows:

$$\begin{aligned}
 R^{-1} & \quad R \leq 30 \text{ km} \\
 R^{-0.4} & \quad 30 < R \leq 60 \text{ km} \\
 R^{-0.6} & \quad 60 < R \leq 90 \text{ km} \\
 R^{-0.8} & \quad 90 < R \leq 100 \text{ km} \\
 R^{-0.5} & \quad R > 100 \text{ km}
 \end{aligned} \tag{3.1}$$

Two regional models by Akinçi *et al.* (2006) and Birgoren and Irikura (2005) are tested for the frequency-dependent quality factor. These models underestimate the Fourier amplitude spectra. Thus, a generic model derived based on the world-wide ground motion data is adopted for the quality factor due to the better fit it provided. The crustal shear-wave quality factor  $Q(f) = 88f^{0.9}$  proposed by Boore (1984) is used in the simulations. For the duration model, distance dependent duration model by Herrmann (1985) given in Equation (3.2) is utilized:

$$T = T_0 + 0.05R \tag{3.2}$$

where  $T_0$  is the source duration (equal to the reciprocal of the corner frequency) and  $R$  is the hypocentral distance.

As mentioned in Chapter 2, site response modeling constitutes an important part in stochastic ground motion simulations. Local soil effects are modeled as the multiplication of amplification factors and an exponential function describing the spectral decay at high frequencies. The effect of site response and the general approaches used for the determination of site amplification factors are discussed in Chapter 2. Herein, specific attention is paid to account for site amplification factors in the simulation of Düzce earthquake.

There is no specific information for the site amplification factors or the velocity profile underneath 30 m for the strong ground motion stations considered in this case study. There are site response studies conducted by Kudo *et al.* (2002) for the SKR and DZC stations and by Asten *et al.* (2010) for the DZC and BOL stations. However, in order to assess the site amplification factors at all stations in a uniform manner, H/V technique is utilized at each station.

H/V ratios of the stations are obtained using aftershock and mainshock recordings. Windows having durations of 10 sec. and 5 sec. are selected from the mainshock and aftershock recordings, respectively (Huang and Teng, 1999). These windows mainly bracket the high-amplitude S-wave portions of the records. Figure 3.3 shows the average H/V curves of the strong ground motion stations with a mean curve obtained from all available recordings.

Although in H/V method it is assumed that vertical components of seismic waves are not exposed to local soil amplification, they are as well exposed to near-surface attenuation. When the horizontal component of a seismic wave is divided into the vertical component, near-surface attenuation in the horizontal component is divided into the near-surface attenuation in the vertical component. Thus a term of  $e^{-\pi f(\kappa_{0(\text{horizontal})} - \kappa_{0(\text{vertical})})}$  is already contained in the H/V ratios. In order to employ only the combination of site amplification and the near-surface attenuation of the horizontal component as the site effects filter,  $e^{-\pi f \kappa_{0(\text{vertical})}}$  must be added to the H/V ratio (Motazedian, 2006). Following this observation, in this study vertical  $\kappa_0$  values with H/V ratios are used for a realistic assessment of the local site effects. Thus the combined site response function is expressed as  $H/V \cdot e^{-\pi f \kappa_{0(\text{vertical})}}$ . The regional  $\kappa$  values are calculated for the vertical components of a total of 66 recordings measured at 30 stations of events having moment magnitudes ranging from 5.8 to 7.1. Information on the location, site class, and operator of the stations along with the number of records used at each station are given in Table 3.2.

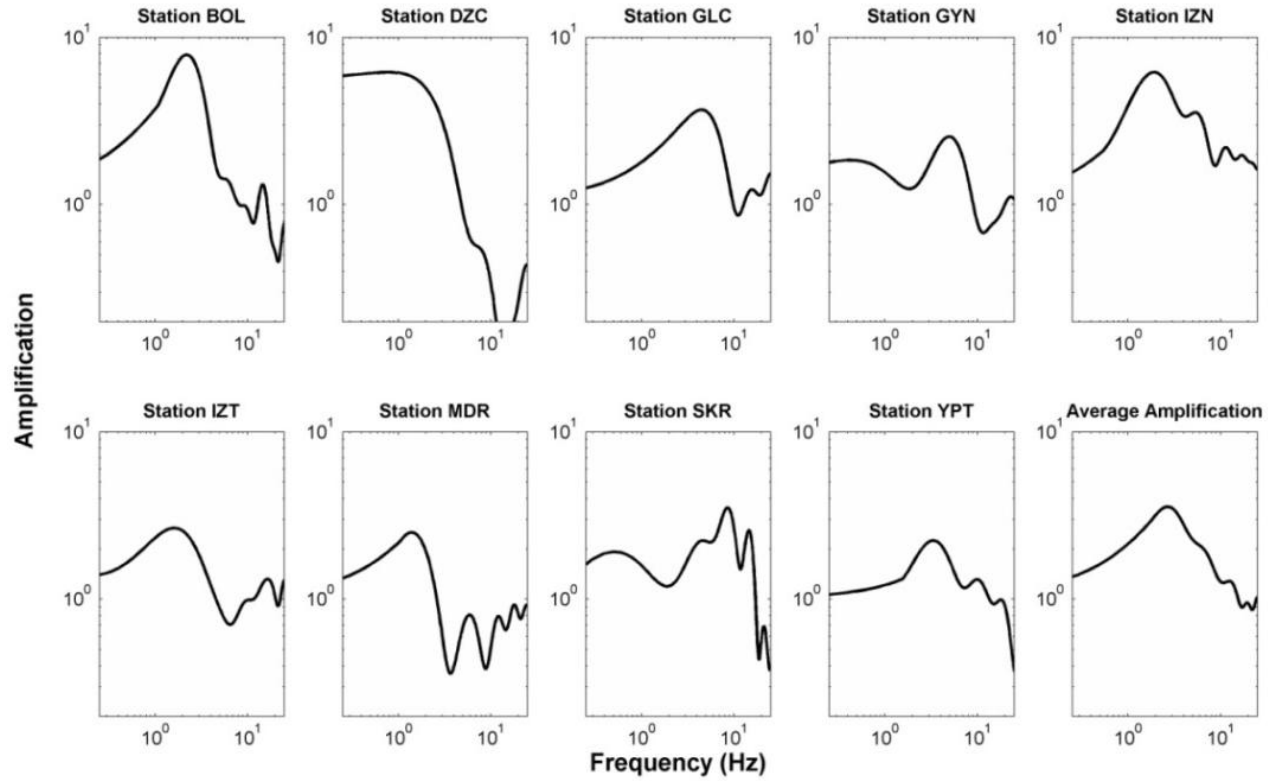


**Figure 3.3** Average H/V ratios of each station based on mainshock and aftershock recordings and the mean H/V ratio of all available records from the 1999 Düzce earthquake

**Table 3.2** Information on the strong motion stations used in the derivation of site specific parameters

Station Name	Station Code	Latitude (°N)	Longitude (°E)	Site Class (NEHRP)	Operator	# of records used
Darica Arcelik Lab.	ARC	40.82	29.36	C	KOERI	3
Ambarli Thermic Power Plant	ATS	40.98	28.69	D	KOERI	4
Yalova Baglaralti Ave.	BAG	40.65	29.27	D	KOERI	1
Yalova Bahcevan St.	BAH	40.65	29.28	D	KOERI	1
Bursa Civil Defence Office	BRS	40.18	29.13	C	ERD	3
Botas Gas Terminal	BTS	40.99	27.98	C	KOERI	2
Bursa Tofas Factory	BUR	40.26	29.07	D	KOERI	4
Canakkale	CNA	41.02	28.76	D	KOERI	4
Darica Arslan Cement Factory	DAR	40.76	29.37	D	KOERI	1
Airport	DHM	40.98	28.82	D	KOERI	3
Fatih Tomb	FAT	41.02	28.95	D	KOERI	4
Galata Bridge	GB	41.02	28.97	D	KOERI	3
Gebze Tubitak Marm. Research Institute	GBZ	40.82	29.44	C	ERD	1
Yalova	GIR	40.66	29.296	D	KOERI	1
Golcuk	GLC	40.73	29.82	D	ITU	1
Goynuk City Hospital	GYN	40.39	30.73	D	ERD	2
Yalova City Hospital	HAS	40.87	29.09	C	KOERI	3
Yalova Hilal St.	HIL	40.65	29.26	D	KOERI	1
Istanbul Min. of Public Works	IST	41.08	29.09	C	ERD	3
Iznik Village Clinic	IZN	40.44	29.75	D	ERD	2
Izmit Weather Station	IZT	40.79	29.96	C	ERD	2
Yalova Ahmet Tas Residence	KAS	40.66	29.29	D	KOERI	1
K.M.Pasa Tomb	KMP	41	28.93	D	KOERI	4
Kütahya Civil Defence Office	KUT	39.42	30	D	ERD	5
Mudurnu District	MDR	40.74	31.21	D	ERD	1
Yalova Ruzgar St	RUZ	40.65	29.28	D	KOERI	1

**Table 3.2 (cont'd)**

Sakarya Min. of Public Works	SKR	40.74	30.38	C	ERD	1
Yalova Agriculture Office	TAR	40.66	29.25	D	KOERI	1
Tekirdağ Min. of Public Works	TKR	40.98	27.52	C	ERD	1
Yarimca Petkim	YPT	40.76	29.76	D	KOERI	2

The  $\kappa$  values of vertical component of ground motion at each station are plotted against epicentral distance (Figure 3.4). The equation of the best-fit line to the distribution is  $0.0474 + 0.00004R$ . Note that this kappa value is in good agreement with the values that have been proposed previously for soft soil sites in Northwestern Turkey which vary between 0.047 and 0.054 (Anderson *et al.*, 2001; Durukal, 2002; Akinci *et al.*, 2006; Ansal *et al.*, 2009).

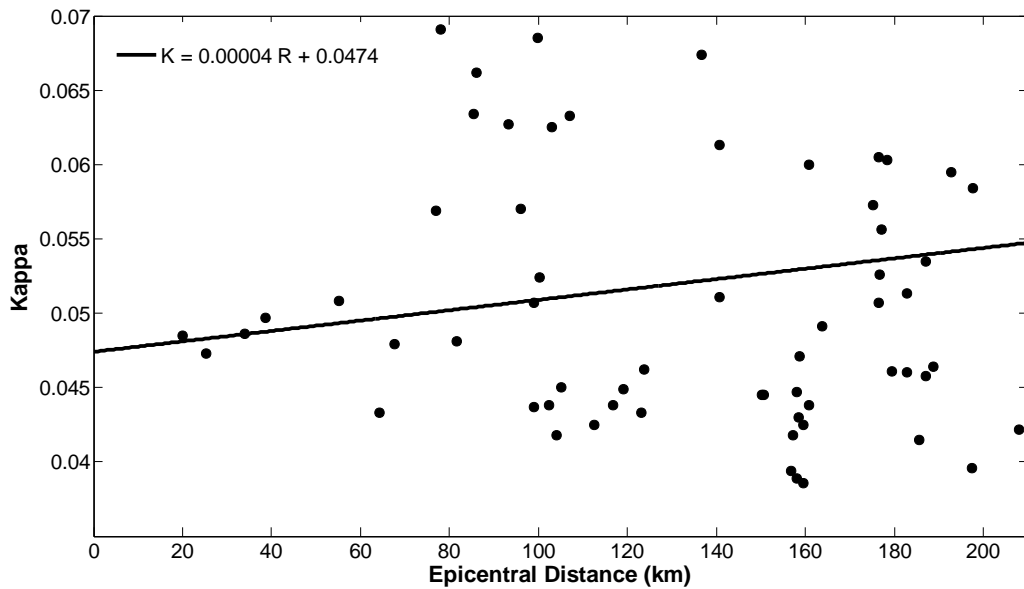


**Figure 3.4** The distribution of vertical kappa factors versus epicentral distance

Figure 3.5 compares the regional average site effects function  $H/V \cdot e^{-\pi f \kappa_0(\text{vertical})}$  computed in this study with those of generic rock and generic soil site conditions defined in Boore and Joyner (1997). It is observed that the regional soil properties lie between the generic rock and generic soil conditions which confirms the varying local soil conditions.

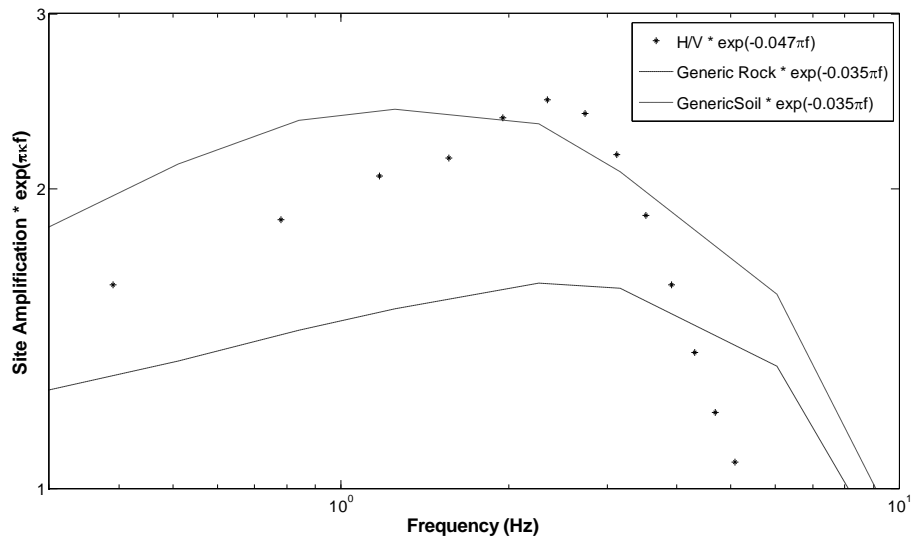


**Figure 3.5** Average of the combined site effect  $H/V \cdot e^{-\pi f \kappa_0(\text{vertical})}$  for the Düzce region in comparison with those of generic rock and soil conditions by Boore and Joyner (1997)

Stress drop is an important parameter which in a way reflects the difference in the stress state before and after the rupture process. Although it is an essential parameter defining the source mechanism, it is not an easily-quantified parameter. Because of the ambiguity associated with its estimation, in this study an error minimization scheme is utilized to determine the stress drop of the 1999 Düzce earthquake. A misfit function is defined which represents the difference between the simulated and

observed Fourier acceleration spectra. The misfit function used in this study is defined as follows (Castro *et al.*, 2008):

$$E(f) = \frac{1}{n} \sum_{i=1}^n \log \left( \frac{A_i(f)_{observed}}{A_i(f)_{synthetic}} \right) \quad (3.3)$$

where  $n$  is the number of stations used in simulations and  $A_i(f)$  is the acceleration spectra of the  $i^{th}$  station. This model misfit function is minimized in the frequency range of 0.25-25 Hz. Figure 3.6 displays the variation of the model error versus frequencies for different stress drop values. Finally, the stress drop parameter for the 1999 Düzce earthquake is calculated to be 100 bars.

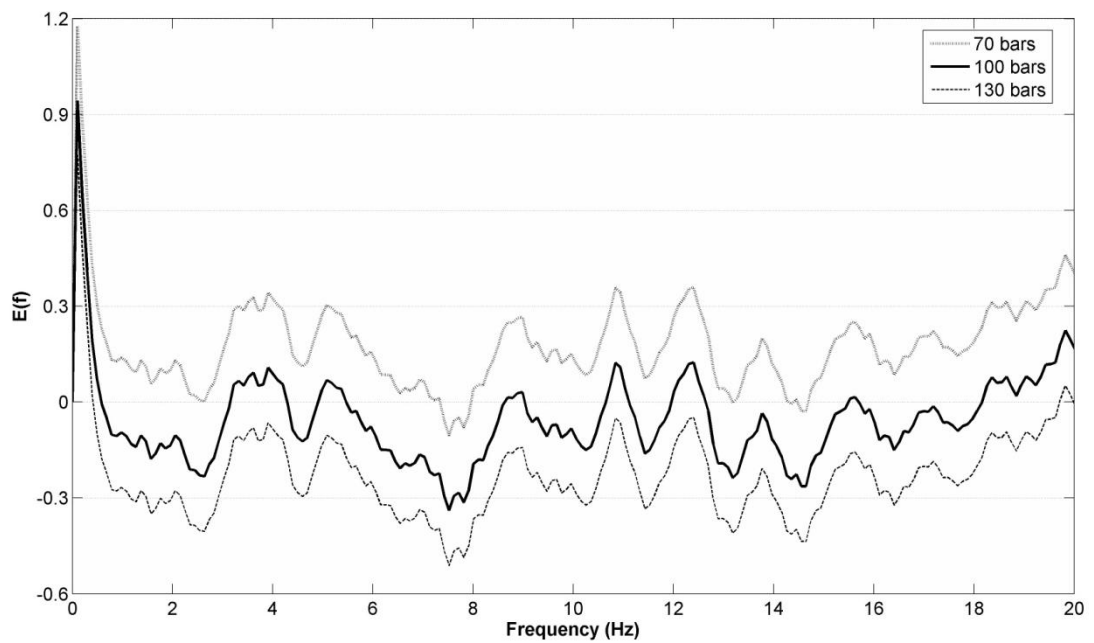


**Figure 3.6** Model misfit versus frequency for various values of stress drop

The pulsing area percentage is another free parameter in EXSIM. The level of low-frequency spectra is controlled by this parameter. Using the misfit function defined in Equation (3.3), pulsing area percentage which better estimates the low-frequency spectra of the nine stations is found to be 30%.

The optimized finite-fault model parameters of the 1999 Düzce earthquake for source, path and site effects are presented in Table 3.3 (Ugurhan and Askan, 2010).

**Table 3.3** Finite-fault model parameters for the 12 November 1999 Düzce earthquake simulation

<b>Parameter</b>	<b>Value</b>
Fault orientation	Strike: 264° Dip: 64°
Fault dimensions	65 x 25 km
Moment Magnitude	7.1
Hypocenter Depth	12.5 km
Subfault Dimensions	5 x 5 km
Stress Drop	100 bars
Crustal Shear Wave Velocity	3700 m/s
Crustal Density	2800 kg/m <sup>3</sup>
Pulsing Area Percentage	30%
$\kappa_0$	0.047
Duration Model	$T_0+0.05R$
Attenuation model, $Q(f)$	$88f^{0.9}$
	$R^{-1}$ $R \leq 30$ km
	$R^{-0.4}$ $30 < R \leq 60$ km
Geometric Spreading	$R^{-0.6}$ $60 < R \leq 90$ km
	$R^{-0.8}$ $90 < R \leq 100$ km
	$R^{-0.5}$ $R < 100$ km
Windowing Function	Saragoni-Hart
Local Amplification	H/V ratios

For BOL station, an  $f_{\max} = 15 \text{ Hz}$  filter is used rather than  $\kappa_0$  to account for the slower spectral decay of the higher frequencies. As pointed out by several authors (eg.: Durukal, 2002; Rathje *et al.*, 2006) located directly to the east of the ruptured fault segment, BOL station has shown a forward rupture directivity effect evidenced by relatively short duration and high amplitude of the ground motion recorded. Based on several previous studies stating the existence of supershear rupture propagation toward the East on the Düzce fault (e.g.: Bouchon *et al.*, 2001; Birgoren *et al.*, 2004; Bouin *et al.*, 2004; Bouchon and Karabulut, 2008; Konca *et al.*, 2010), the slower spectral decay at high frequencies at BOL station can be related to the effect of supershear rupture. In a recent study by Bizzarri and Spudich (2008), it is shown that supershear rupture velocities lead to a net enhancement of high frequency radiation which may be the cause of the increased frequency content of the record at the BOL station compared to the other near-fault stations.

### 3.5 Results of Simulations and Discussions

#### 3.5.1 Comparison of Observed and Simulated Waveforms

The synthetic Fourier amplitude spectra and acceleration time histories, computed using the model parameters given in Table 3.3, are shown along with the recordings in Figure 3.7 at the selected strong ground motion stations. To represent the misfit as a single value, the following definition of error is used for every station:

$$\text{Error}_f = \frac{1}{n_{freq}} \sum_{0.5 \leq f \leq 20 \text{ Hz}} \log \left| \frac{A_i(f)_{\text{observed}}}{A_i(f)_{\text{synthetic}}} \right| \quad (3.4)$$

where  $n_{freq}$  is the number of frequencies used in the simulation.

The errors between the observed and synthetic spectra, calculated using Equation (3.4), are given in Appendix C.

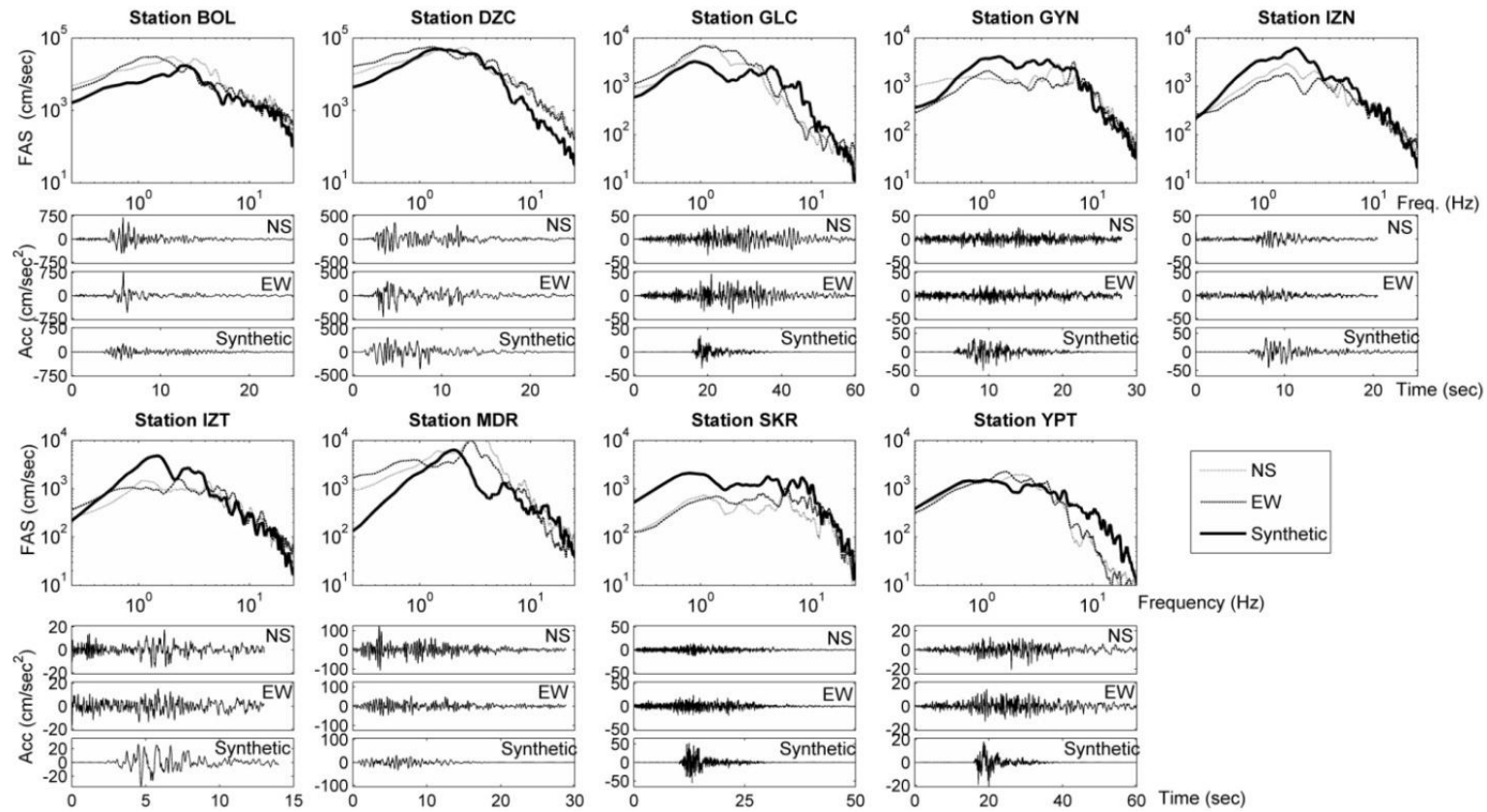


**Figure 3.7** Comparison of time histories and Fourier spectra of synthetics with real data for the 12 November 1999 Düzce earthquake at the selected stations

Through the comparison of acceleration time histories in Figure 3.7, the individual synthetic peak ground acceleration values are observed to generally match well with the observations. The duration of the ground motions is well-reproduced at most of the stations (DZC, BOL, MDR, IZT, IZN) but underestimated at some of the distant stations (GLC, YPT, SKR), pointing out to the significance of regional duration models that include the complexity of the wave propagation path effects. Surface waves generated from basin effects, which are not included in the finite-fault model, can also explain the longer durations of the records when compared with those of synthetics.

Comparing the synthetic and observed Fourier spectra for frequencies less than 1 Hz in Figure 3.7, at the MDR and DZC stations, the synthetic spectrum is observed to be lower than the recorded one. This observed misfit at lower frequencies cannot be completely due to the source model since the same model works well for the other stations. However, in a recent study by Konca *et al.* (2010), it is stated that the waveforms recorded at the near-source stations during the 12 November 1999 Düzce earthquake can be best explained using a variable rupture velocity. Since the finite-fault model used here does not take into account the variations in the rupture velocity, the discrepancy at the lower frequencies at the near fault stations are expected to some extent. On the other hand, this error at lower frequencies might as well rise from homogeneous half space assumption of the model, where the surface waves are not generated in the synthetics.

For the higher frequencies, a sufficient spectral match is observed at BOL, IZN and IZT stations. However, at DZC, GLC, MDR, and YPT stations, the high frequency portion of the simulated spectra overestimates the observed ones. A major cause of these discrepancies could be the insufficient representation of site amplifications since soft soil sites could display strong nonlinearity effects under seismic excitations with high intensity. At the SKR station, despite the close match of the spectral shape, the observed spectra is overestimated by the synthetic one at almost all frequencies. This may be caused by the smaller moment release on the fault towards the west or the backward directivity effects, which cannot entirely be represented by the method

used herein. Note that the longer duration and smaller amplitudes of the SKR record support the possibility of backward directivity phenomenon (Appendix D).

Additionally, none of the strong motion stations that recorded the 1999 Düzce earthquake were located at free-field during the time of the earthquake. Thus, dynamic responses of the buildings containing the accelerometers could as well be included in the recorded data at certain frequencies, which are certainly not possible to regenerate through ground motion simulations.

### **3.5.2 Simulation of Forward Directivity with an Analytical Pulse**

An important feature of the near fault ground motions is the source directivity phenomenon affecting the amplitude, frequency content and the duration of the ground motions recorded in the close vicinity of the fault. Located directly to the east of the ruptured fault segment, BOL station has shown a forward directivity effect evidenced by the short duration and high amplitude of the recorded ground motion. Effect of forward directivity in near-fault ground motions of large earthquakes is generally associated with the seismic radiation pattern towards the fault-normal direction causing a large long period velocity pulse in the fault-normal component. As a result, the fault-normal ground motion is usually larger than the fault-parallel component at longer periods (Somerville *et al.*, 1997). However, in many cases a clear pulse in the fault-parallel component is also observed (Bray and Rodriguez-Marek, 2004; Watson-Lamprey and Boore, 2007) as in the case of BOL station, in particular when supershear rupture propagations are present (Dunham and Archuleta, 2004). From Figure 3.7, despite the discrepancy in the amplitude; the frequency content, duration and spectral shape of the fault-normal (North-South) component are already simulated using only the stochastic high-frequency model application of EXSIM. Consequently, the single pulse shaped motion in the fault-parallel (FP) component of the BOL station is regenerated using the analytical model by Mavroeidis and Papageorgiou (2003) included in EXSIM. Although EXSIM does not assign a directivity effect to individual subfaults, it is known to mimic the directivity

effect by the effects of rupture propagation along the fault (Assatourians and Atkinson, 2007). However, EXSIM did not fully reproduce the velocity pulse at BOL station where forward directivity is highly pronounced. Therefore the analytical approach by Mavroeidis and Papageorgiou (2003) included in EXSIM is used. In this approach, the near-fault pulse is defined in a closed-form expression in time-domain with the following four parameters: pulse period, pulse amplitude, the number and phase of the half cycles. Pulse period is related to the magnitude of the earthquake through  $\log T_p = -2.9 + 0.5M$  and here its value is taken to be 4.47. The amplitude parameter  $A$  is taken to be 100 to regenerate the measured pulse amplitude, the phase angle  $\nu$  is  $180^\circ$  and the parameter  $\gamma$  related to the oscillatory character is taken to be 0.17. In the frequency domain, the pulse generated with this analytical model is superimposed with the random synthetic record generated in EXSIM. Transformation back to time domain results in stochastic time series with a long-period pulse. (Motazedian and Atkinson, 2005). Figure 3.8 displays the observed fault-parallel component at the BOL station, compared in both time and frequency domains with the hybrid random horizontal component.

The pulse is simulated using the analytical model with a particular improvement in the match of spectral amplitudes corresponding to lower frequencies. However, it is important to be able to estimate a directivity pulse in advance rather than regenerating it with models such as the one presented herein. Reliable simulations of forward directivity effects are essential for assessing the seismic response of long-period engineering structures. The limitations of the stochastic finite-fault method for simulating directivity effects without any analytical models will be discussed in detail in Chapter 4.

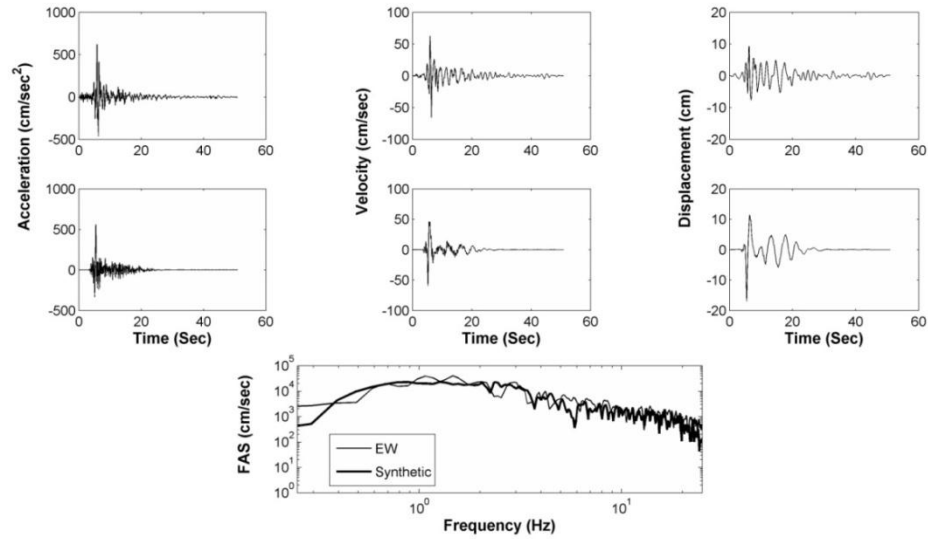


**Figure 3.8** Acceleration, velocity and displacement time histories recorded at the BOL station in comparison with those of the synthetics generated using the analytical directivity model

### 3.5.3 Comparison of Observed Damage with the Distribution of Simulated Ground Motions

The validated model is used to simulate random synthetic horizontal acceleration records around the fault to observe whether any correlation between the observed building damage and the spatial variation of simulated peak ground motion parameters exists. A region of 2° (East-West) by 1° (North-South) is picked around the fault and divided into grids of 0.02°. At each grid point synthetics are generated. The objective is to observe the combined effects of the source and soil conditions on the spatial distribution of the ground motion in the region and to detect possible correlation between the observed building damage and the peak ground motion parameters. Typical soil property within the Düzce and Bolu basins is deep alluvial deposits. For simplicity, the region encountered is assumed to be underlain uniformly

by deep soil deposits. To represent the mean soil conditions, the average H/V ratio and kappa factor of 0.047 both derived in this study is used.

As a measure of the severity of the widespread building damage in the near-fault area, a mean damage ratio (MDR) is defined for each subprovince in the region based on damage surveys performed on reinforced concrete and masonry residential buildings in cities of Düzce, Sakarya and Bolu in the aftermath of the 12 November 1999 Düzce earthquake (Özmen and Bağcı, 2000). In these damage surveys, each residential building is classified into one of the following damage levels: None (N), Light (L), Moderate (M), Severe (S) damage cases and Collapse (C) case. Each of these damage levels is assigned a central damage ratio as a function of the ratio of the replacement cost of the building to the original cost of construction (Gurpinar *et al.*, 1978; Yucemen and Askan, 2003) as shown in Table 3.4.

**Table 3.4** Central damage ratios for the damage levels

<b>Damage Level</b>	<b>Definition</b>	<b>Central Damage Ratio (%)</b>
N	None Damage	0
L	Light Damage	5
M	Moderate Damage	30
S	Severe Damage	70
C	Collapse	100

Mean damage ratio in a region is then calculated as a weighted average of the occurrence rates of each damage level, with the central damage ratios as weights. In

other words, for a region with no building damage the MDR is 0% and in a region where all the buildings have collapsed the MDR is 100%.

In Figure 3.9, the spatial distribution of ground motion is compared with that of building damage. The thin lines are the subprovince borders whereas the thick lines are city borders. The triangles are the stations that recorded the mainshock. The epicenter of the 12 November 1999 Düzce earthquake is shown with a star sign. Figure 3.9a is a contour map showing the distribution of synthetic PGA within the region and Figure 3.9b demonstrates the distribution of mean damage ratios of residential buildings that were exposed to the ground shaking at the subprovince level in cities of Bolu, Düzce and Sakarya. Figure 3.9b displays the unique discrete MDR value computed for each subprovince.

From Figure 3.9a, despite the average soil amplifications employed, the PGA values are as high as 0.4g and 0.7g around the Düzce city center and Kaynaşlı region, respectively. Consistent with the PGA distribution, these locations have very high MDR values up to 40% as seen in Figure 3.9b. On the other hand, the city centers of Bolu and Sakarya exhibit relatively lower PGA values around 0.2g but the subprovinces located to the east of Sakarya have much higher PGA values consistent with the damage distribution in that area. The overall PGA distribution compares well with the MDR distribution in the region, yet high MDR values despite lower PGA values in the city centers of Bolu and Sakarya indicate that the major structural damage observed in these areas may be attributed to major local site effects which are not taken into account herein. Finally, as observed from Figures 3.9a and 3.9b, in Karadere region of Sakarya, despite the high PGA values, very low MDRs are observed. This is due to the fact that Karadere is a mountainous rural area.

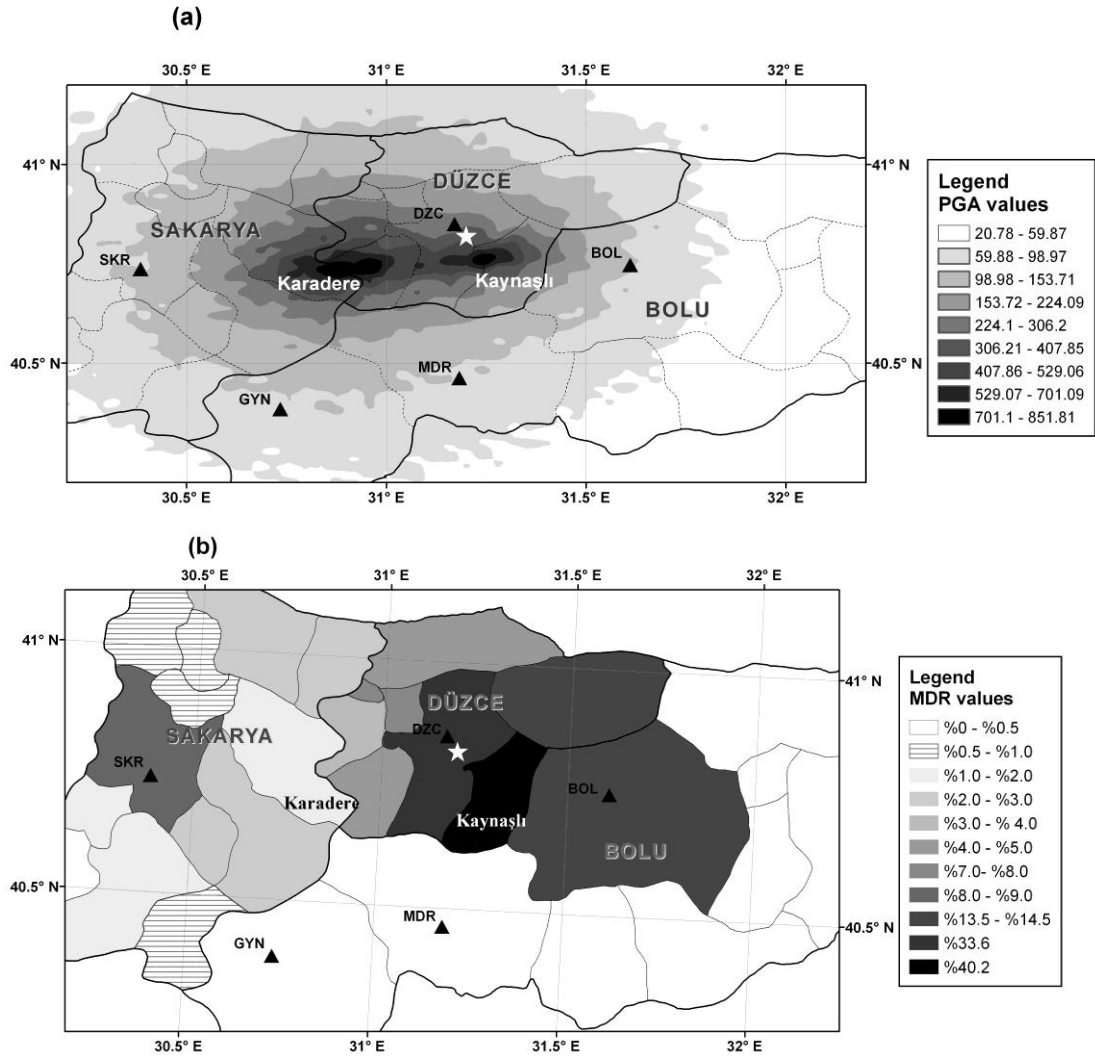


**Figure 3.9** Distribution of (a) synthetic PGA map (in  $\text{cm/sec}^2$ ) and (b) and mean damage ratios

The spatial variation of peak ground motion parameters in Figure 3.9 reflects mainly the source effect since the soil conditions are assumed to be uniform in the region. The peak amplitudes display the effect of soil conditions but they as well include an inherent uncertainty related to mean soil condition assumption made in the simulation of the synthetic records. The widespread building damage observed in the meizoseismal area can be said to have occurred as a combination of the source and site effects. However, a more rigorous comparison of the distributions of peak

ground motion parameters and building damage must involve more precise representation of the local site effects. Further studies in this direction could yield very insightful results in terms of correlation of local site amplifications with observed building damage.

#### **3.5.4 Comparison of Attenuation of Synthetics with GMPEs**

To compare the simulated results with recent ground motion prediction equations derived based on the strong ground motion data of the region and two recent NGA models; synthetic records are generated for 2600 dummy stations for two different site conditions: generic rock and mean soil conditions. For the regional mean soil conditions, the mean H/V ratio derived in this study is used with a regional kappa factor of 0.047; and for the generic rock conditions the generic rock amplifications factors (Boore and Joyner, 1997) is used with a kappa factor of 0.035. Figure 3.10 compares the simulation results with regional GMPEs of Gülkan and Kalkan (2002), Ulusay *et al.* (2004), Akkar and Bommer (2007) and NGA models of Boore and Atkinson (2007) and Campbell and Bozorgnia (2007) for soil and generic rock conditions.

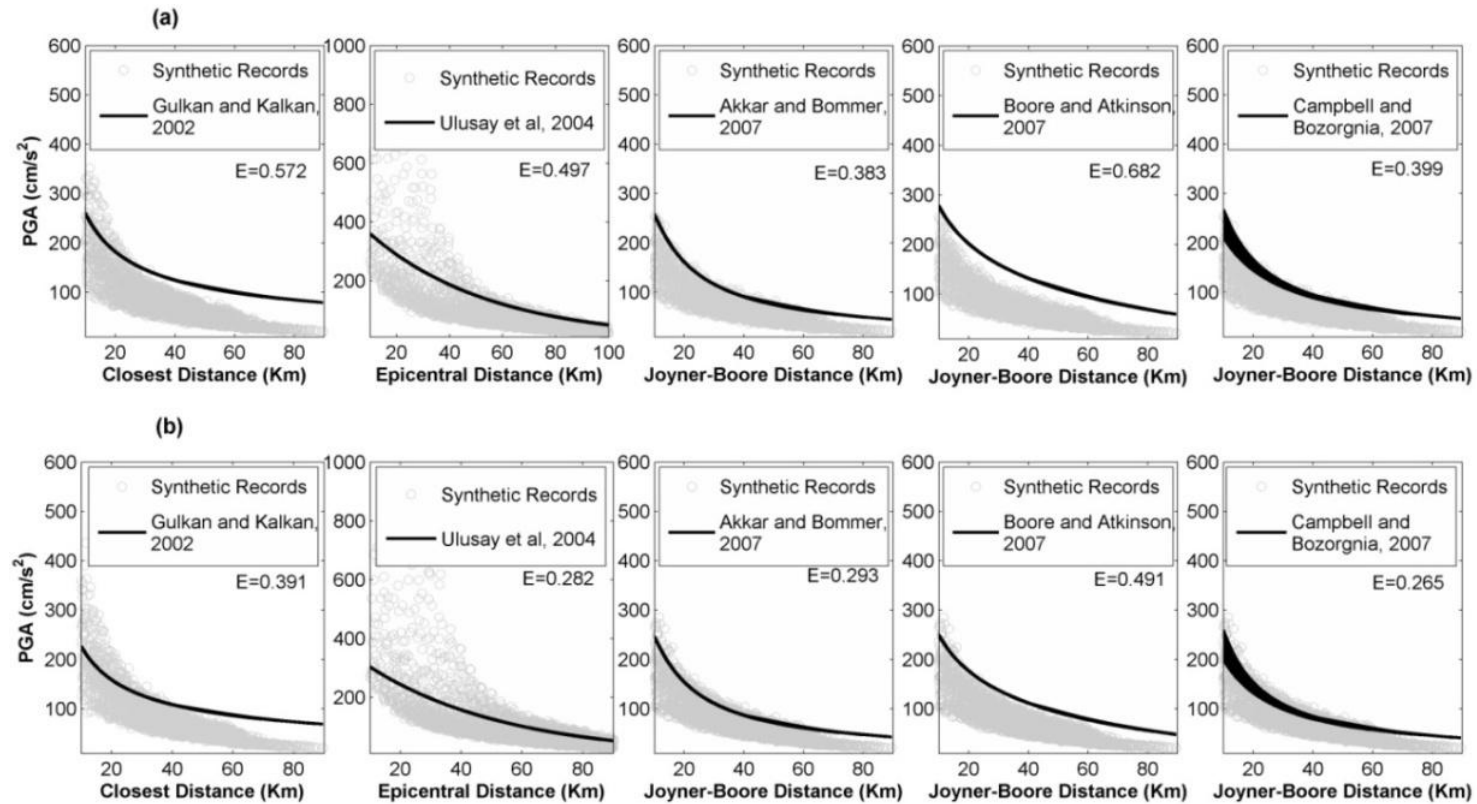


**Figure 3.10** Comparison of attenuation of synthetic data with recent attenuation relationships derived for the region for  
 (a) regional mean soil conditions, (b) generic rock conditions

At the time the studies of Gülkan and Kalkan (2002) and Ulusay *et al.* (2004) were conducted, detailed site descriptions and shear wave velocity measurements were not available at most of the strong motion stations in Turkey. Thus following the existing geological references and past earthquake reports, Gülkan and Kalkan (2002) and Ulusay *et al.* (2004) divided the site conditions into three groups: rock, soil and soft soil. The GMPE derived in the former study uses 30 meters-shear wave velocity ( $V_{S30}$ ) as an input whereas the latter one requires the soil type in terms of the three categories defined. Akkar and Bommer (2007) however provides the GMPE as a function of not only soil types but also faulting styles. Similarly, GMPEs by Boore and Atkinson (2007) and Campbell and Bozorgnia (2007) uses  $V_{S30}$  and faulting type as main input parameters. As shown in the Figure 3.10, different prediction relationships use different distance measures.

For assessing the goodness of fit, the error, E, is calculated as the average ratio of the logarithm of the PGA values determined from GMPEs to the logarithm of the synthetic PGA values at each distance. The errors are shown at the top right corner of each subfigure in Figure 3.10. For generic rock conditions, among all relationships, the GMPE by Campbell and Bozorgnia (2007) exhibits the minimum error. For mean soil conditions, however, a clear discrepancy between most of the GMPEs and synthetics is observed. This misfit could arise from the difference in the site class definition for 'soil' conditions in the prediction equations and the synthetic simulations with mean soil conditions assumed for the region. GMPEs by Boore and Atkinson (2007) and Akkar and Bommer (2007) provide an upper bound to the simulated records for both soil and rock conditions. These two GMPEs are in good agreement between the maximum synthetic PGA values corresponding to each distance.

Comparisons of the synthetics with both observed damage and GMPEs confirm that the simulations are in good agreement with the observations of the 1999 Düzce earthquake.

The next chapter discusses the application of the methodology to L'Aquila region. The limitations of the method in terms of simulating the directivity effects are assessed in detail.

## CHAPTER 4

### GROUND MOTION SIMULATION OF THE 2009 L'AQUILA EARTHQUAKE: SIMULATING DIRECTIVITY EFFECTS

#### 4.1 General

Stochastic ground motion modeling provides physics-based simulations and it is known to successfully predict the amplitudes and frequency content of observed ground motions. Although it has been validated in many parts of the world with earthquakes of various magnitudes, the method has several limitations. The purpose of this case study is to investigate the limitations of this method in terms of simulating directivity effects. For this purpose, an earthquake that is distinguished with significant forward and backward directivity effects is selected. April 06, 2009 L'Aquila (Italy) Earthquake ( $M_w=6.3$ ) is characterized with azimuth-dependent peak ground motion intensity values and durations of the seismograms recorded during the earthquake. The stations that are oriented in the backward direction of rupture propagation recorded low peak values with long durations whereas the stations located in the forward direction of the rupture propagation recorded higher peak values with shorter durations. Figure 4.1 shows sample acceleration-time histories recorded at four selected strong ground motion stations. Stations LSS and SPC are oriented opposite to the rupture direction whereas stations CLN and SUL are oriented along the rupture directions. Furthermore, station pairs of LSS - CLN and SPC - SUL have similar epicentral distances. Backward stations have longer duration, low-amplitude records whereas forward stations have records that have shorter durations but high amplitudes. This obvious signature in the seismograms is attributed to directivity effects. In this chapter, ground motion simulation methodology will be examined in terms of simulating directivity effects.

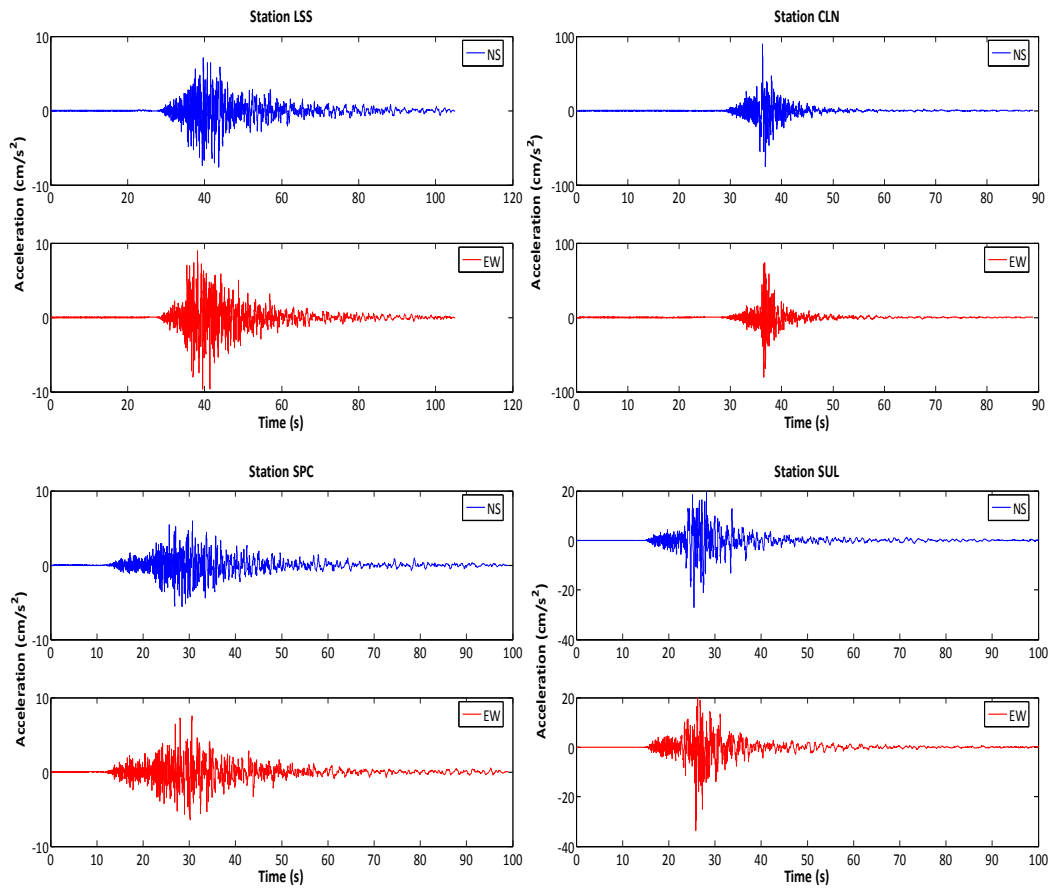


**Figure 4.1** Acceleration records from the 2009 L'Aquila earthquake evidencing directivity effects. The strong ground motion station data is taken from the ITACA WEB site (Italian Accelerometric Archive <http://itaca.mi.ingv.it/ItacaNet>).

In section 4.2, background information about the seismicity and geology of the region with a detailed description of the earthquake are presented. Section 4.3 gives information about the strong ground motion stations. Simulation parameters and validation of these parameters are presented in Section 4.4. Section 4.5 displays the simulation results and summarizes this chapter with discussions.

## 4.2 Background Information

An earthquake of  $M_w=6.3$  occurred in the Central Apennines, Italy, close to the L'Aquila town on April 06, 2009 at 03:33 a.m. with local time. The earthquake occurred on Northwest-Southeast (NW-SE) trending normal fault, with strike, dip and rake angles of  $133^\circ$ ,  $54^\circ$ ,  $-102^\circ$ , respectively (Cirella *et al.*, 2009). The epicenter of the earthquake was located at  $42.423^\circ\text{N}$ ,  $13.395^\circ\text{E}$  with a hypocentral depth of 9 km as reported by Institute of Geophysics and Volcanology (INGV) in Italy.

The foreshock sequence of the L'Aquila earthquake had begun in December 2008. The foreshock activity was considered to be weak until ten days prior to the mainshock. On March 30, 2009 the largest foreshock occurred with  $M_L=4.1$ . During the last ten days before the mainshock, the seismicity rate of the region increased dramatically (Papadopoulos *et al.*, 2010). But none of the events was considered to be a warning for a large magnitude event. Following the  $M_w=6.3$  mainshock event, occurred a significant amount of aftershocks migrating to SE and NW. In one month, hundred aftershocks were recorded with  $3 < M_w < 5$  and several thousand with smaller magnitudes (Akinici *et al.*, 2010). The two largest aftershocks were  $M_w=5.6$  and  $M_w=5.4$  which occurred on April 07, 2009 and April 09, 2009, respectively. The location of the event on the Italy map is shown in Figure 4.2, in bottom left panel. In Figure 4.2, the aftershock distribution is shown with red circles. The yellow star indicates the epicenter of the mainshock whereas the green stars indicate the epicenters of the two largest aftershocks mentioned previously. The white rectangle shows the surface projection of the fault plane. Several of the strong ground motion stations that recorded the mainshock are indicated with blue triangles in the same figure.

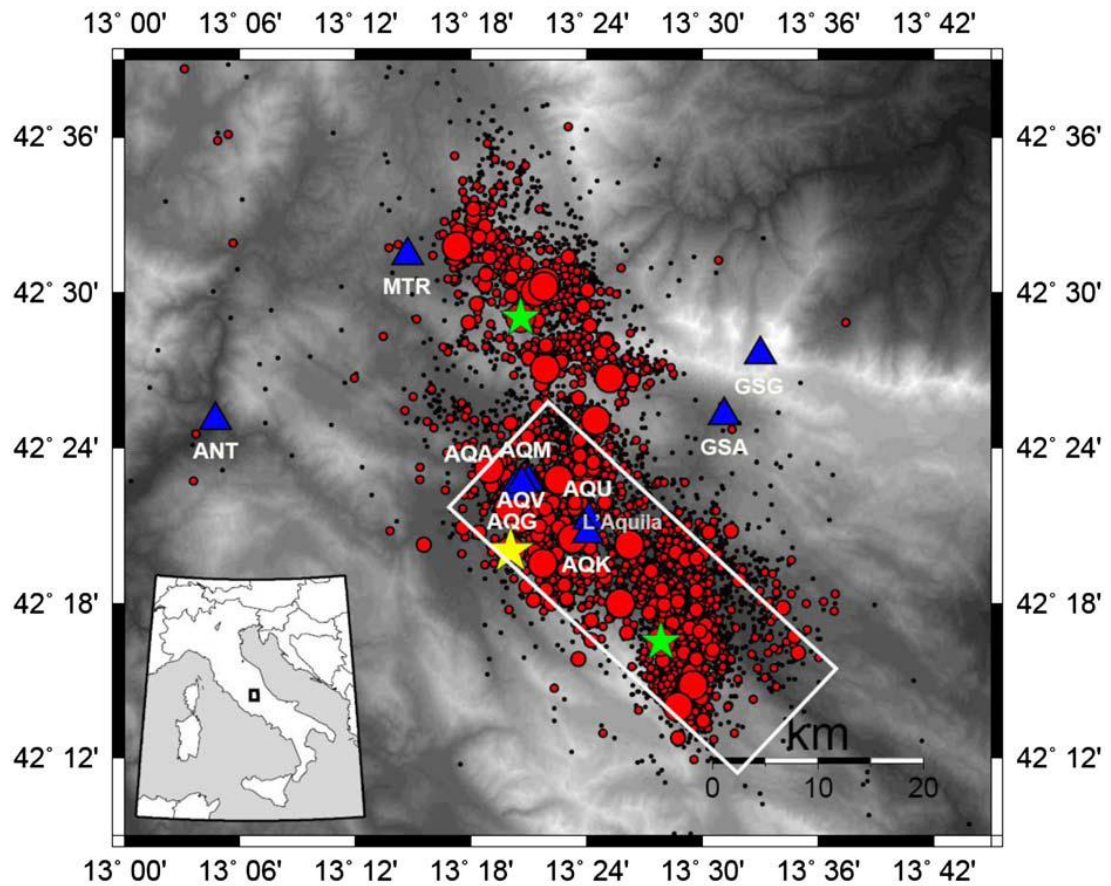


**Figure 4.2** The aftershock distribution in the L'Aquila region and the epicenter of the mainshock of April 1999 L'Aquila earthquake (Adapted from Akinci *et al.*, 2010)

Although the earthquake is considered to be a moderate magnitude event, significant damage is observed. L'Aquila region is one of the most popularized residential regions of central Italy with many historical monuments. The earthquake hit the region at midnight leading to 305 fatalities and thousands of injuries. Significant damage was observed in over 10,000 buildings and approximately 66,000 people were left homeless (Akinci *et al.*, 2010). Many historical buildings and churches were subjected to significant damage as well.

The earthquake region is a part of Aterno valley and characterized by its complex tectonics. The collision of the African and Eurasian plates overcomes the opening of the Tyrrhenian Sea. This movement created many active normal faults in that area. Besides several events with lower intensities (VII-VIII Mercalli-Cancani-Sieberg scale, MCS), the region experienced three significant earthquakes in 1349, 1461, and 1703 (XI-X MCS) in the past 1000 years evidenced by paleoseismological data (De Luca *et al.*, 2005). The complex tectonics caused variable geologic formations within the region. Aterno valley is basically located on Quaternary lacustrine basin. The sediment thickness within the basin varies between 60 m and 250 m (Bindi *et al.*, 2009). Finally, the region is characterized by high level of seismic hazard. Thus, studies assessing potential ground motions in the region are essential.

### **4.3 Strong Ground Motion Data**

The L'Aquila mainshock and aftershocks yielded 264 recordings at 56 strong ground motion stations. These stations belong to Italian Strong Motion Network managed by Department of Civil Protection. The strong ground motion station data used in this study are taken from the ITACA WEB site (Italian Accelerometric Archive <http://itaca.mi.ingv.it/ItacaNet>). All of the accelerograms are digital instruments (Kinematics Episensor FBA-3 200 Hz with ETNA 18 bits or K2-Makalu 24 bits digitizers).

In this study, 21 strong ground motion stations within an epicentral distance of 100 km is selected as the simulation sites. Table 4.1 displays the names of the stations used in this study along with their codes, site classes according to EuroCode 2008 (EC08), epicentral and Joyner-Boore distances with respect to fault plane of the 2009 L'Aquila mainshock as well as PGA and PGV values recorded during the earthquake. The orientation of the epicenter of the mainshock (red star), fault plane (red box) and strong ground motion stations (blue triangles) with respect to the fault plane are indicated in Figure 4.3.

**Table 4.1** Information on the strong motion stations that recorded the 2009 L'Aquila earthquake

Station Code	Station Name	Site Class (EC08)	R <sub>epi</sub> (km)	R <sub>JB</sub> (km)	PGA (cm/s <sup>2</sup> )	PGV (cm/s)
ANT	Antrodoco	A	23.0	17.77	25.97	2.47
AQA	V. Aterno-f. Ateno	B	4.6	0	435.39	31.92
AQG	V. Aterno-Colle Grilli	A	4.4	0	479.3	35.76
AQK	Aquila parcheggio	B	5.7	0	355.46	35.80
AQV	V. Aterno-Centro Valle	B	4.9	0	644.25	42.72
ASS	Assisi	A	101.7	95.27	6.05	0.44
AVZ	Avezzano	C	34.89	20.03	67.69	11.30
CDS	Castel Di Sangro	A	88.52	65.55	9.95	0.98
CHT	Chieti	B	67.17	45.58	29.43	7.87
CLN	Celano	A	31.64	11.69	88.47	7.05
FMG	Famignano	A	19.32	17.07	26.32	2.58
GSA	Gran Sasso	A	18.05	7.86	146.62	9.79
GSG	Gran Sasso (Lab. Infn Galleria)	A	22.63	12.77	29.40	3.15
LSS	Leonessa	A	39.02	33.68	9.61	0.83
MMP	Mompeo	A	49.21	45.56	8.83	0.87
MTR	Monte reale	A	22.35	14.48	61.37	3.54
ORC	Ortucchio	A	49.35	27.79	64.08	5.87
SBC	Subiaco	A	50.42	46.31	6.65	1.25
SPC	Spoletto (Cantina)	C	66.73	61.44	7.56	0.69
SPO	Spoletto	A	65.93	60.70	9.58	0.82
SUL	Sulmona	A	56.53	32.23	33.61	3.65

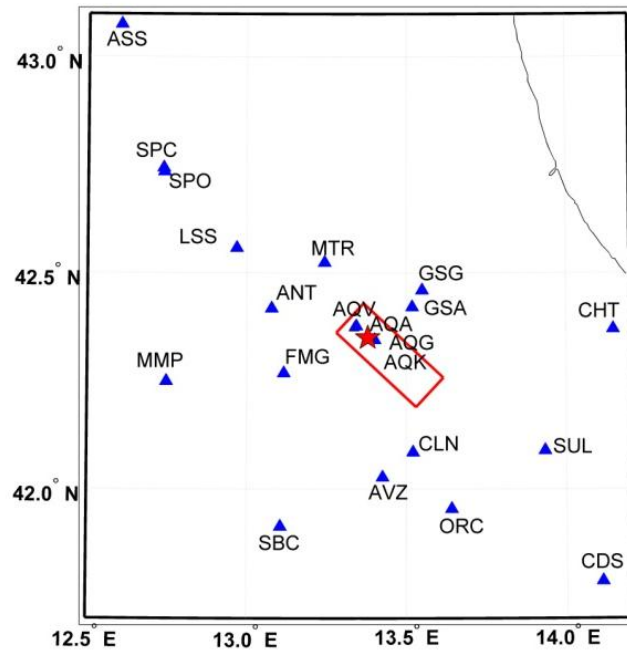


**Figure 4.3** Distribution of the strong ground motion stations that recorded the mainshock of the 2009 L'Aquila earthquake

#### 4.4 Validation of Simulation Parameters

The main objective of this case study is to reproduce the directivity effects in L'Aquila earthquake and investigate the limitations of stochastic finite-fault simulations in generating directivity effects. The amplitudes of ground motions of large earthquakes are significantly azimuth-dependent and are observed to be more sensitive in the direction of rupture propagation (Boore and Joyner, 1978). Since directivity is a rupturing effect and it is mainly due to the source properties, special attention is paid to the parameters that define the source model.

The general procedure followed in this case study is as follows: initially, the path and site effects are constrained to the optimum models proposed in the literature for the Central Italy region. Afterwards, different source models are tested and their effects

are examined. The parameters that define the source mechanism the best are selected. The results of the simulations are then presented with the established parameters.

There are various models in the literature that define the path effects in the Central Italy region (Rovelli *et al.*, 1988; Malagnini *et al.*, 2000; Malagnini *et al.*, 2008; Bindi *et al.*, 2009). Among all models for crustal quality factor and geometrical spreading, the parameters of Malagnini *et al.* (2008), which are based on analyses of weak motion data from the Central Apennines region, are utilized.

A major disadvantage is that none of the strong ground motion stations that recorded the L'Aquila earthquake have detailed site investigations. Site amplification factors determined using Standard Spectral Ratio (SSR) method are given in Akinci *et al.* (2010). These values can be used as site amplifications in the simulations but there are some unrealistic amplification values at certain stations which cannot be considered physically meaningful. For example, at ORC station an amplification factor of 40 and at both AQK and AQV stations an amplification factor of 20 exists. These values suggest that a portion of the source effect might still be present in the site amplification factors (Akinci A. and Malagnini L., personnel comm., 2010). Consequently, generic site amplification factors based on quarter wavelength approach by Boore and Joyner (1997) are utilized. The site classifications of the strong ground motion stations according to EuroCode 2008 (EC08) are given in Table 4.1. Based on the site class information, corresponding soil amplification factors by Boore and Joyner (1997) are employed. For station GSG, which is located 1.5 km below the free surface, no site amplification is used. The stations AQA, AQK, AQV and CHT are identified as site class B according to EC08 classification. For these stations, NEHRP-C type amplification factors by Boore and Joyner (1997) are utilized. The generic soil amplification factors are used for stations AVZ and SPC, which are identified as site class C according to EC08. Other stations are located on type A soils and generic rock amplification factors of Boore and Joyner (1997) are utilized. For modeling the spectral decay at high frequencies,  $\kappa_0=0.035$  is used at all stations (Malagnini *et al.*, 2008).

After the parameters defining path and site effects are constrained, source parameters are assessed in detail. The fault plane is defined with the dip and strike angles which are restricted by the focal plane solutions (INGV) along with its dimensions.

A very significant source parameter is the distribution of slip values along the plane. The asperity locations and relative slip ratios of subfaults directly affect the distribution of peak ground motion parameters. For this purpose, slip distribution models obtained from various source inversions are tested. The first model belongs to Cirella *et al.* (2009) where the rupture history is obtained from the non-linear joint inversion of strong ground motion and GPS data. Two models of Tinti E. (personnel comm., 2010) constitute the second and third models which are obtained from the inversion of strong ground motion and GPS data together and strong ground motion data alone, respectively. The dimensions of the fault plane vary in these studies. Figure 4.4 shows the three alternative fault models with the associated slip distributions defining the source (The slip values given in the figure are in meters whereas the fault lengths and widths are given in km). As observed, models have asperities at different locations. In the first model by Cirella *et al.* (2009), a big asperity exists in the bottom center. In both second and third models, there are two asperities at different locations.

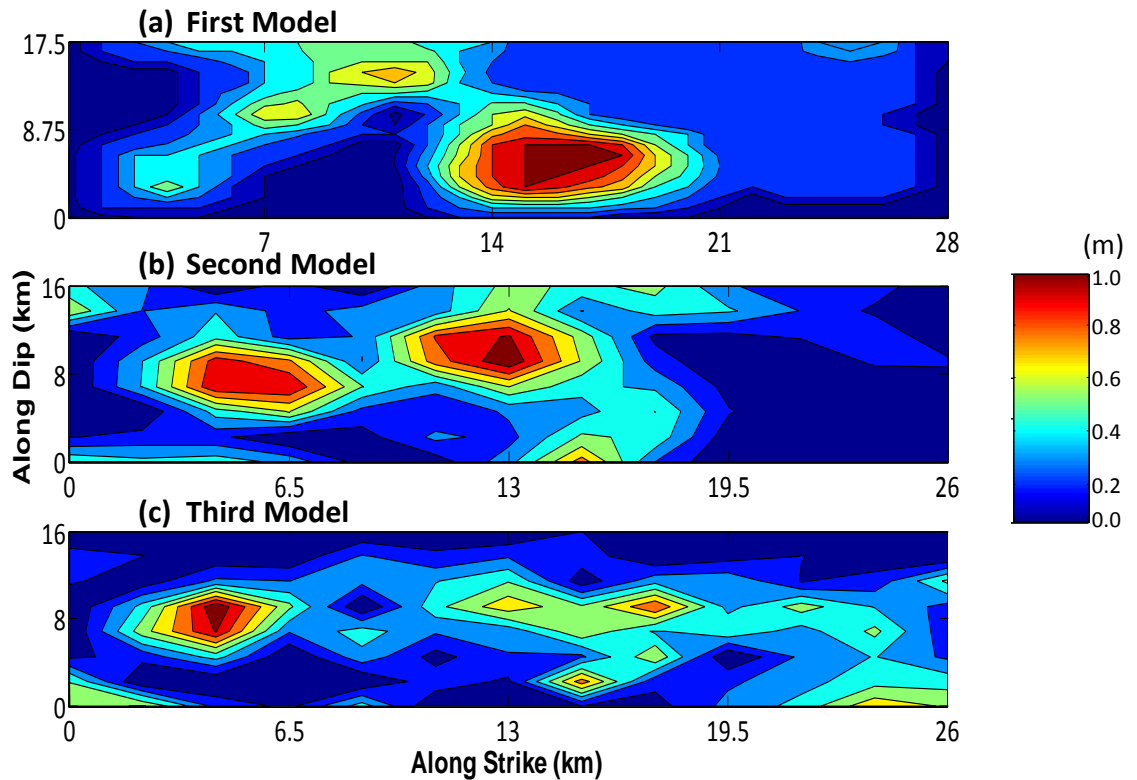


**Figure 4.4** Slip distribution models proposed for 2009 L'Aquila earthquake

As mentioned previously, stress drop is the signature of the rupture mechanism and it defines the amplitudes of the Fourier spectra. Different stress drop values are tested here in an error minimization scheme. The aim is to minimize the total error between the observed and synthetic records in the frequency domain. It is observed that the stress drop value, which provides a close fit to the stations that are oriented along the rupture direction, overestimates the Fourier amplitudes of the stations that are oriented in the opposite direction. The opposite holds true for the stations that are oriented in the backward direction. With a lower stress drop value, a better fit is observed at backward stations but the spectral values of forward stations are underestimated. We can group the stations ANT, ASS, FMG, LSS, MMP, MTR, SBC, SPC and SPO as backward stations and the rest (stations AQA, AQG, AQK, AQV, AVZ, CDS, CHT, CLN, GSA, GSG, ORC and SUL) as forward stations.

Since there is approximately equal number of stations along and opposite to the rupture direction, the stress drop value minimizing the total error does not serve the purpose. Since in a recent paper, Akinici *et al.* (2010) pointed to the high stress drop value associated with the rupture complexity of the earthquake, the stress drop value providing good fit at sites oriented along forward directivity is chosen, which is 150 bars.

The peak ground motion intensity parameter distributions with different slip models are shown in Figure 4.5. Different slip models are observed to affect only the peak values at the points near the fault plane. Peak values are observed to occur on the surface projection of asperities and the top of the rupture plane. However, at intermediate to far distances, different slip models make almost no difference in the distribution of the peak values. At these distances, peak ground motion intensities are governed by path and site effects mostly.

Due to the better fit obtained in the low frequency band of the Fourier amplitude spectra of the records, the model by Cirella *et al.* (2009) is selected as the fault plane solution of the 2009 L'Aquila earthquake. The proposed fault plane has dimensions of 28 x 17.5 km and it is divided into subfaults of 1x1 km. The top of the rupture plane is at a depth of 0.5 km.

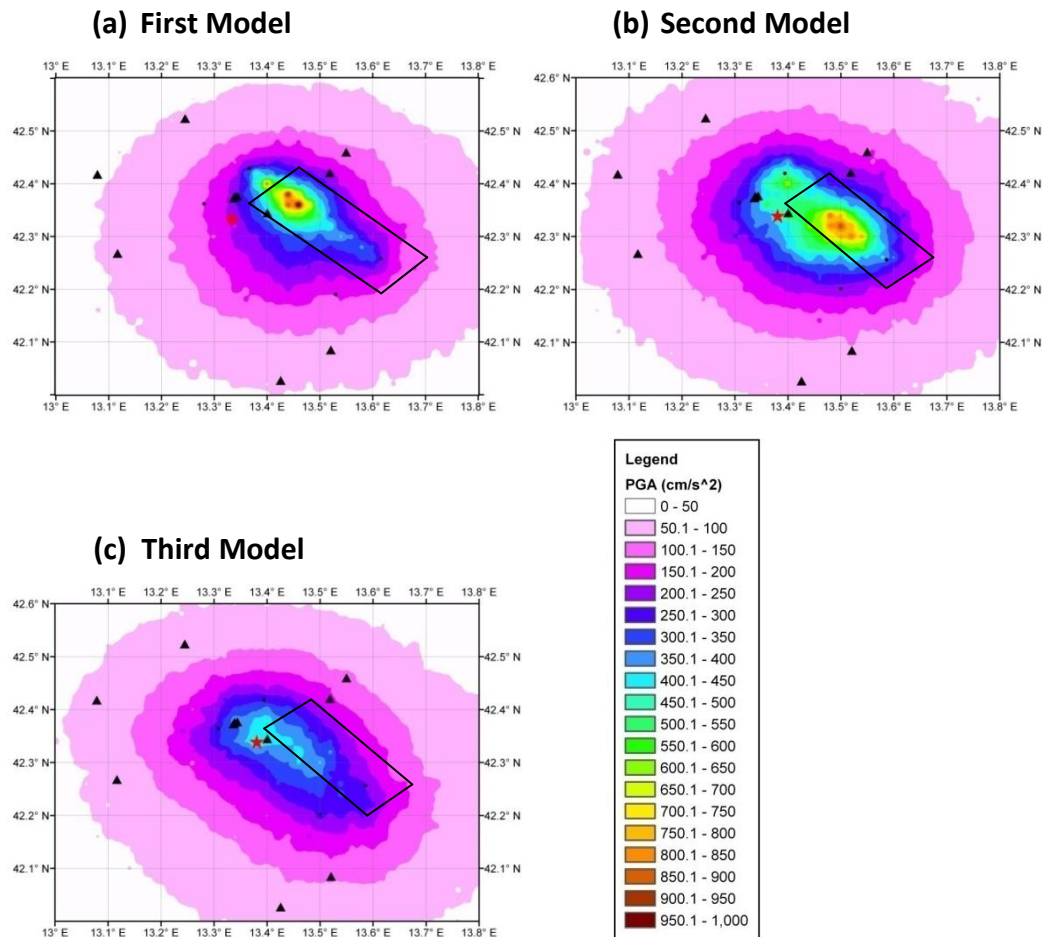


**Figure 4.5** Distribution of PGA values for different slip models of 2009 L'Aquila earthquake

Table 4.2 summarizes the simulation parameters which are used to define the 2009 L'Aquila Earthquake model.

**Table 4.2** Finite-fault model parameters for the 2009 L'Aquila earthquake simulation

<b>Parameter</b>	<b>Value</b>
Fault orientation	Strike: 133° Dip: 54°
Fault dimensions	28 x 17.5 km
Moment Magnitude	6.3
Depth of the Top of Fault Plane	0.5km
Subfault Dimensions	1 x1 km
Stress Drop	150 bars
Crustal Shear Wave Velocity	3500 m/s
Crustal Density	2800 kg/m <sup>3</sup>
Pulsing Area Percentage	50%
$\kappa_0$	0.035
Duration Model	0.1606*R for $0 \leq R < 40$ 0.10673*R for $40 \leq R < 80$ 0.005*R for $R \geq 80$
Attenuation model, Q(f)	$100f^{0.4}$
Geometric Spreading	$R^{-1}$ if $R < 30$ km $R^{-0.5}$ if $R \geq 30$ km
Windowing Function	Saragoni-Hart
Local Amplification	Boore and Joyner, 1997

#### 4.5 Results of the Simulations and Discussions

The Fourier Amplitude spectra of the strong ground motion records in comparison with the synthetics are given in Figures 4.6 and 4.7. The errors between the simulated and observed spectra are calculated using Equation (3.4). These errors are presented in a tabular format in Appendix C.

The spectra of strong ground motion stations that are oriented in the forward direction are shown in Figure 4.6. As observed from the figures, simulations provided reasonable estimates of the general shape and amplitudes of the spectra. At stations AQA and AQV, the simulations do not capture several local peaks which are most probably due to local site amplification effects. These stations have site classes of type B according to EC08 and using generic amplification factors in the simulations; the effect of local soil conditions is only mimicked. Although the amplitudes are roughly captured, the amplifications at some important frequencies cannot be simulated. This observation holds true for station AVZ as well. AVZ has site class of C and generic site amplifications and diminution factor are most probably not capable of identifying local site effects at that station. Better assessment of site conditions could improve the fit for these stations.

The Fourier Amplitude spectra of the records at the strong ground motion stations that are oriented in the backward direction are shown in Figure 4.7. As observed from the figures, the synthetic spectra overestimate the observed spectra of both horizontal components especially in the low frequency band. Since only the station SPC is located on site class C type soil, this overestimation in all other stations cannot be due to soil effects. This discrepancy should be due to the directivity effects, in this case backward directivity effects, which cannot be simulated using stochastic finite-fault methodology implemented in this study.

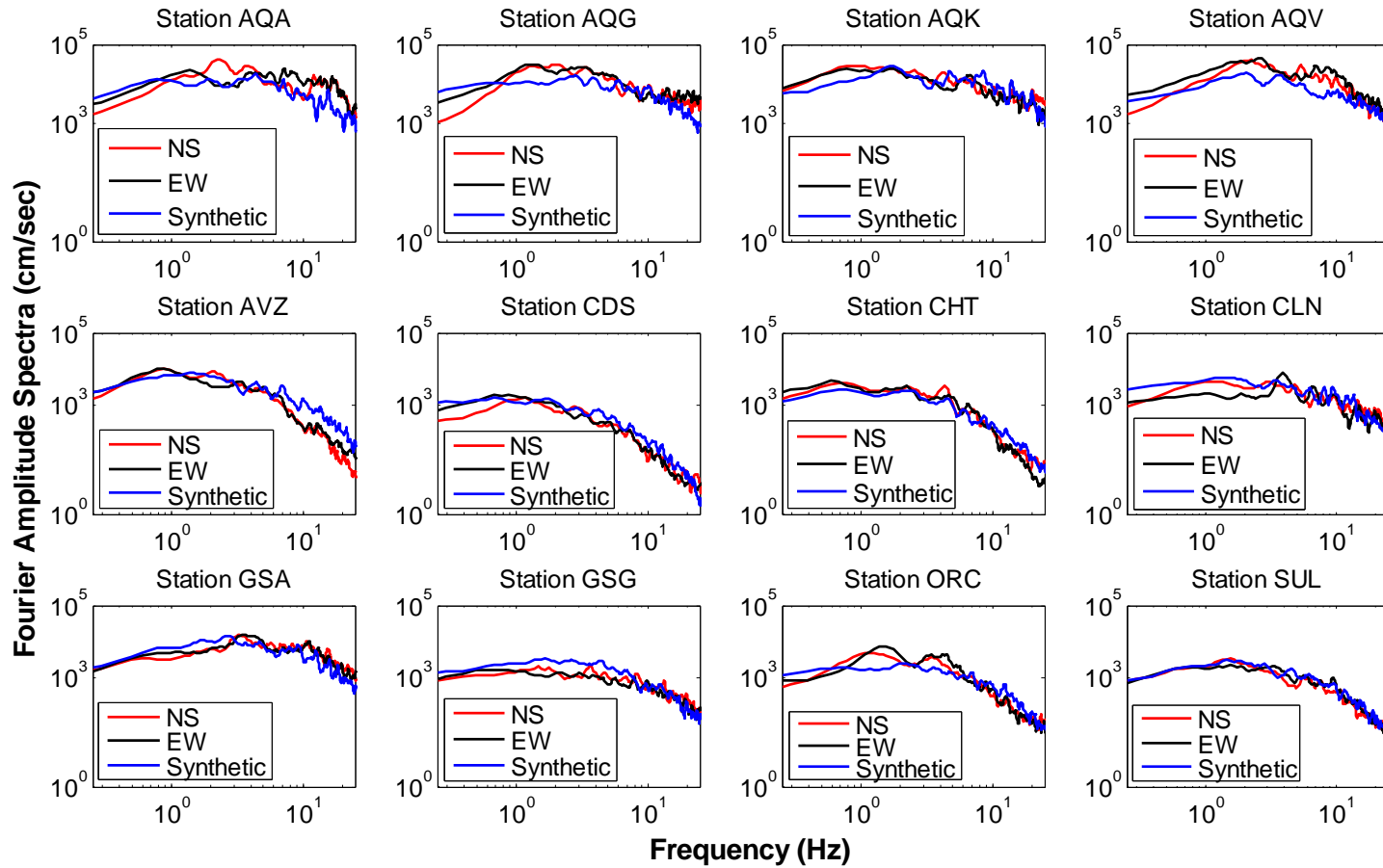


**Figure 4.6** Fourier amplitude spectra of forward stations that recorded the 2009 L'Aquila earthquake

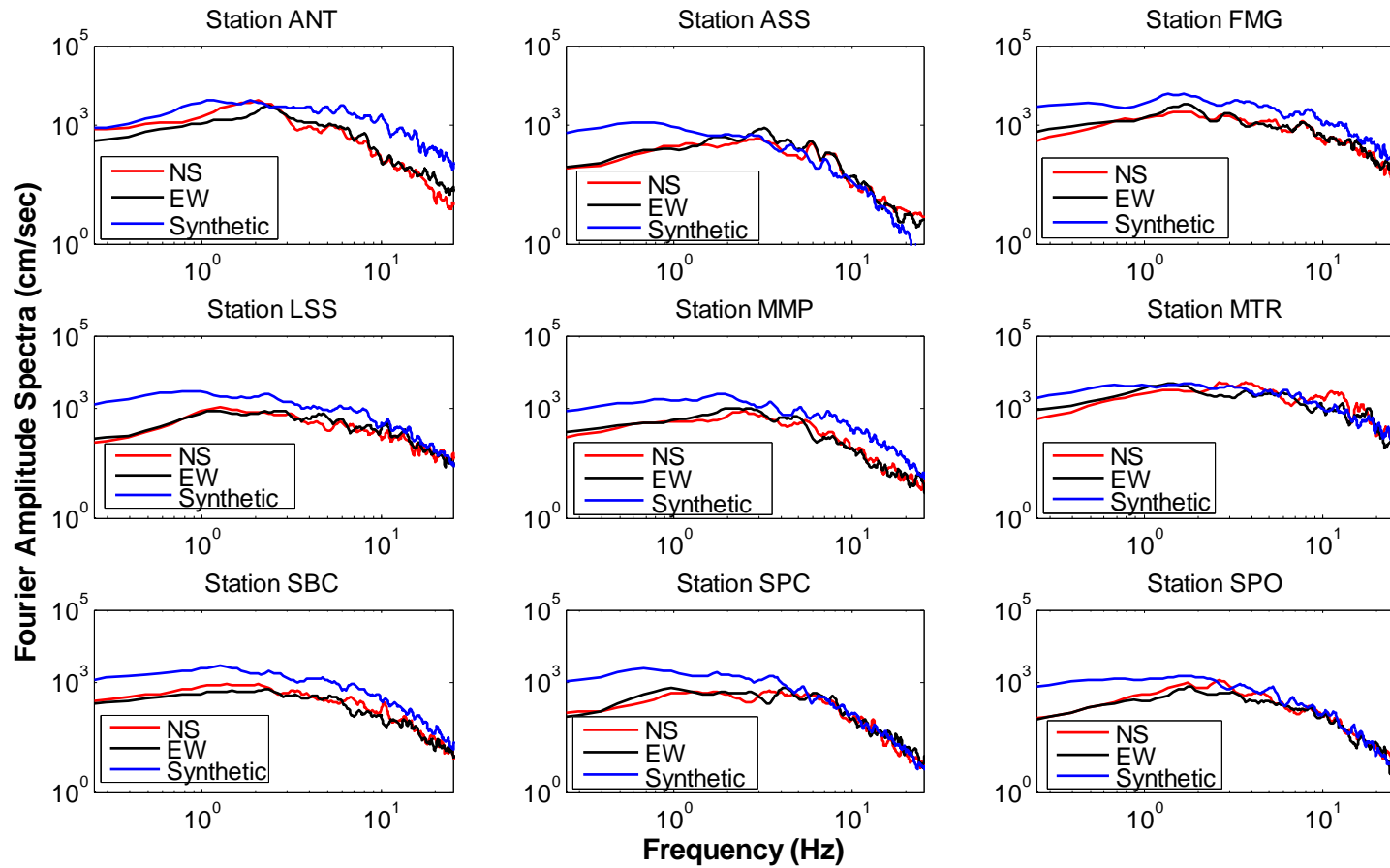


**Figure 4.7** Fourier amplitude spectra of backward stations that recorded the 2009 L'Aquila earthquake

5% damped acceleration response spectra of the recordings at a few selected stations are shown in Figure 4.8 along with the simulation results. The dotted line shows the EW component, dashed line shows the NS component of the observed recordings. The solid line stands for the synthetic records. The stations pairs for comparison are formed such that the two stations have similar Joyner-Boore distances but oriented in opposite directions with respect to rupture propagation. It is evident that there are significant differences in the response spectra of station pairs in terms of amplitudes. Due to the attenuation phenomena, distance is an important factor affecting the amplitudes. But these differences are not due to distance effects since the station pairs have similar distances from the fault plane. An alternative reason for amplitude differences is the local site conditions. In order to overcome this problem, the station pairs are chosen to be of the same site class. Indeed, all of the stations used in the comparisons are of type A class. Therefore, the station pairs are chosen such that the stations have similar propagation and site effects. Based on this discussion, the differences (if any) in the spectra of station pairs are most probably due to the directivity effects. The forward stations which are indicated with red lines are shown to have larger amplitudes. It is clear that the synthetic spectra of station pairs have similar amplitudes except the spectra at FMG and GSA stations. The difference in the synthetic spectra of FMG and GSA station pairs can be attributed to the distance difference between the stations. For near-field station pairs, small differences in distance are observed to make considerable differences in the amplitudes of the synthetic ground motions which is not the case for intermediate and far-field station pairs. From the spectra of other station pairs, it is observed that synthetic spectra are blind to station location. Whether the station is oriented in the rupture direction or opposite to the rupture direction does not make a significant difference in the simulations.

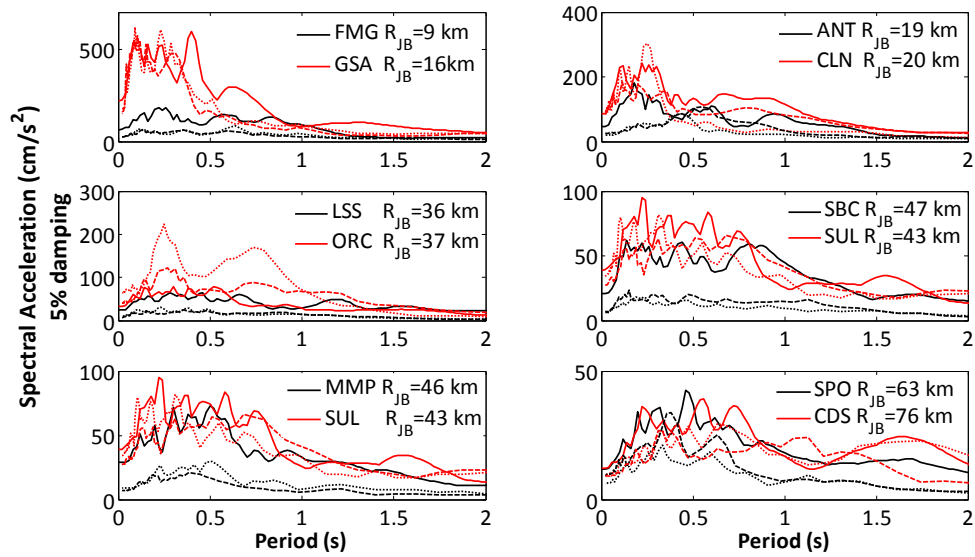


**Figure 4.8** Comparison of response spectra curves of equal distant stations. The dotted line shows the EW component, dashed line shows the NS component of the observed recordings. The solid line represents for the synthetic records. Forward stations are shown with red color whereas backward stations are shown with black color.

Figure 4.9 shows the comparison of  $PGA_{obs}/PGA_{syn.}$  and  $PGV_{obs}/PGV_{syn.}$  with respect to azimuth and Joyner-Boore distance of strong ground motions stations. The red circles stand for the forward stations whereas the blue circles represent the backward stations. As observed from the figures, the peak ground motion intensity values are always overestimated in the backward stations whereas forward stations have varying intensity parameters. The overestimation in backward stations confirms the inherent limitation of stochastic finite-fault modeling in simulating the directivity effects. On the other hand, the simulation results of forward stations do not show an obvious trend of underestimation or overestimation. The variation in the peak values of forward stations could be due to local site effects and the strong forward directivity effects which can be also only mimicked in the simulations (Assatourians and Atkinson, 2007).

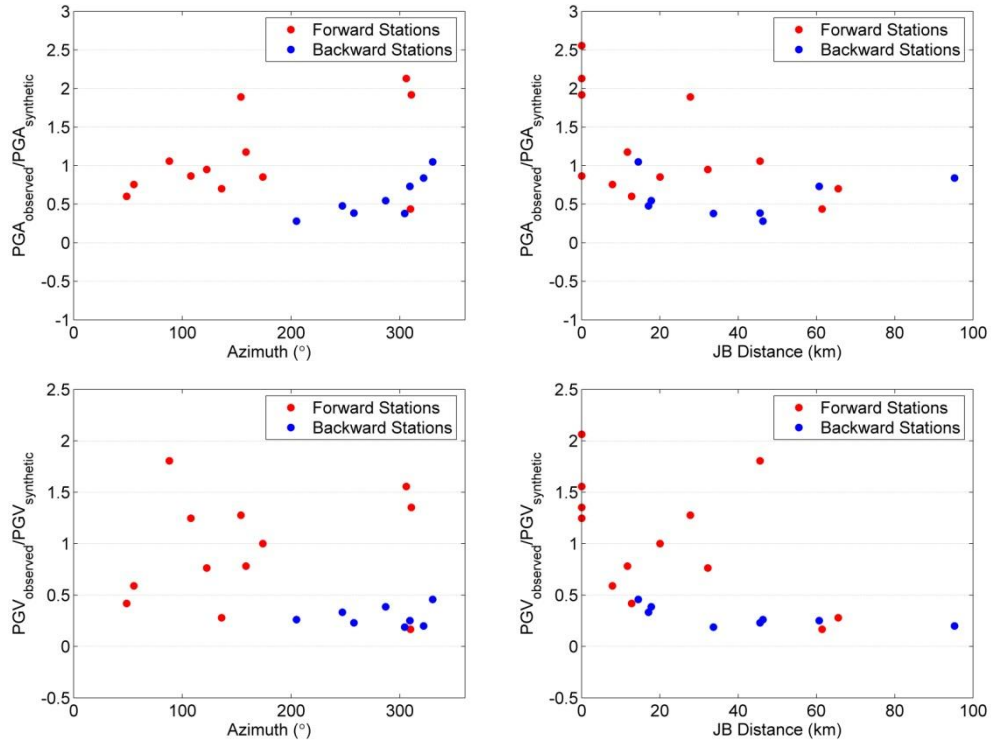


**Figure 4.9** Comparison of PGA and PGV values of observed and synthetic records with respect to azimuth and Joyner-Boore distance of strong ground motions stations

In summary, mainshock recordings of the 2009 L'Aquila earthquake are simulated to study the limitations of the methodology in terms of generating directivity effects which are highly pronounced in the 2009 L'Aquila earthquake.

The next case study explores Erzincan region. The regional seismic parameters of the region are studied with a parametric sensitivity approach.

## CHAPTER 5

### A SENSITIVITY ANALYSIS FOR EASTERN NORTH ANATOLIAN FAULT ZONE: ERZİNCAN CASE STUDY

#### 5.1 General

The eastern segments of the NAFZ are less investigated and have less dense seismic networks than the western ones. Thus, seismic parameters related to source, path and site effects are not well-established. A major objective of this case study is to investigate the ability of stochastic finite-fault simulations in determining regional seismic parameters of an area with a sparse seismic network. For this purpose, initially ground motions of 13 March 1992 Erzincan earthquake are simulated. Then, a sensitivity analysis around the optimum model parameters is presented. To quantify the error, misfit functions in terms of observed and synthetic Fourier Amplitude Spectra (FAS), PGA and PGV values are defined.

Section 5.2 gives background information about the Erzincan region including its seismicity and geology. The 13 March 1992 Erzincan earthquake and the strong ground motion stations that recorded the mainshock are also presented. In Section 5.3, regional parameters used in the ground motion simulations are introduced with the definitions of error functions which measure the misfit between the observed and synthetic ground motions. Ground motion simulation results with optimum parameters are also presented. In Section 5.4, a local sensitivity study is conducted around the optimum parameters determined in Section 5.3 to observe the variation of the results with respect to small perturbations in the input parameters. The sensitivity of the simulated ground motions to different parameters is then discussed in detail.

## 5.2 Background Information

Erzincan is considered to be one of the most hazardous regions of the world. Historical records evidence 18 large ( $M \geq 8$ ) earthquakes in the close vicinity of Erzincan within the past 1000 years (Barka, 1993). It is located in a seismologically very complex regime, in the conjunction of three active faults, namely North Anatolian, North East Anatolian and East Anatolian Fault Zones. These faults characterize the basic seismotectonics of the region. NAFZ displays right-lateral strike-slip faulting whereas EAFZ and North East Anatolian Fault Zones are left-lateral strike-slip in nature. The tectonic map of the region is displayed in Figure 5.1, top panel. In the bottom panel of the figure, red lines indicate the active faults existing in the region.

Erzincan basin is formed as a pull-apart basin because of the interactions between NAFZ and Ovacık Faults. It is the largest basin on the NAFZ with dimensions of 50 x 15 km in the close vicinity of Fırat River. The thickness of the alluvial layers goes up to several kilometers at the center of the basin and decreases near the mountain ranges (Lav *et al.*, 1993). From the mountain ranges in the north to Fırat River in the south, the size of the soil particles decreases in the order of gravel, sand, silt and clay (Öztaş, 1993).

As mentioned in Chapter 3, NAFZ is the most active fault zone in Turkey, yielding several destructive earthquakes in the past 100 years. The destructive earthquake sequence of NAFZ started with 1939 Erzincan Earthquake. This earthquake is the largest earthquake of the past century causing more than 30,000 fatalities and relocation of the city towards North (Akinçi *et al.*, 2001). Following this earthquake, the seismic sequence of this fault zone propagated towards westward. While another event was being expected on one of the western segments, on March 13, 1992 an earthquake of  $M_w=6.6$  (ERD) occurred on an eastern segment of NAFZ in Erzincan region, at the intersection of NAFZ and Ovacık faults. The earthquake was reported to have epicentral coordinates of 39.716°N and 39.629°E (ERD). In Figure 5.1, bottom panel, the epicenter of the earthquake is indicated with a purple star whereas

the strong ground motion stations that recorded the mainshock is indicated with black triangles. Although this earthquake is considered to be a moderate magnitude one, it caused over 500 deaths and an economic loss of 5-10 trillion Turkish Liras (Barka, 1993).

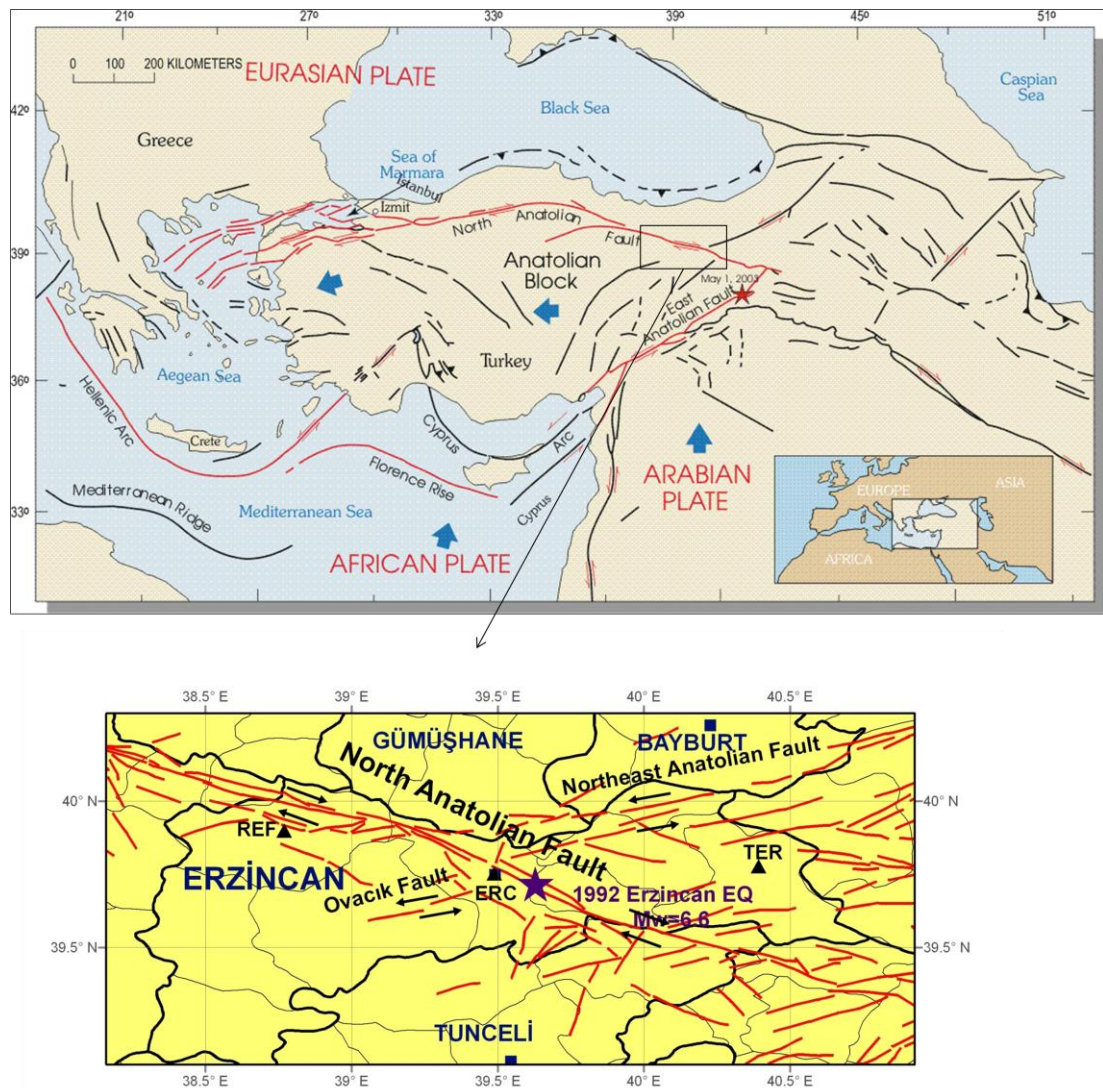


**Figure 5.1** Top Panel: Map showing the plate tectonics of the Anatolian Block

(adapted from [http://neic.usgs.gov/neis/eq\\_depot/2003/eq\\_030501/](http://neic.usgs.gov/neis/eq_depot/2003/eq_030501/))

Bottom Panel: Regional map showing the active faults (indicated with red lines) in the Erzincan region with the epicenter (indicated with a purple star sign) and strong ground motion stations of 1992 Erzincan earthquake (indicated with black triangles)

The mainshock of 13 March 1992 earthquake was recorded by three strong ground motion stations. The station names, codes, operating institutes, hypocentral coordinates, mean shear-wave velocity at 30 m ( $V_{S30}$ ), epicentral distances and the larger of the horizontal peak ground motion acceleration and velocity values are given in Table 5.1. The data given in Table 5.1 is obtained from Strong Ground Motion Database of Turkey, DAPHNE webpage, [http://daphne.deprem.gov.tr:89/2K/daphne\\_v4.php](http://daphne.deprem.gov.tr:89/2K/daphne_v4.php).

**Table 5.1** Information on the strong motion stations used in the validation of the finite-fault model of the 13 March Erzincan earthquake

Station	Code	Op. Name	Latitude (°N)	Longitude (°E)	Mean	Epi.	PGA ( $\text{cm/s}^2$ )	PGV ( $\text{cm/s}$ )
					$V_{S30}$ (m/s)	Dist (km)		
Erzincan- Merkez	ERC	ERD	39.752	39.487	-	12.83	478.77	108.43
Refahiye	REF	ERD	39.899	38.768	433	76.45	80.61	4.27
Tercan	TER	ERD	39.466	40.235	320	65.62	40.92	4.77

According to Barka (1993), 1992 Erzincan earthquake increased the probability of a larger magnitude earthquake in the city of Erzincan on NAFZ and/or Ovacık faults. Although it is seismically very active and other potential large earthquakes are expected in the future, there are neither sufficient studies nor a dense local seismic network to assess the seismicity in this region. This study aims to determine the seismological parameters that define the source, path and site effects in Erzincan region using ground motion simulations. The parameters are established among the few regional models from the literature as well as worldwide generic models using an optimization approach.

## 5.3 Ground Motion Simulation of 1992 Erzincan Earthquake

### 5.3.1 Simulation Parameters

For the validation of the ground motion simulation of 1992 Erzincan Earthquake, the three records obtained at the stations listed in Table 5.1 are utilized. In the search of optimum model parameters, a total of 6144 simulations are generated using all possible combinations of the parameters given in Table 5.2. Table 5.2 lists seismic parameters proposed for the Erzincan region in previous studies along with generic models based on worldwide seismic data.

For the slip distribution of this earthquake, uniform slip is used over the fault plane following the observations of Legrand and Delouis (1999). The duration of the ground motions is computed using the generic model of Herrmann (1985) given in Equation (3.2). The pulsing area percentage is assumed to be 50%.

For all of the simulations performed, two types of error functions are utilized to quantify the misfit between the observed and simulated ground motions. The first one defines the misfit in the frequency domain and the second one defines the misfit in terms of PGA and PGV values. Error measures in terms of the entire time series rather than the peak values exist in the literature (Dragovich and Lepage, 2009) but those measures are mostly used in the comparison of low-frequency ground motions and are not employed here.

The frequency domain error function is computed as follows: First, by dividing the observed horizontal FAS to the synthetic FAS at every frequency; one obtains a discrete error series as a function of frequencies. The discrete error values are then averaged over a frequency band of 0.5 to 20 Hz. Finally, the average of the error calculated for the three stations is taken as the final error representing the misfit in the frequency domain. The error formulation in frequency domain is given in Equation (3.4).

**Table 5.2** Alternative models used in the ground motion simulation of 1992 Erzincan earthquake

Fault Length	30 km (Pinar <i>et al.</i> , 1994)
	28 km (Wells and Coppersmith, 1994)
Fault Width	15 km (Pinar <i>et al.</i> , 1994)
	12 km (Wells and Coppersmith, 1994)
Hypocentral Depth	9 km (Bernard <i>et al.</i> , 1997)
	22.6 km (ERD)
Stress Drop	25 bar (Pinar <i>et al.</i> , 1994)
	100 bar (Akinci <i>et al.</i> , 2001)
	82 bars (Mohammedioun and Serva, 2001)
	65 bars (Mohammedioun and Serva, 2001)
Q	$40f^{0.45}$ (Akinci <i>et al.</i> , 2001)
	$35f^{0.83}$ (Akinci and Eyidogan, 1996)
	$47f^{0.86}$ (Akinci and Eyidogan, 1996)
	$29f^{1.03}$ (Akinci and Eyidogan, 1996)
	$59f^{0.81}$ (Akinci and Eyidogan, 1996)
	$122f^{0.68}$ (Grosser <i>et al.</i> , 1998)
	$57f^{1.22}$ (Gürbüz <i>et al.</i> , 1993)
$82f^{0.87}$ (Gürbüz <i>et al.</i> , 1993)	
Geometric Spreading	$R^{-1}$ $R \leq 30$ km (Herrmann, 1985)
	$R^{-0.5}$ $R > 30$ km
	$R^{-1.1}$ $R \leq 25$ km (Akinci <i>et al.</i> , 2001)
	$R^{-0.5}$ $R > 25$ km
Site Amplification Factors	NEHRP C Amp. Fact. (Boore and Joyner, 1997)
	Generic Soil Amp. Fact. (Boore and Joyner, 1997)
	NEHRP D Amp. Fact. (Boore and Joyner, 1997)
Kappa	0.035
	0.045

The second type of error used in this study computes the misfit in the PGA and PGV values. These parameters are the most common parameters defining the intensity of ground motions and they are frequently used by the engineering community, thus it is essential to assess the goodness of fit in terms of them. Further definitions of error,

determining the fit in other spectral values such as spectral displacement, velocity or acceleration are also possible.

The misfit function in PGA values is formulated as follows:

$$\text{Error} = \frac{1}{n} \sum_{i=1}^n \frac{\text{PGA}_{\text{obs.}}}{\text{PGA}_{\text{synt.}}} \quad (5.1)$$

In Equation (5.1),  $n$  is the number of stations.  $\text{PGA}_{\text{obs.}}$  is defined as the geometric average of the two horizontal components which is represented as  $\text{PGA}_{\text{obs.}} = \sqrt{\text{PGA}_{\text{H1}} * \text{PGA}_{\text{H2}}}$  where  $\text{PGA}_{\text{H1}}$ ,  $\text{PGA}_{\text{H2}}$  are the PGA values recorded in the two horizontal components (Hartzell *et al.*, 1999). Equation (5.1) is also used to determine the misfit in PGV values by replacing the PGA values with PGV values.

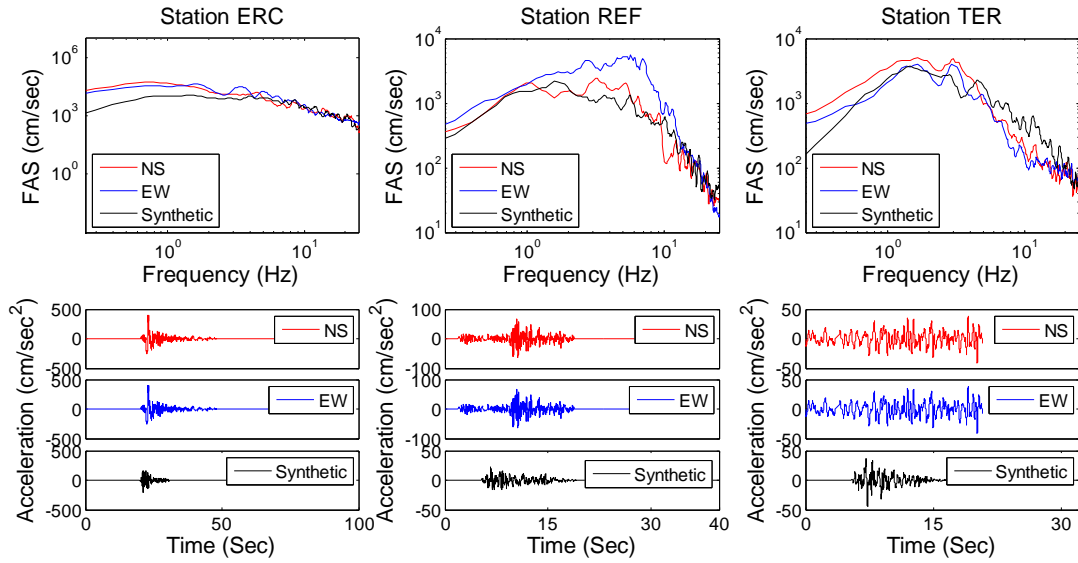
In this study, frequency-domain error values are used as the major indicator of goodness of fit for the synthetics since the deterministic spectrum is defined in the frequency domain. In addition, the time-domain representation of the signal is random and it shows variability for each simulation.

Table 5.3 shows the optimum parameters determined as the seismic parameters of the Erzincan region. These parameters minimized the overall frequency-domain error among 6144 sets of simulations.

Since it is not possible to visualize the results of all 6144 sets of simulations, only the results of the simulations with the optimum parameters are shown in Figure 5.2 along with the observed values.

**Table 5.3** Regional parameters of Erzincan region

<b>Parameter</b>	<b>Value</b>
Fault orientation	Strike: 123° Dip: 86°
Fault dimensions	28 x 12 km
Moment Magnitude	6.6
Depth of the Top of Fault Plane	3 km
Subfault Dimensions	2 x 2 km
Stress Drop	82 bars
Crustal Shear Wave Velocity	3500 m/s
Crustal Density	2800 kg/m <sup>3</sup>
Pulsing Area Percentage	50%
$\kappa_0$	0.045
Duration Model	0.05*R
Attenuation model, Q(f)	122f <sup>0.68</sup>
Geometric Spreading	R <sup>-1</sup> if R<30 km R <sup>-0.5</sup> if R≥30 km
Windowing Function	Saragoni-Hart
Local Amplification	NEHRP D Amplification (Boore and Joyner, 1997)



**Figure 5.2** FAS and acceleration-time series of the observed and synthetic ground motions of 1992 Erzincan earthquake

In Station ERC, although a satisfactory fit is obtained in the high frequency portion, there is a clear underestimation of the synthetics in the lower frequencies. Due to the high amplitude and short duration peaks in the recordings, the acceleration time histories of station ERC imply that the records are subjected to forward directivity effects. As verified in the previous chapter, stochastic ground motion simulation methodology is limited in simulating directivity effects (Assatourians and Atkinson, 2007). The limitation of the method in simulating directivity effects and the generic duration model are the most probable causes of the misfit in the low-frequency portion of the ground motions recorded at the station ERC.

The North-South (NS) component of station REF is closely matched by the synthetic spectra. On the other hand, there is a clear discrepancy between the synthetic spectra and EW component of the observed ground motion. The EW component displays a clear amplification around 5 Hz which seems to be due to local soil amplification effect.

The differences in the FAS of observed and synthetic records of station TER can be attributed to the insufficient representation of soil response. It must be noted that generic amplifications does not capture the resonant frequencies and amplifications that are specific to the region considered. Better assessment of soil amplification and diminution would provide better results.

It is clear from Figure 5.2 that the duration model used in the simulations is not successful in simulating the duration of S-wave portion of the seismograms recorded in the Erzincan region. As mentioned previously, Erzincan region is located on an alluvial basin. When the seismic waves travel through an alluvial basin, they are exposed to several reflections and refractions which increase their durations. This phenomenon is named as “basin effect”. The recordings obtained at Erzincan region experienced these affects causing an increase in the duration of the recordings. A regional model would better simulate the ground motion durations.

### **5.3.2 Variation in the Simulation Results with respect to Alternative Models**

Next, to see the variation in misfit for the alternative models used in defining input parameters, each input parameter is varied alone by fixing all other parameters to their optimum value given in Table 5.3. Figure 5.3 shows the errors computed using different combinations of input parameters with bar charts. In the figures, the parameters are grouped to show the effect of source, path and site parameters individually.



**Figure 5.3** Errors computed using different combinations of input parameters showing the effect of source, path and site parameters individually

It is clear from Figure 5.3 that the synthetic spectra are mostly affected by the path parameters. The errors in the frequency domain reach up to 3 and the errors in the PGA and PGV values exceed 6 by changing only the path parameters. On the other hand, an error of maximum 1 in the frequency domain and 4.5 in the PGA and PGV is obtained by changing the source parameters. The lowest difference in the error comes from the site effects with the frequency domain errors reaching 0.5 and PGA and PGV errors reaching 3. These findings suggest that the simulations are most sensitive to propagation (path) effects. However, to derive a solid conclusion on the effect of parameters on misfit amplitudes, a local parameter sensitivity study around optimum parameters must be conducted. The next section investigates the sensitivity of ground motion simulation methodology to perturbations in optimum input parameters.

#### 5.4 A Local Sensitivity Analysis Around the Optimum Parameters

In the previous section, among several models proposed for the Erzincan region, optimum parameters are determined based on a set of 6144 forward simulations. In order to see the effects of small perturbations in the input parameters on simulation results, a local sensitivity study is performed around selected optimum parameters. These parameters are varied with increments of 10% in both positive and negative directions and the sensitivity of simulations in terms of FAS, PGA and PGV is investigated. The sensitivity index (SI) is defined as the difference in the simulation with the perturbed input parameters with respect to the simulation with optimum parameters. SI definitions in the frequency and time domain are as follows:

$$SI_f = \frac{1}{n_{\text{freq.}}} \sum_{0.5 \leq f \leq 20 \text{ Hz}} \log \left| \frac{A_i(f)_{\text{perturbed}}}{A_i(f)_{\text{optimum}}} \right|$$

$$SI_{\text{PGA}} = \frac{\text{PGA}_{\text{perturbed}} - \text{PGA}_{\text{optimum}}}{\text{PGA}_{\text{optimum}}} \quad (5.2)$$

$$SI_{PGV} = \frac{PGV_{\text{perturbed}} - PGV_{\text{optimum}}}{PGV_{\text{optimum}}}$$

where  $SI_f$  is the sensitivity index in the frequency domain and  $SI_{PGA}$  and  $SI_{PGV}$  are the sensitivity indices of PGA and PGV, respectively.  $n_{\text{freq.}}$  is the number of frequencies used in the simulation and  $A_i(f)$  is the acceleration spectra of the  $i^{\text{th}}$  station.

#### 5.4.1 Sensitivity of Simulations with respect to Source Parameters

The parameters defining the source model in stochastic ground motion simulations are moment magnitude, fault dip and strike, fault length and width, depth of the top of the rupture plane, stress drop, rupture velocity and slip distribution. In the simulation of a particular earthquake, moment magnitude, the dip and strike angles of the fault plane are generally well-constrained from inverse analyses of teleseismic and/or strong ground motion recordings. The other source parameters such as fault length and width, depth of the top of the rupture plane and stress drop constitute the most ambiguous part of the source mechanism. When detailed studies for these parameters do not exist, empirical relationships are frequently used.

Stress drop is the key parameter in the definition of the source. This subsection investigates the sensitivity of ground motion simulations to variations in the stress drop. Stress drop value is varied alone by fixing the other input parameters to their optimum values given in Table 5.3. Figure 5.4 displays the frequency domain, PGA and PGV sensitivity indices corresponding to different stress drop values.

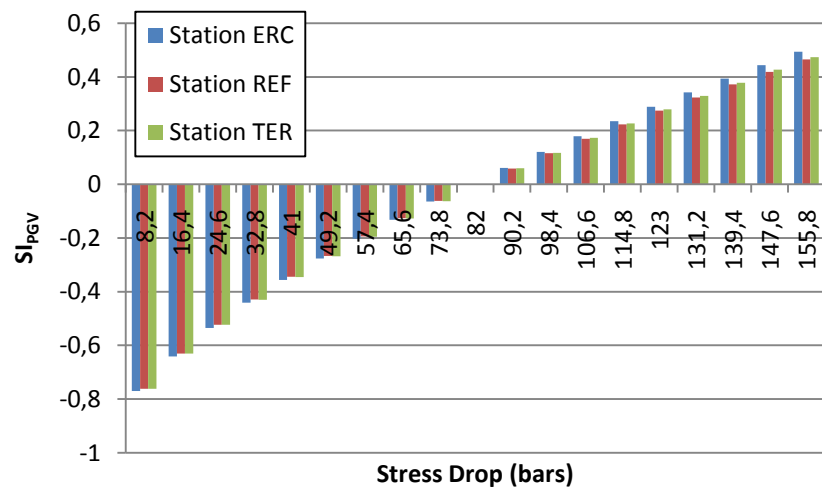
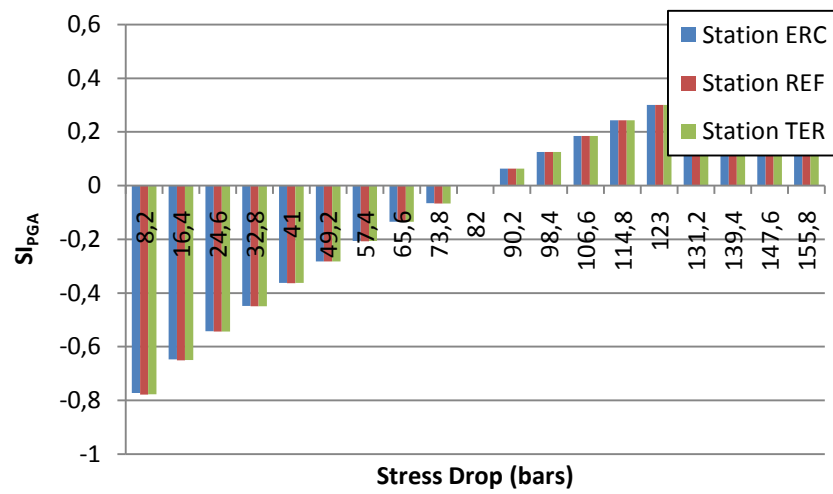
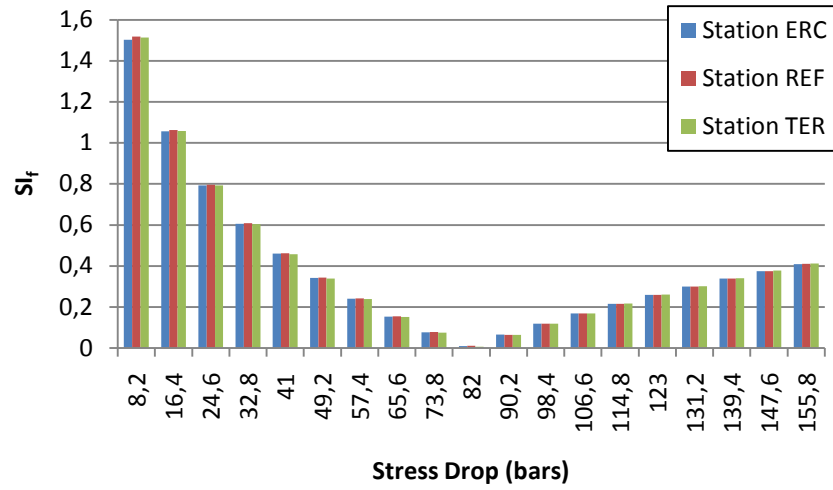


**Figure 5.4** Sensitivity indices with respect to different stress drop values

As observed from Figure 5.4, FAS is visibly sensitive to stress drop. Although the source parameters affect low to intermediate frequencies, it is noted that stress drop affects a wider frequency range resulting in considerable effects on simulations. The slope of  $SI_f$  corresponding to decreasing stress drop values is greater than that of increasing values of stress drop. This is because the seismic moment is a nonlinear function of the stress drop.

From the sensitivity plots of PGA and PGV values with respect to different stress drop values, it is observed that increasing stress drop yields higher peak ground motion intensity values. Reducing the stress drop value by 10% causes 7% decrease in both PGA and PGV values; whereas increasing the stress drop values by 10% causes 6% increment in the PGA and PGV values. In summary, the peak ground motion intensity parameters are sensitive to stress drop. Thus, it is important to estimate this parameter accurately for reliable simulations.

Another significant parameter in the definition of source is the depth of the fault plane. Numerical exercises involving a sensitivity analysis around the depth parameter showed that varying the depth of rupture plane changes the results for multiple reasons. First, by varying the depth of the rupture plane, one varies the effective distance of the fault plane from the observation point of interest. This variation affects the other parameters such as geometrical spreading and anelastic attenuation function which is  $e^{-\frac{\pi f R}{Q(f)\beta}}$ . Thus, the sensitivity results vary with respect to the distance and frequency range considered. Such a local sensitivity study must involve detailed analyses of all filters used in the simulations and is found to be beyond the scope of this study.

#### **5.4.2 Sensitivity of Simulations with respect to Path Parameters**

In this study, the sensitivity of ground motion simulations to path parameters is tested in terms of the quality factor parameter. As mentioned before, quality factor is

frequency-dependent and is represented as  $Q = Q_0 f^n$ . The sensitivity of ground motions to different  $Q_0$  and  $n$  values is shown in Figure 5.5.

Figure 5.5 suggests that the effect of  $Q$  value is significant in intermediate-to-far distances. Station ERC is located at an epicentral distance of 12 km whereas stations REF and TER have epicentral distances of approximately 76 and 65 km, respectively. It is observed from Figure 5.5 that as the distance of the station from the fault plane increases, the effect of both  $Q_0$  and  $n$  values in FAS, PGA and PGV values increase. Since  $Q$  effects are not obvious in near-field distances, the following discussions are based on stations REF and TER.

Figure 5.5 suggests that decreasing the  $Q_0$  values changes the frequency domain representations exponentially whereas increasing it causes a more gradual change. This observation holds true for  $n$  values as well, but with less significant effects.

By increasing  $Q_0$  value, one obtains lower attenuation and thus higher amplitudes. Thus, the increasing trend in  $SI_{PGA}$  and  $SI_{PGV}$  values is expected. A  $Q_0$  value 10% smaller than the initial value produces 7% lower PGA whereas a 10% larger  $Q_0$  yields 6% higher PGA. The decay is smoother for PGV values. A  $Q_0$  value 10% smaller than the initial value produces 5% lower PGV whereas 10% larger  $Q_0$  leads to 4% higher PGV in the simulations.

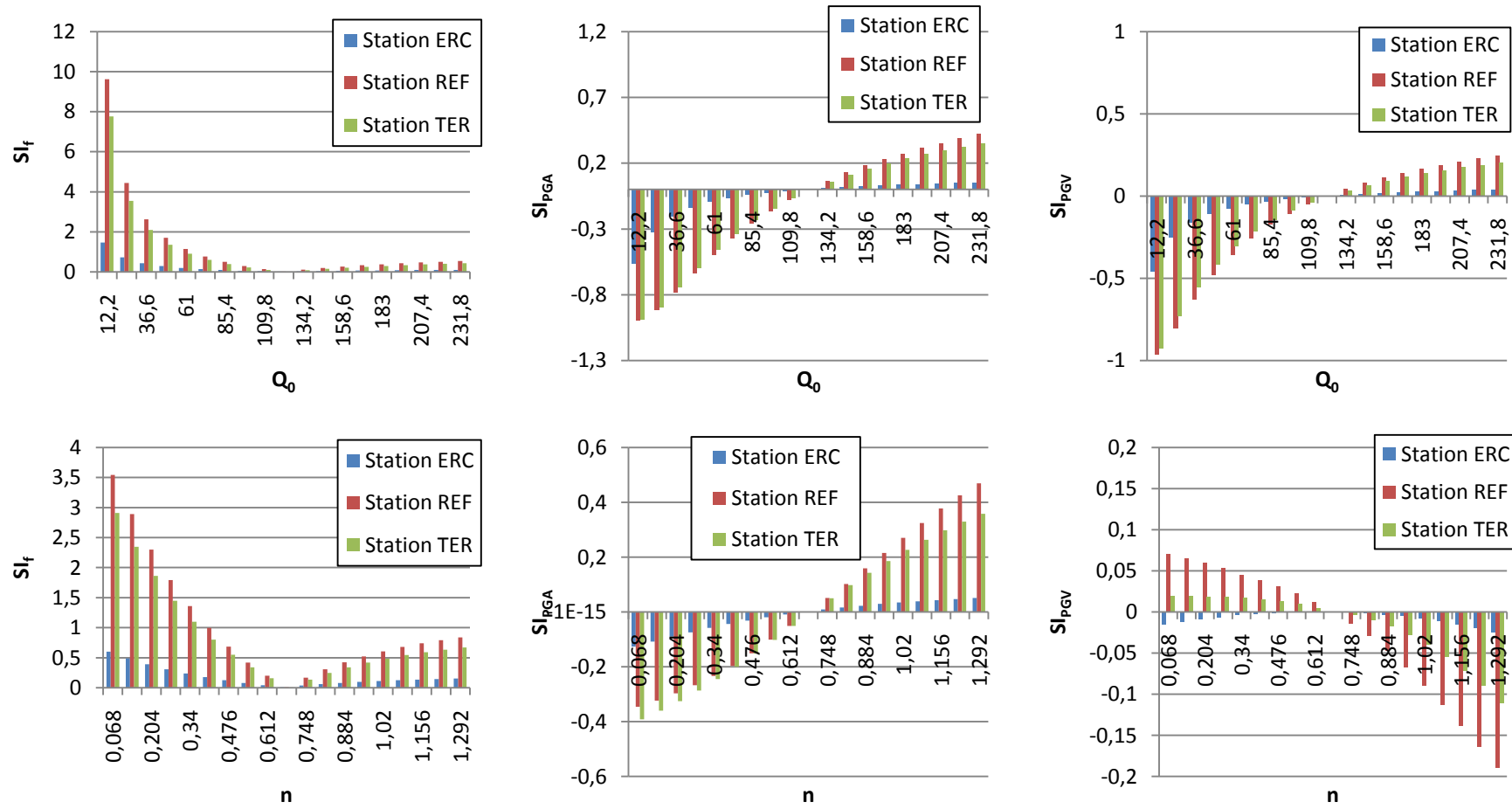


**Figure 5.5** Sensitivity indices with respect to different quality factors

By increasing  $n$  value, one increases the dependence of FAS on different frequency ranges. For frequencies higher than 1 Hz, an increment in  $n$  value has the effect of decreasing the amount of attenuation and thus increasing the amplitudes. However, for frequencies lower than 1 Hz, the opposite holds true. The dependence on the frequency range leads to variable behaviors of PGA and PGV values. Since PGV is affected by low-to-intermediate frequencies, in this frequency range an increment in  $n$  value causes amplitudes to decrease. On the other hand, increasing  $n$  values causes an increase in the amplitudes of frequencies that affect PGA values. This explains the increase of PGA and the decrease of PGV with increasing  $n$ . 10% reduction in  $n$  value causes 5% increase in PGA and 1% decrease in PGV, whereas 10% increment in  $n$  value causes 5% decrease in PGA and 1% increase in PGV.

#### **5.4.3 Sensitivity of Simulations with respect to Site Parameters**

The parameters defining the site model in stochastic ground motion simulations are frequency-dependent site amplification factors and diminution factor. In this study kappa operator is used as the diminution factor. The sensitivity results of kappa operator are shown in Figure 5.6.

In the frequency domain, it is clear that changing the kappa operators linearly increases the difference in the simulations. Since the kappa values acts as diminution filters, increasing them decreases the amplitudes. The variation in PGA and PGV is exponential with a slowing rate since the spectrum is dependent on kappa values by  $e^{-\pi\kappa f}$ . Changing kappa by 10% yielded 6% different PGA values and 2% different PGV values. The sensitivity of PGA with respect to kappa is higher since kappa filter affects mostly the higher frequencies.

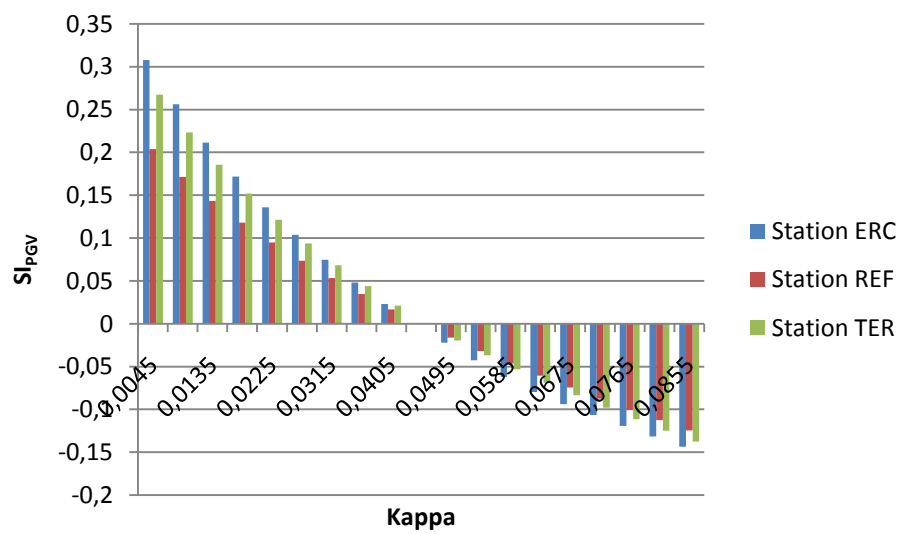
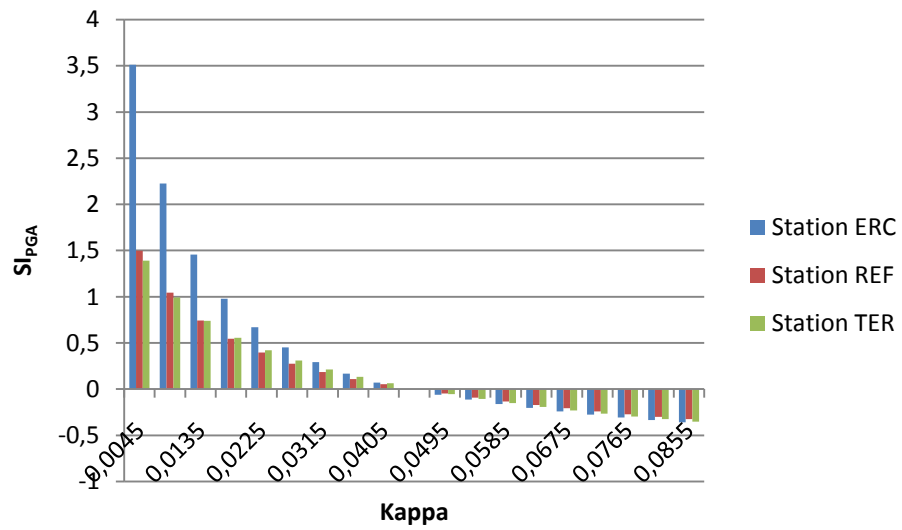
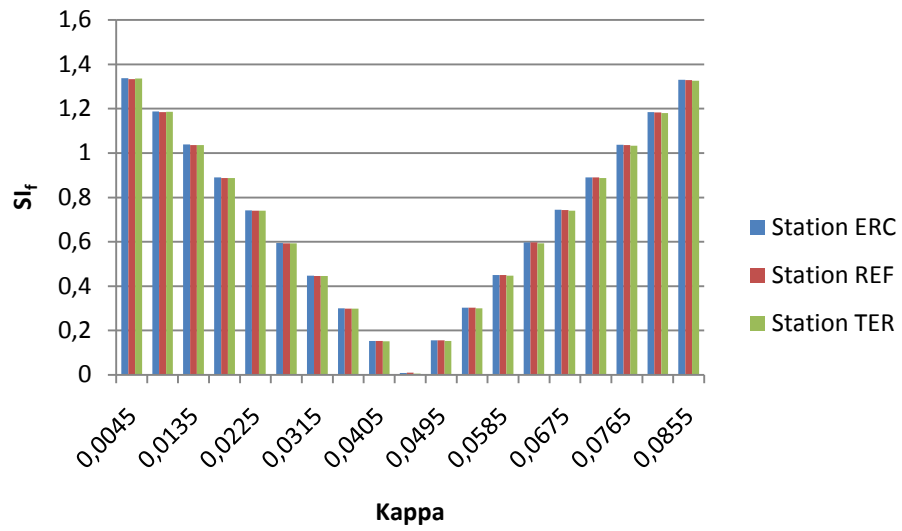


**Figure 5.6** Sensitivity indices with respect to different kappa operators

To summarize, this chapter explores Erzincan region that is characterized by high seismic activity. Despite the seismicity in the region, it is not well-studied seismologically. In this case study, seismic parameters of Erzincan region are determined from a large set of simulations with alternative models using an error minimization approach. Afterwards, the precision of the optimum parameters are investigated through a parametric sensitivity analysis. Among the parameters tested which includes stress drop, quality factor and kappa operator, the most sensitive parameter turned out to be the crustal shear-wave quality factor. Stress drop and kappa values are confirmed to be other important parameters in ground motion simulations.

## CHAPTER 6

### CONCLUDING REMARKS

#### 6.1 Summary

This thesis presents ground motion simulations of large earthquakes in Düzce, L'Aquila and Erzincan regions. The method utilized is the stochastic finite-fault ground motion simulation technique with a dynamic corner frequency approach. This method is known for its efficiency in generating high frequency components of large amplitude shear-waves. The main objective of this thesis is to study seismic properties of Düzce, L'Aquila and Erzincan regions by validation of synthetics with records from past large earthquakes that occurred in these regions.

In the Düzce case study, the simulated waveforms, which are generated using the regional parameters determined in this study, are validated against the observed ground motions of 1999 Düzce earthquake. The simulation of 1999 Düzce earthquake is challenging for multiple reasons. There are only a few records obtained in the near to intermediate field distance range from the fault plane. The second issue is the seismologically complex character of the earthquake. It is evidenced by supershear rupture propagation and forward directivity effects. Furthermore, the region is not well studied seismologically. In this case study, after validating the regional parameters with the observed ground motions, the method is further verified by comparisons of the attenuation of synthetics with the existing GMPEs and the spatial distribution of observed damage.

Next, 2009 L'Aquila earthquake is simulated. The case study of 2009 L'Aquila earthquake is entirely different than the Düzce study. The regional parameters of

L'Aquila region are better-constrained from previous studies when compared to Düzce region. In addition, 2009 L'Aquila earthquake is recorded by several near field strong ground motion stations. However, the earthquake is characterized by significant directivity effects observed in the records. The limitations of the stochastic method in terms of generating directivity effects are investigated with the simulation of this particular earthquake.

The final case study regarding Erzincan region is remarkably different from both Düzce and L'Aquila studies. There are very few studies for the regional parameters and the last large earthquake, 1992 Erzincan earthquake, yielded only 3 strong ground motion records. This earthquake is used in the verification simulations in this case study. By minimizing the error between synthetics and the observed ground motions for a set of 6144 simulations, the regional parameters that provide the best-fit to observed Fourier amplitude spectra is determined. Later, the effects of small perturbations in optimum input parameters are investigated with a sensitivity study.

## **6.2 Observations And Conclusions**

For regions of sparse or no seismic stations, ground motion simulations provide earthquake engineers the peak parameters and frequency content of potential ground motions in regions of interest. These parameters are essential for reliable seismic hazard estimation, damage mitigation and earthquake resistant design. Ground motion simulations are important not only for providing the peak seismic design parameters but also for offering an understanding of the earthquake mechanisms and the properties of the media in the region of interest.

In this study, stochastic ground motion simulation methodology is adopted. The observations are as follows:

- It is verified that stochastic finite-fault simulation methodology effectively generates the high frequency shear-wave portion of ground motions. It provides physics-based simulation of earthquakes.
- From the FAS of the synthetics, stochastic finite-fault simulation methodology is observed to be inadequate in generating the low frequency content of ground motions. Low frequency waves are deterministic in nature and when velocity profile in the region of interest is known, by numerical solutions of the wave propagation equation, one can obtain long-period ground motions. Assessment of long period ground motions is essential for engineering structures with long periods. In order to generate realistic broadband simulations, one should combine the stochastic method with deterministic methods.
- In alluvial basins, an enhancement in low frequencies occurs which increases the duration of the ground motions. This phenomenon is called basin effects and it is important in terms of structural response as the structures will be exposed to longer seismic excitations. Another observation made in this study is the limitation of the stochastic ground motion simulation methodology in generating these effects. To simulate the basin effects properly, one needs an accurate wave velocity model and a deterministic technique.
- Forward directivity is evidenced by short duration, high amplitude pulses whereas backward directivity is identified with long duration and small amplitude ground motions. The directivity effects are very important and must be assessed carefully since they cause significant damage in the near fault urban regions. It is observed that in this technique the directivity effects are only mimicked at very near field distances due to the finite dimensions of the fault plane.
- The computer program EXSIM includes an analytical solution of directivity pulses that can be superimposed onto the synthetic motion. This analytical pulse option can be used in the validation of a particular earthquake where the observed pulse is known in advance. But for the generation of scenario motions or blind

simulations, it is not possible to predict the directivity pulse beforehand since the pulse is highly random.

- It is observed that the near-field ground motions are governed by source effects. Source effects encompass very complex phenomena and they are random in nature. However, in the intermediate to far field distances, propagation effects overcome the source effects. Propagation effects are more quantifiable compared to source effects. Thus, using stochastic method, it is possible to assess the design loads from potential earthquakes which the structures, located at intermediate to far field distances from the fault zones, will be exposed to during their lifetimes.
- One of the most important parameter that affects the synthetic ground motions is shown to be the local soil response. Site amplification can change the duration, frequency content and amplitudes of the ground motions at all distances. Thus, it is crucial to assess the local soil conditions and estimate corresponding site response in regions with high seismic hazard.
- Simulations are observed to be most sensitive to crustal quality factor. Since it is frequency-dependent, the interaction between other input parameters and crustal quality factor can produce significant changes in the simulations. Thus, it is very important to utilize a crustal quality factor that well represents the regional anelastic losses in the study area.
- It is very important to use regional parameters with high accuracy in the simulations. In cases where regional parameters are not known, it is not reasonable to depend on simulation results unless the simulations are validated against observed ground motions.
- It is observed that the attenuation of synthetics well correlates with GMPES. It must be noted that synthetics are physics-based simulations of real earthquakes. Thus, synthetic peak ground motion intensity parameters can be used to augment GMPEs. Also in regions for which GMPEs are not available, simulations can be used in determining the attenuation of peak parameters with distance.

### 6.3 Future Work and Recommendations

- The regional seismic parameters determined in this study for Düzce, Erzincan and L'Aquila can be developed further and used as input into other studies that assess the seismic hazard in the regions of interest.
- The ground motions simulated in this study can be combined with low frequency ground motions generated from deterministic methods in order to obtain broadband simulations. It must be noted that deterministic methods can only be used in the presence of wave velocity models.
- With better assessment of the frequency-dependent site amplification factors, the high-frequency synthetic motions obtained in this study can be further improved.
- Ground motion simulations can be used as input to a variety of studies. As deterministic hazard measures, they can be combined with building fragility functions in order to estimate the loss from potential earthquakes (Ugurhan *et al.*, 2010). Synthetic motions can also be used in seismic hazard analysis studies in determining the peak ground motion intensity values instead of GMPEs.
- It is possible to use the results of this study in seismic response analyses of engineering structures. Rather than using real records from other regions with different seismotectonic features, one can perform time history analyses with synthetic records simulated particularly for the region of interest.
- A wave velocity model provides significant information about the wave propagation properties and soil response in a region of interest. These models are essential in determining the seismic response of alluvial basins in particular. Although in Turkey there are various basins near the fault zones with deep sediment deposits, wave velocity models with fine resolution do not exist. Thus, velocity models must be built for better assessment of seismic hazard in these regions.

- For the better assessment of potential ground motions and seismic hazard, it is very important to increase the number of strong ground motion stations under operation and widen the seismic networks all over the world.

## REFERENCES

- Aki, K. (1957). Space and time spectra of stationary stochastic waves with special reference to microtremors, *Bull. of the Earthquake Research Institute*, **35**, 415-457.
- Aki, K. (1967). Scaling law of seismic spectrum, *J. Geophys. Res.* **72**, 1217–1231.
- Aki, K. (1968). Seismic displacement near a fault, *J. Geophys. Res.*, **73**, 5359-5376.
- Aki, K. (1980). Attenuation of shear waves in the lithosphere for frequencies from 0.05 to 25 Hz, *Phys. Earth Planet. Inter.*, **21**, 50-60.
- Aki, K. and P. G. Richards (1980). *Quantitative Seismology*, W. H. Freeman and Co., San Francisco, 932 pp.
- Akinci, A. and H. Eyidogan (1996). Frequency dependent attenuation of *S* and coda waves in Erzincan region (Turkey), *Phys. Earth Planet. Interiors* **97**, 109–119.
- Akinci A., L. Malagnini, R. B. Herrmann, N. A. Pino, L. Scognamiglio, and H. Eyidogan (2001). High-Frequency Ground Motion in the Erzincan Region, Turkey: Inferences from Small Earthquakes, *Bull. Seismol. Soc. Am.* **91**, 1446– 1455.
- Akinci, A., L. Malagnini, R. B. Herrmann, R. Gok, and M. B. Sorensen (2006). Ground motion scaling in the Marmara region, Turkey, *Geophys. J. Int.* **166**, 635–651.
- Akinci, A. (2010). Personnel Communication.
- Akinci A., L. Malagnini and F. Sabetta (2010). Characteristics of the strong ground motions from the 6 April 2009 L'Aquila earthquake, Italy, *Soil Dyn Earthquake Eng*, doi:10.1016/j.soildyn.2009.12.006.
- Akcar, S. and Bommer, J.J. (2007). Prediction of elastic displacement response spectra in Europe and the Middle East, *Earthquake Engng Struct. Dyn.* **36**, 1275-1301.
- Ambraseys, N. (2009). *Earthquakes in the Mediterranean and Middle East: A Multidisciplinary Study of Seismicity up to 1900*, Cambridge University Press.
- Anderson, J. and S. Hough (1984). A model for the shape of the Fourier amplitude spectrum of acceleration at high frequencies, *Bull. Seism. Soc. Am.* **74**, 1969–1993.

- Anderson, J., Y. Zeng, and H. Sucuoglu (2001). Analysis of Accelerations from the 1 October 1995 Dinar, Turkey, Earthquake, *Bull. Seism. Soc. Am.* **91**, 1433–1445.
- Ansal A., A. Akinci, G. Cultrera, M. Erdik, V. Pessina, G. Tönük and G. Ameri (2009). Loss estimation in Istanbul based on deterministic earthquake scenarios of the Marmara Sea region (Turkey), *Soil Dyn. and Earthq. Eng.* **29**, 699–709.
- Assatourians, K. and G. M. Atkinson (2007). Modeling variable-stress distribution with the stochastic finite-fault technique, *Bull. Seism. Soc. Am.* **97**, 1935-1949.
- Asten, M.W., T. Dhu, A. Jones and T. Jones (2003). Comparison of shear velocities measured from microtremor array studies and SCPT data acquired for earthquake site hazard classification in the northern suburbs of Perth W.A., *Proceedings of a Conference of the Australian Earthquake Engineering Soc.*, 12 p., Melbourne.
- Asten, M., A. Askan, E. E. Ekinoglu, F. N. Sisman and B. Ugurhan (2010). Site Characterization in Northwestern Turkey Based on Spatial Autocorrelation Technique: A Comparative Study on Site Hazard Estimation, *Seism. Res. Let.* **81**, 283.
- Atkinson, G. M. (1984). Attenuation of Strong Ground Motion in Canada from a Random Vibrations Approach, *Bull. Seismol. Soc. Am.* **74**, 2629–2653.
- Atkinson, G. M and W. Silva (2000). Stochastic Modeling of California Ground Motions, *Bull. Seism. Soc. of Am.* **90**; 255-274.
- Atkinson, G. (2004). Empirical attenuation of ground motion spectral amplitudes in southeastern Canada and the northeastern United States, *Bull. Seism. Soc. Am.* **94**, 1079 –1095.
- Atkinson, G. M., K. Assatourians, D. M. Boore, K. Campbell and D. Motazedian (2009). A Guide to Differences between Stochastic Point-Source and Stochastic Finite-Fault Simulations, *Bull. Seism. Soc. Am.* **99**, 3192-3201.
- Bao, H., J. Bielak, O. Ghattas, L. Kallivokas, D. O'Hallaron, J. Schewchuk and J. Xu (1998). Large-scale simulation of elastic wave propagation in heterogeneous media on parallel computers, *Computer methods in applied mechanics and engineering*, **152**, 85-102.
- Barka, A. (1993). Tectonics of the Erzincan Basin and Its Vicinity and 13 March 1992 Erzincan Earthquake, 2nd National Conference on Earthquake Engineering, Istanbul, Turkey, 259-270 (in Turkish).
- Beresnev, I. and G. M. Atkinson (1997). Modeling finite-fault radiation from the  $\omega^n$  spectrum, *Bull. Seism. Soc. Am.* **87**, 67 - 84.

- Beresnev, I. and G. M. Atkinson (1998a). FINSIM—a FORTRAN program for simulating stochastic acceleration time histories from finite-faults, *Seism. Res. Lett.* **69**, 27–32.
- Beresnev, I. and G. M. Atkinson (1998b). Stochastic finite-fault modeling of ground motions from the 1994 Northridge, California earthquake. I. Validation on rock sites, *Bull. Seism. Soc. Am.* **88**, 1392–1401.
- Bernard, P., J.C. Gariel and L. Dorbath (1997). Fault location and rupture kinematics of the magnitude 6.8, 1992 Erzincan earthquake, Turkey, from strong ground motion and regional records, *Bull. Seism. Soc. Am.* **87**, 1230–1243.
- Bindi, D., F. Pacor, L. Luzi, M. Massa and G. Ameri (2009). The Mw 6.3, 2009 L’Aquila earthquake: source, path and site effects from spectral analysis of strong motion data, *Geophys. J. Int.* **179**, 1573–1579.
- Birgoren, G., H. Sekiguchi, and K. Irikura (2004). Rupture model of the 1999 Duzce, Turkey, earthquake deduced from high and low frequency strong motion data. *Geophys. Res. Lett.* **31**, L05610, doi:10.1029/2003GL019194.
- Birgoren, G. and K. Irikura (2005). Estimation of site response in time domain using the Meyer-Yamada wavelet analysis, *Bull. Seism. Soc. Am.* **95**, 1447–1456.
- Bizzarri, A. and P. Spudich (2008). Effects of supershear rupture speed on the high-frequency content of *S* waves investigated using spontaneous dynamic rupture models and isochrone theory, *J. Geophys. Res.* **113**, B05304.
- Boore, D. M. and W. B. Joyner (1978). The influence of rupture incoherence on seismic directivity, *Bull. Seism. Soc. Am.* **68**, 283–300.
- Boore, D. M. (1983). Stochastic simulation of high-frequency ground motions based on seismological models of the radiated spectra, *Bull. Seism. Soc. Am.* **73**, 1865–1894.
- Boore, D. M. (1984). Use of seismoscope records to determine  $M_L$  and peak velocities, *Bull. Seism. Soc. Am.* **74**, 315–324.
- Boore, D.M. and W.B. Joyner (1997). Site amplifications for generic rock sites, *Bull. seism. Soc. Am.* **87**, 327–341.
- Boore, D. M. (2003). Simulation of ground motion using the stochastic method, *Pure and Applied Geophysics* **160**, 635–675.
- Boore, D. M. and G. M. Atkinson (2007). Boore-Atkinson NGA ground motion relations for the geometric mean horizontal component of peak and spectral ground motion parameters, PEER Report 2007/01, Berkeley, CA: Pacific Earthquake Engineering Research Center, University of California.

Borcherdt, R. D. (1970). Effects of local geology on ground motion near San Francisco Bay, *Bull. Seismol. Soc. Am.* **60**, 29–61.

Bouchon, M. (1981). A simple method to calculate Green's functions for elastic layered media, *Bull. Seismol. Soc. Am.* **71**, 959 - 971.

Bouchon, M., M. Bouin, H. Karabulut, M. N. Toksöz, M. Dietrich, and A. J. Rosakis (2001). How fast is rupture during an earthquake? New insights from the 1999 Turkey Earthquakes, *Geophys. Res. Lett.* **28**, 2723–2726.

Bouchon, M. and H. Karabulut (2008). The Aftershock Signature of Supershear Earthquakes, *Science* **320** (5881), 1323-1325.

Bouin, M.P., M. Bouchon, H. Karabulut, M. Aktar (2004). Rupture process of the 1999 November 12 Duzce (Turkey) earthquake deduced from strong motion and Global Positioning System measurements, *Geophys. J. Int.* **159**, 207–211.

Bray, J. D. and Rodriguez-Marek, A. (2004). Characterization of forward-directivity ground motions in the near-fault region, *Soil Dynamics and Earthquake Engineering* **24**, 815–828.

Brune, J. (1970). Tectonic stress and the spectra of seismic shear waves from earthquakes, *J. Geophys. Res.* **75**, 4997–5009.

Brune, J. (1971). Correction, *J. Geophys. Res.* **76**, 5002.

Burgmann, R., M.E. Ayhan, E.J. Fielding, T.J. Wright, S. McClusky, B. Aktug, C. Demir, O. Lenk and A. Turkezer (2002). Deformation during the 12 November 1999 Duzce, Turkey, Earthquake from GPS and InSAR Data, *Bull. Seism. Soc. Am.* **92**, 161–171.

Cakir, Z., A. Barka, J.B. de Chabaliere, A. Armijo, and B. Meyer (2003). Kinematics of the November 12, 1999 ( $M_w = 7.2$ ) Duzce earthquake from SAR interferometry, *Turk. J. Earth Sci.* **12**, 105–118.

Campbell, K. W. and Bozorgnia, Y. (2007). Campbell-Bozorgnia NGA ground motion relations for geometric mean horizontal component of peak and spectral ground motion parameters, Report PEER 2007/02, Berkeley CA: Pacific Earthquake Engineering Research Center, University of California.

Castro, R. R., A. Rovelli, M. Cocco, M. Di Bona, and F. Pacor (2001). Stochastic simulation of strong-motion records from the 26 September 1997 ( $M_w$  6), Umbria–Marche (central Italy) earthquake, *Bull. Seism. Soc. Am.* **91**, 27-39.

Castro, R.R., F. Pacor, G. Franceschina, D. Bindi, G. Zonno, and L. Luzi (2008). Stochastic Strong-Motion Simulation of the Mw 6 Umbria–Marche Earthquake of September 1997: Comparison of Different Approaches, *Bull. Seism. Soc. Am.* **98**, 662–670.

Chen, X. and Zhang H. (2001). An Efficient Method for Computing Green's Functions for a Layered Half-Space at Large Epicentral Distances, *Bull. Seism. Soc. Am.* **91**, 858 - 869.

Cirella, A., A. Piatanesi, M. Cocco, E. Tinti, L. Scognamiglio, A. Michelini, A. Lomax, and E. Boschi (2009). Rupture history of the 2009 L'Aquila (Italy) earthquake from non-linear joint inversion of strong motion and GPS data, *Geophys. Res. Lett.* **36**, L19304, doi:10.1029/2009GL039795.

Claprood, M., and M. W. Asten (2007). Use of SPAC, HVSR and strong motion analysis for site hazard study over the Tamar Valley in Launceston, Tasmania, in McCue, K., and Lenz, S., editors, *Earthquake Engineering in Australia Conference 2007*, Australian Earthquake Engineering Society, Wollongong.

Cohen, G., P. Joly, and N. Tordjman (1993). Construction and analysis of higher-order finite elements with mass lumping for the wave equation, in: Kleinman R. (Ed.), in *Proceedings of the Second International Conference on Mathematical and Numerical Aspects of Wave Propagation*, SIAM, Philadelphia, Pennsylvania, 152-160.

De Luca G., S. Marcucci, G. Milana and T. Sanò (2005). Evidence of Low-Frequency Amplification in the City of L'Aquila, Central Italy, through a Multidisciplinary Approach Including Strong- and Weak-Motion Data, Ambient Noise, and Numerical Modeling, *Bull. Seism. Soc. Am.* **95**, 1469 - 1481.

Delouis, B., P. Lundgren and D. Giardini (2004). Slip distributions of the 1999 Düzce (Mw 7.2) and Izmit (Mw 7.6) earthquakes on the North Anatolian Fault (Turkey): A combined analysis, *internal report*, 2004.

Dragovich, J. J. and A. Lepage (2009). FDE index for goodness-of-fit between measured and calculated response signals, *Earthquake Engng Struct. Dyn.* **38**, 1751–1758.

Dunham, E.M. and R.J. Archuleta (2004). Evidence for a supershear transient during the 2002 Denali fault earthquake, *Bull. Seism. Soc. Am.* **94**, S256–S268.

Durukal, E. (2002). Critical evaluation of strong motion in Kocaeli and Duzce (Turkey) earthquakes, *Soil Dyn. and Earthq. Eng.* **22**, 589–609.

Erdik, M. and E. Durukal (2001). A Hybrid Procedure for the Assessment of Design Basis Earthquake Ground Motions for Near-fault Conditions, *Soil Dyn. Earthq. Eng.* **21**, 431–443.

EXSIM. A FORTRAN program for simulating stochastic acceleration time histories from finite-faults with a dynamic corner frequency approach.

- Frankel, A. and J. Vidale (1992). A three-dimensional simulation of seismic waves in the Santa Clara Valley, California, from a Loma Prieta aftershock, *Bull. Seism. Soc. Am.* **82**, 2045-2074.
- Frankel, A. (1993). Three-dimensional simulations of the ground motions in the San Bernardino valley, California, for hypothetical earthquakes on the San Andreas fault, *Bull. Seism. Soc. Am.* **83**, 1020-1041.
- Galuzzo, D., G. Zonno and E. Del Pezzo (2008). Stochastic Finite-Fault Ground-Motion Simulation in a Wave-Field Diffusive Regime: Case Study of the Mt. Vesuvius Volcanic Area, *Bull. Seism. Soc. of Am.* **98-3**; 1272-1288.
- Grosser, H., M. Baumbach, H. Berchemer, B. Baier, A. Karahan, H. Schelle, F. Kruger, A. Paulat, G. Michel, R. Demirtas, S. Gencoglu, and R. Yılmaz (1998). The Erzincan earthquake ( $M_s=6.8$ ) of March 13, 1992 and its aftershock sequence, *Pure Appl. Geophys.* **152**, 465–505.
- Gülkan, P. and E. Kalkan (2002). Attenuation modeling of recent earthquakes in Turkey, *Journal of Seismology* **6**, 397-409.
- Gürbüz, C., A. Pınar, Ş. Barış and A. M. Işıkara (1993). 13 March 1992 Erzincan Earthquake and Aftershocks, 2nd National Conference on Earthquake Engineering, Istanbul, Turkey, 300-309 (in Turkish).
- Gurpinar, A., M. Abalı, M. S. Yucemen and Y. Yesilcay (1978). Feasibility of Mandatory Earthquake Insurance in Turkey, Earthquake Engineering Research Center, Report No. 78-05, Middle East Technical University, Ankara. (in Turkish).
- Hanks, T. C. (1979).  $b$  Values and  $\omega^{-\gamma}$  Seismic Source Models: Implications for Tectonic Stress Variations Along Active Crustal Fault Zones and the Estimation of High-Frequency Strong Ground Motion, *J. Geophys. Res.* **84(B5)**, 2235–2242, doi:10.1029/JB084iB05p02235.
- Hanks, T., and H. Kanamori (1979). A moment magnitude scale, *J. Geophys. Res.* **84**, 2348-2350.
- Hanks, T. C. and R. K. McGuire (1981). The character of high frequency strong ground motion, *Bull. Seism. Soc. Am.* **71**, 2071-2095.
- Hanks, T. C. (1982).  $f_{\max}$ , *Bull. Seism. Soc. Am.* **72**, 1867-1879.
- Hanks, T. C. and Boore, D. M. (1984). Moment-Magnitude Relations in Theory and Practice, *J. Geophys. Res.* **89**, 6229–6235.
- Hartzell, S. (1978). Earthquake aftershocks as Green's functions, *Geophys. Res. Lett.* **5**, 1–14.

- Hartzell, S., S. Harmsen, A. Frankel and S. Larsen (1999). Calculation of broadband time histories of ground motion: Comparison of methods and validation using strong-ground motion from the 1994 Northridge earthquake, *Bull. Seism. Soc. Am.* **89**, 1484 - 1504.
- Haskell, N.A. (1960). Crustal reflections of plane SH waves, *J. Geophys. Res.* **65**, 4147-4150.
- Haskell, N. A. (1964). Total energy and energy spectral density of elastic wave radiation from propagating faults, *Bull. Seism. Soc. Am.* **54**, 1811-1841.
- Haskell, N. A. (1966). Total energy and energy spectral density of elastic wave radiation from propagating faults. Part II. A Statistical Source Model, *Bull. Seism. Soc. Am.* **56**, 125-140.
- Heaton, T.H. (1990). Evidence for and implications of self-healing pulses of slip in earthquake rupture, *Phys. Earth Planet Int.* **64**, 1-20.
- Herrmann, R.B. (1985). An extension of Random Vibration Theory estimates of strong ground motion to large earthquakes, *Bull. Seis. Soc. Am.* **75**, 1447–1453.
- Hisada, Y. (1994). An efficient method for computing Green's functions for a layered half-space with sources and receivers at close depths, *Bull. Seis. Soc. Am.* **84**, 1456 - 1472.
- Hisada, Y. and J. Bielak (2003). A Theoretical Method for Computing Near-Fault Ground Motions in Layered Half-Spaces Considering Static Offset Due to Surface Faulting, with a Physical Interpretation of Fling Step and Rupture Directivity, *Bull. Seis. Soc. Am.* **93**, 1154 - 1168.
- Hisada, Y. (2008). Broadband strong motion simulation in layered half-space using stochastic Green's function technique, *Journal of Seismology*, **12**, 265-279.
- Housner, G. W. (1947). Characteristics of strong-motion earthquakes, *Bull. Seis. Soc. Am.* **37**, 19 - 31.
- Housner, G. W. (1955). Properties of strong ground motion earthquakes, *Bull. Seis. Soc. Am.* **45**, 197 – 218.
- Huang, H. and Teng T. (1999). An evaluation on H/V Ratio vs. Spectral Ratio for Site-response Estimation Using the 1994 Northridge Earthquake Sequences, *Pure Appl. Geophys.* **156**, 631-649.
- Irikura, K. (1986). Prediction of strong acceleration motions using empirical Green's function, in *Proc. 7th Japan Earthq. Eng. Symp.* 151–156, Tokyo, Japan.
- ITACA, Italian Accelerometric Archive, <http://itaca.mi.ingv.it/ItacaNet>, last visited on 14 September 2010.

- Joyner, W., and T. Fumal (1985). Predictive mapping of ground motion in *Evaluating Earthquake Hazards in the Los Angeles Region*, Ziony (Editor), *U.S. Geol. Surv. Prof. Pap. 1360*, 203–220.
- Kamae, K., K. Irikura, and A. Pitarka (1998). A technique for simulating strong ground motion using Hybrid Green's function, *Bull. Seism. Soc. Am.* **88**, 357–367.
- Kawase, H. (1988). Time-Domain response of a semi-circular canyon for incident SV, P, and Rayleigh waves calculated by the discrete wavenumber boundary element method, *Bull. Seism. Soc. Am.* **78**, 1415-1437.
- Kennett, B.L.N. (1983). *Seismic wave propagation in a stratified half-space*, Cambridge University Press, Cambridge.
- KOERI, UDIM, <http://www.koeri.boun.edu.tr/sismo/default.htm>, last visited on 14 September 2010.
- Komatitsch, D. (1997). Spectral and spectral element methods for the 2D and 3D elastodynamics equations in heterogeneous media, Ph. D. Thesis, Institut de Physique du Globe, Paris, France.
- Komatitsch, D. and J.-P. Vilotte (1998). The spectral element method: an efficient tool to simulate the seismic response of 2D and 3D geological structures. *Bull. Seismol. Soc. Am.* **88**, 368-392.
- Komatitsch, D. and J. Tromp (1999). Introduction to the spectral element method for 3-D seismic wave propagation, *Geophys. J. Int.* **139**, 806-822.
- Komatitsch, D., Q. Liu, J. Tromp, P. Süß, C. Stidham, and J. Shaw (2004). Simulations of ground motion in the Los Angeles basin based upon the spectral-element method, *Bull. Seismol. Soc. Am.* **94**, 187-206.
- Konca, A.O., S. Leprince, J.-P. Avouac and D.V. Helmberger (2010). Rupture Process of the 1999 Mw 7.1 Duzce Earthquake from Joint Analysis of SPOT, GPS, InSAR, Strong-Motion, and Teleseismic Data: A Supershear Rupture with Variable Rupture Velocity, *Bull. Seism. Soc. Am.* **100**, 267–288.
- Kramer, S.L. (1996). *Geotechnical Earthquake Engineering*, Prentice Hall, Inc., Upper Saddle River, New Jersey, 653 pp.
- Kudo, K., T.Kanno, H.Okada, O.Özel, M. Erdik, M. Takahashi, T. Sasatani, S. Higashi and K. Yoshida (2002). Site Specific Issues on Strong Ground Motion during the Kocaeli, Turkey Earthquake of August 17, 1999, as Inferred from Array Observations of Microtremors and Aftershocks, *Bull. Seism. Soc. Am.* **92**, 448-465.
- Lav, A., A. Erken, R. İyisan and A. Ansal (1993). The Local Soil Conditions in Erzincan and Its Effects on Structural Damage, Proc. of XII. Technical Conference of Turkish Civil Engineering, Ankara, Turkey, 25-38 (in Turkish).

Lay, T. and T. C. Wallace (1995). Modern global seismology, Volume 58 of *International geophysics series*. San Diego: Academic Press.

Legrand, D. and B. Delouis (1999). Determination of the fault plane using a single near-field seismic station with a finite-dimension source model, *Geophys. J. Int.* **138**, 801–808.

Lermo, J. and F. J. Chávez-García (1994). Are microtremors useful in site response evaluation? *Bull. Seismol. Soc. Am.* **84**, 1350-1364.

Li, X., J. Bielak, and O. Ghattas (1992). Three-dimensional earthquake site response on a CM-2, in *Proc. 10th World Conf. on Earthquake Eng.*

Louie, J.N. (2001). Faster, Better: Shear-wave velocity to 100 meters depth from refraction microtremor arrays, *Bull. Seism. Soc. Am.* **91**, 347-364.

Luco, E. J., H. I. Wong and F. C. P. de Barros (1990). Three-dimensional response of a cylindrical crayon in a layered half-space, *Earthquake Eng. Struc. Dynamics*, **19**, 799-817.

Malagnini, L., R. B. Herrmann and M. Di Bona (2000). Ground-Motion Scaling in the Apennines (Italy), *Bull. Seism. Soc. Am.* **90**, 1062 - 1081.

Malagnini, L., L. Scognamiglio, A. Mercuri, A. Akinci and K. Mayeda (2008). Strong evidence for non-similar earthquake source scaling in central Italy, *Geophys. Res. Lett.* **35**:L17303.

Malagnini, L. (2010). Personnel Communication.

Margaris, B. N., and D. M. Boore (1998). Determination of  $\Delta\sigma$  and  $\kappa_0$  from response spectra of large earthquakes in Greece, *Bull. Seism. Soc. Am.* **88**, 170–182.

Mavroeidis, G. P. and Papageorgiou A. S. (2003). A mathematical representation of near-fault ground motions, *Bull. Seism. Soc. Am.* **93**, 1099–1131.

McGuire, R. K. and T. C. Hanks (1980). RMS accelerations and spectral amplitudes of strong ground motion during the San Fernando, California, earthquake, *Bull. Seism. Soc. Am.* **70**, 1907–1919.

Milkereit, C., S. Zunbul, S. Karakisa, Y. Iravul, J. Zschau, M. Baumbach, H. Grosser, E. Gunther, N. Umutlu, T. Kuru, E. Erkul, K. Klinge, M. Ibs von Seht, and A. Karahan (2000). Preliminary aftershock analysis of the Mw=7.4 Izmit and Mw=7.1 Düzce earthquake in western Turkey, in: Barka, A., Kozaci, O., Akyuz, S. (Eds.), *The 1999 Izmit and Düzce Earthquakes: Preliminary Results*. Istanbul Technical University, ISBN: 975-561-182-7, 179–187.

- Moczo, P., J. Kristek, V. Vavrycuk, R. J. Archuleta, and L. Halada (2002). 3D Heterogeneous Staggered-Grid Finite-Difference Modeling of Seismic Motion with Volume Harmonic and Arithmetic Averaging of Elastic Moduli and Densities, *Bull. Seism. Soc. Am.* **92**, 3042 - 3066.
- Mohammadioun, B. and L. Serva (2001). Stress drop, slip type, earthquake magnitude, and seismic hazard, *Bull. Seismol. Soc. Am.* **91**, 694–707.
- Motazedian, D., and G. M. Atkinson (2005). Stochastic finite-fault modeling based on a Dynamic Corner Frequency, *Bull. Seism. Soc. Am.* **95**, 995–1010.
- Motazedian, D. (2006). Region-Specific Key Seismic Parameters for Earthquakes in Northern Iran, *Bull. Seism. Soc. Am.* **96**, 1383–1395.
- Motazedian, D. and A. Moinfar (2006). Hybrid stochastic finite fault modeling of 2003, M6.5, Bam earthquake (Iran), *Journal of Seismology* **10**, 91-103.
- Nakamura, Y. (1989). A method for dynamic characteristics estimation of subsurface using microtremor on the ground surface, *QR RTRI* **30**, 25–33.
- Olsen, K. B., R. J. Archuleta, and J. R. Matarese (1996). Three-dimensional simulation of a magnitude 7.75 earthquake on the San Andreas fault, *Science* **270**, 1628-1632.
- Olsen, K. B. and R. J. Archuleta (1996). Three-dimensional simulation of earthquakes on the Los Angeles fault system, *Bull. Seism. Soc. Am.* **86**, 575-596.
- Özmen, B. and G. Bağcı (2000). 12 November 1999 Düzce Earthquake Report, Ministry of Public Works and Settlement, General Directorate of Disaster Affairs, Ankara (in Turkish).
- Öztaş, T. (1993). General Engineering Geological Properties of Erzincan City Vicinity, 2nd National Conference on Earthquake Engineering, Istanbul, Turkey, 281-291 (in Turkish).
- Papadopoulos, G. A., M. Charalampakis, A. Fokaefs, and G. Minadakis (2010). Strong foreshock signal preceding the L'Aquila (Italy) earthquake ( $M_w$  6.3) of 6 April 2009, *Nat. Hazards Earth Syst. Sci.* **10**, 19–24.
- Papageorgiou, A. S. and K. Aki (1983). A specific barrier model for the quantitative description of inhomogeneous faulting and prediction of strong ground motion, Part I and II, *Bull. Seis. Soc. Am.* **73**, 693-722 and 953-978.
- Park, C.B., R. D. Miller and J. Xia (1999). Multi-channel analysis of surface waves, *Geophysics* **64**, 800-808.
- Pedersen, H. A., F. J. Sánchez-Sesma and M. Campillo (1994). Three-dimensional scattering by two-dimensional topographies, *Bull. Seism. Soc. Am.* **84**, 1169-1183.

- Pinar, A., Y. Honkura and M. Kikuchi (1994). Rupture process of the 1992 Erzincan Earthquake and its implication for seismotectonics in eastern Turkey, *Geophys. Res. Lett.* **21**(18), 1971–1974, doi:10.1029/94GL01712.
- Pitarka, A., K. Irikura, T. Iwata, and H. Sekiguchi (1998). Three-dimensional simulation of the near-fault ground motion for the 1995 Hyogo-Ken Nanbu (Kobe), Japan, earthquake, *Bull. Seism. Soc. Am.* **88**, 428-440.
- Pitarka, A., P. Somerville, Y. Fukushima, T. Uetake and K. Irikura (2000). Simulation of Near-Fault Strong-Ground Motion Using Hybrid Green's Functions, *Bull. Seism. Soc. Am.* **90**, 566 - 586.
- Priolo, E., J. M. Carcione and G. Seriani (1994). Numerical simulation of interface waves by high-order spectral modeling techniques, *J. Acoust. Soc. Am.* **95**, 681-693.
- Raghukanth, S. T. G. and S. N. Somala (2009). Modeling of Strong-Motion Data in Northeastern India: Q, Stress Drop, and Site Amplification *Bull. Seism. Soc. Am.* **99**, 705-725.
- Rathje, E.M., J. P. Stewart, M.B. Baturay, J.D. Bray, and J.P. Bardet (2006). Strong ground motions and damage patterns from the 1999 Düzce earthquake in Turkey, *Journal of Earthquake Engineering*, **10** (5), 693–724.
- Rial, J. A., N. G. Saltzman, and H. Ling (1992). Earthquake induced resonance in sedimentary basins, *American Scientists* **80**, 566-578.
- Rosenblad, B.L. and J. Li (2009). Comparative Study of Refraction Microtremor (ReMi) and Active Source Methods for Developing Low-Frequency Surface Wave Dispersion Curves, *Journal of Environmental and Engineering Geophysics*, in press.
- Roumelioti, Z., A. Kiratzi, and N. Theodulidis (2004). Stochastic Strong Ground-Motion Simulation of the 7 September 1999 Athens (Greece) Earthquake, *Bull. Seism. Soc. Am.* **94**, 1036 - 1052.
- Rovelli, A., O. Bonamassa, M. Cocco, M. Di Bona, and S. Mazza (1988). Scaling laws and spectral parameters of the ground motion in active extensional areas in Italy, *Bull. Seism. Soc. Am.* **78**, 530–560.
- Sanchez-Sesma, F.J. (1987). Site effects on strong ground motion, *Soil. Dyn. Earthq. Eng.* **6**, 124-132.
- Schmidt, R.O. (1986). Multiple emitter location and signal parameter estimation. *IEEE Transactions on Antennas and Propagation*, AP-34, 276-280.
- Shoja-Taheri, J., and H. Ghofrani (2007). Stochastic Finite-Fault Modeling of Strong Ground Motions from the 26 December 2003 Bam, Iran, Earthquake, *Bull. Seism. Soc. Am.* **97**, 1950 - 1959.

Somerville, P.G., N.F. Smith, R.W. Graves and N.A. Abrahamson (1997). Modification of empirical strong ground motion attenuation relations to include the amplitude and duration effects of rupture directivity, *Seismol. Res. Lett.* **68**, 199–222.

Stein, S., A. A. Barka and J. H. Dietrich (1997). Progressive failure on the North Anatolian fault since 1939 by earthquake stress triggering, *Geophys. J. Int.* **128**, 594-604.

Stein, S. and M. Wysession (2003). An Introduction to Seismology, Earthquakes, and Earth Structure, Blackwell Science, Oxford, 498 pp.

Stokoe, K.H., II Wright, S.G., Bay, J.A. and Roesset, J.M. (1994). Characterization of Geotechnical Sites by SASW Method, ISSMFE Technical Committee #10 for XIII ICSMFE, Geophysical Characterization of Sites, A. A. Balkema Publishers/Rotterdam & Brookfield, Netherlands, 15-25.

Strong Ground Motion Database of Turkey, DAPHNE, [http://daphne.deprem.gov.tr:89/2K/daphne\\_v4.php](http://daphne.deprem.gov.tr:89/2K/daphne_v4.php), last visited on 14 September 2010.

Suzuki, T., Y. Adachi, and M. Tanaka (1995). Application of microtremor measurements to the estimation of earthquake ground motions in Kushiro City during the Kushiro-Oki earthquake of 15 January 1993, *Earthq. Eng. Struct. Dyn.* **24**, 595-613.

Şaroğlu, F., Ö. Emre ve İ. Kuşçu (1992). Active Fault Map of Turkey, *Mineral Res. Explor. Inst. Turkey*.

Thomson, W. T. (1959). Spectral Aspect Of Earthquakes, *Bull. Seism. Soc. Am.* **49**, 91-98.

Tinti, E. (2010). Personnel Communication.

Toro, G. R. and R. K. McGuire (1987). An Investigation into Earthquake Ground Motion Characteristics in Eastern North America, *Bull. Seismol. Soc. Am.* **77**, 468–489.

Toshinawa, T. and T. Ohmachi (1992). Love-wave propagation in a three-dimensional basin, *Bull. Seism. Soc. Am.* **82**, 1661-1677.

Ulusay, R., E. Tuncay, H. Sonmez and C. Gokceoglu (2004). An attenuation based on Turkish strong motion data and iso-acceleration map of Turkey, *Engineering Geology* **74**, 265-291.

Ugurhan, B. and A. Askan (2010). Stochastic Strong Ground Motion Simulation of the 12 November 1999 Düzce (Turkey) Earthquake Using a Dynamic Corner Frequency Approach, *Bull. Seism. Soc. Am.* **100**, 1498-1512.

Ugurhan, B., A. Askan and M. A. Erberik (2010). A Methodology for Seismic Loss Estimation in Urban Regions based on Ground Motion Simulations, submitted to *Bull. Seism. Soc. Am.*

Umutlu, N., K. Koketsu, and C. Milkereit (2004). The rupture process during the 1999 Duzce, Turkey, earthquake from joint inversion of teleseismic and strong-motion data, *Tectonophysics* **391**, 315–324.

Utkucu, M., S.S. Nalbant, J. McCloskey, S. Steacy, and O. Alptekin (2003). Slip distribution and stress changes associated with the 1999 November 12, Duzce (Turkey) earthquake ( $M_w = 7.1$ ), *Geophys. J. Int.* **153**, 229–241.

USGS, Earthquake Facts and Statistics, <http://earthquake.usgs.gov/earthquakes/eqarchives/year/eqstats.php>, last visited on 14 September 2010.

USGS, Earthquake Hazards Program: Earthquake Report, Eastern Turkey, [http://neic.usgs.gov/neis/eq\\_depot/2003/eq\\_030501/](http://neic.usgs.gov/neis/eq_depot/2003/eq_030501/), last visited on 14 September 2010.

Vanmarcke, E. H. and S. P. Lai (1980). Strong-motion duration and RMS amplitude of earthquake records, *Bull. Seism. Soc. Am.* **70**, 1293 - 1307.

Watson-Lamprey, J. A. and D. M. Boore (2007). Beyond SaGMRotI: Conversion to Sa<sub>Arb</sub>, Sa<sub>SN</sub>, and Sa<sub>MaxRot</sub>, *Bull. Seism. Soc. Am.* **97**, 1511-1524.

Wells, D., and K. Coppersmith (1994). New empirical relationships among magnitude, rupture length, rupture width, rupture area, and surface displacement, *Bull. Seism. Soc. Am.* **84**, 974 -1002.

Yagi, Y. and M. Kikuchi (1999). Preliminary Results of Rupture Process for the November 12, 1999 Turkey Earthquake, Earthquake Research Institute, The University of Tokyo, Online report, <http://www.eri.u-tokyo.ac.jp/yuji/trk2/Turkeyafter.html>, last visited on 14 September 2010.

Yalçınkaya, E. (2004). Investigation of Parameters Affecting the Soil Amplification for 1-D Models, *Yerbilimleri Dergisi*, **17**, 47-56 (in Turkish).

Yalcinkaya, E. (2005). Stochastic Finite-fault Modeling of Ground Motions From the June 27, 1998 Adana-Ceyhan Earthquake, *Earth Planets Space* **57**,107–115.

Yomogida, K. and J. T. Egeten (1993). 3-D wave propagation in the Los Angeles basin for the Whittier-narrows earthquake, *Bull. Seism. Soc. Am.* **83** 1325-1344.

Yucemen, M. S. and A. Askan (2003). Estimation of earthquake damage probabilities for reinforced concrete buildings, In: S. T. Wasti and G. Ozcebe (eds), Seismic Assessment and Rehabilitation of Existing Buildings, NATO Science Series IV: Earth and Environmental Sciences, Kluwer Academic Publishers, **29**, 149–164.

## APPENDIX A

### STRESS DROP

Stress drop is the difference in the state of stress before and after the rupture takes place. The following discussion explains how the rupture process occurs.

Earthquakes are sudden releases of strain accumulation which develops near the fault plane over a long time. For any point on the fault plane, there is a stress concentration  $\tau_0$  due to this accumulation before the earthquake rupture occurs. When the rupture approaches to the point of interest, the stress concentration increases until it reaches the strength of the fault,  $\tau_s$ . When the stress exceeds the strength of the fault, slip starts to develop. With the development of the slip, stress diminishes and reaches  $\tau_f$ . After the termination of slip, the state of stress reaches its final value,  $\tau_1$ .  $\tau_1$  can be greater or smaller than  $\tau_f$  depending whether velocity hardening or weakening occurs. Figure A.1 displays the variation in stress with respect to time (Lay and Wallace, 1995).

The stress drop is simply defined as:

$$\Delta\sigma = \tau_0 - \tau_1 \quad (\text{A.1})$$

Stress drop can show variations over the fault plane. In stochastic strong ground motion simulations, the static stress drop is used and it is defined as the integration of stress drop values over the fault plane, divided by the fault area.

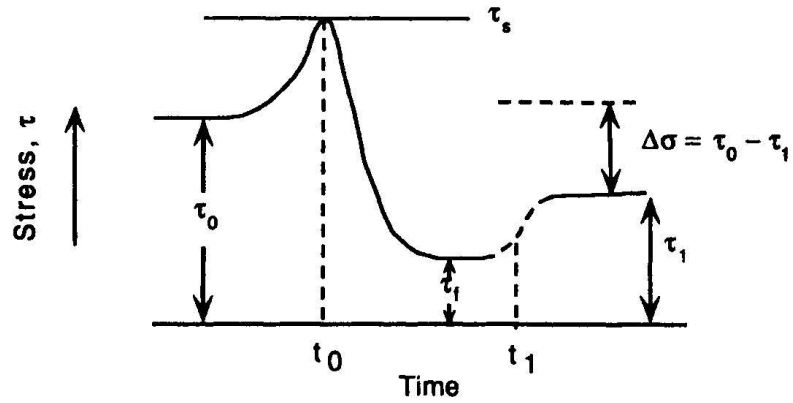


**Figure A.1** Stress variation with respect to time at a point on the fault plane  
(Adapted from Lay and Wallace, 1995)

For a fault plane having a characteristic dimension of  $\bar{L}$  (either length or width), the strain change due to a slip value of  $D$  can be represented as  $D/\bar{L}$ . Using Hooke's law, the stress drop associated with the aforementioned strain is defined as:

$$\Delta\sigma = C\mu\left(\frac{D}{\bar{L}}\right) \quad (\text{A.2})$$

Where  $C$  is a constant describing fault geometry.

Since  $M_0 = \mu AD$ , stress drop can be represented using the seismic moment as:

$$\Delta\sigma = \frac{CM_0}{\bar{L}^3} = \frac{CM_0}{S^{3/2}} \quad (\text{A.3})$$

where  $S$  represents the fault area.

For a circular fault plane having radius  $R$ , the static stress drop is defined as:

$$\Delta\sigma = \frac{7M_0}{16R^3} \quad (\text{A.4})$$

An important observation is that stress drop is proportional to the cube of the characteristic fault length. Thus, it is crucial to accurately determine the fault dimensions. Ambiguity in fault dimensions leads to larger ambiguities in stress drop values.

## APPENDIX B

### MAGNITUDE SCALES

Magnitudes are used to reflect earthquake size. After the corrections for geometrical spreading and anelastic attenuation are made, the wave amplitudes reflect the magnitude of an earthquake. Magnitude scales are mostly empirical and they depend on the largest amplitude recorded on seismographs.

The magnitude scales have the following general format:

$$M = \log\left(\frac{A}{T}\right) + f(\Delta, h) + C \quad (\text{B.1})$$

where  $A$  represents the amplitude of a signal having a dominant period of  $T$  and  $C$  is a constant to reflect the regional effects. A correction  $f$  is applied for the source-to-receiver distance  $\Delta$  and focal depth,  $h$ .

A common magnitude scale used is the local magnitude,  $M_L$  which is computed with the following equation:

$$M_L = \log_{10} A + 2.76 \log_{10} \Delta - 1.67 \quad (\text{B.2})$$

where  $A$  is the largest displacement amplitude measured on a Wood-Anderson seismograph in  $10^{-6}$  m and  $\Delta$  is in km. The fact that the dominant period of Wood-Anderson seismograph (0.8 s) and many buildings (around 1 s) are very close to each other make  $M_L$  to be a good indicator of structural damage.

Body wave magnitude,  $m_b$  is another scale that is frequently used. P-wave portion is usually used in determining  $m_b$  with the following relation:

$$m_b = \log\left(\frac{A}{T}\right) + Q(h, \Delta) \quad (\text{B.3})$$

where  $Q$  is an empirical function depending on focal depth and distance.

The most important disadvantage of  $M_L$  and  $m_b$  scales is that they are observed to saturate for large magnitude events.

Surface wave magnitude,  $M_s$  utilizes the surface wave portion of the records. It is defined as:

$$M_s = \log\left(\frac{A}{T}\right) + 1.66 \log \Delta + 3.3 \quad (\text{B.4})$$

In Equation (B.4),  $A$  is in microns,  $T$  is in seconds and  $\Delta$  is in degrees.  $M_s$  scale is used only for shallow events since it is not applicable to deep ones.

The most common and physical magnitude scale is moment magnitude,  $M_w$ . It is defined as:

$$M_w = \frac{2}{3} M_0 - 10.73 \quad (\text{B.5})$$

where  $M_0$  is the seismic moment in dyn-cm.

Another magnitude scale that is frequently used is earthquake duration magnitude. The distinction of this magnitude scale from the aforementioned scales is that it does not depend on the largest amplitude obtained in the seismograms. It directly depends on the duration of the seismogram which is obtained starting from the arrival of the seismic waves up to the point where predefined percentage of the seismic energy is

achieved. Thus, the basis of the earthquake duration magnitude is that the longer the duration of the seismogram, the larger the magnitude of the earthquake.

## APPENDIX C

### MISFIT VALUES OF DÜZCE AND L'AQUILA SIMULATIONS

#### a) 1999 Düzce Earthquake Simulation

Station Code	Error <sub>f</sub>
BOL	0.488
DZC	0.961
GLC	0.660
GYN	0.407
IZN	0.394
IZT	0.409
MDR	0.669
SKR	0.624
YPT	1.169

#### b) 2009 L'Aquila Earthquake Simulation

Station Code	Error <sub>f</sub>
ANT	7.65E-42
AQA	3.87E-10
AQG	5.67E-38
AQK	6.95E-08
AQV	1.08E-05
ASS	5.22E-31
AVZ	1.20E+00
CDS	2.07E-28
CHT	3.24E-03
CLN	5.57E-24
FMG	2.41E-21
GSA	3.94E-01
GSG	5.84E-01
LSS	8.12E-17
MMP	2.46E-14
MTR	1.21E-12
ORC	4.35E-10
SBC	1.65E-07
SPC	3.13E-03
SPO	1.63E-05
SUL	2.57E-03

## APPENDIX D

### DIRECTIVITY

The azimuthal dependence of source-time function is called *directivity*. Figure D.1 shows the source-time functions obtained for different observation stations.

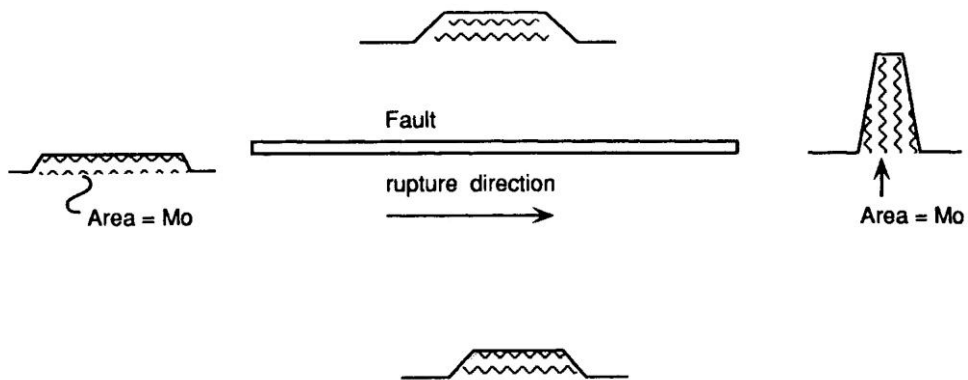


**Figure D.1** Variation in source-time function with respect to different azimuths  
(Adapted from Lay and Wallace, 1995)

The duration of rupture changes with respect to the orientation of the observer by the following equation:

$$\tau_c = \frac{L}{v_r} - \frac{L \cos \theta}{c} \quad (\text{D.1})$$

where  $L$  is the length of the fault plane,  $v_r$  is the rupture velocity,  $c$  is the wave velocity and  $\theta$  defined the angle between the fault plane and the observation point. If the station is oriented along the rupture propagation direction ( $\theta=0^\circ$ ), the records have short duration pulses. In order to conserve the area under the source-time function, magnitudes of the records have to increase. This effect, evidenced by short duration, high amplitude pulses, is called *forward directivity*. If the station is oriented in the opposite direction of the rupture propagation, the records have long duration, thus low amplitude pulses. This effect is termed as *backward directivity*.